Nonlinear Optical Spectroscopy of Single Walled Carbon Nanotubes

by

Vasudev Lal

A dissertation submitted in partial fulfillment
of the requirements for the degree of
Doctor of Philosophy
(Electrical Engineering)
in The University of Michigan
2012

Doctoral Committee:

Professor Duncan G Steel, Chair
Professor Theodore B Norris
Professor Roseanne J Sension
Assistant Professor Zhaohui Zhong

To,

Neeta and Deepak Lal for being loving parents

Nandita Lal for being a caring sister

Sulochana Dhar for being my pillar of strength.

ACKNOWLEDGEMENTS

I am really grateful to my advisor, Prof Duncan Steel for giving me the opportunity to work in his lab. His sufficiently hands-off approach helped me develop my own independent thinking and problem solving abilities, while his guidance at critical junctures was extremely useful and productive towards my research objectives. I would like to imbibe more of his work ethic, and his persistence on focusing on the fundamentals throughout my career. My project was a collaborative effort including the groups of Prof Roseanne Sension and Dr Richard Freeling, SRI International. I am very grateful for key inputs that I have received from them. Especially, the data analysis section of this thesis would not have been completed if I did not have access to an excellent program that has been developed in Prof Sension's group.

I am very grateful to the faculty who have taught me courses over my time in graduate school. I learnt a great deal from taking Professor Ted Norris's class on Classical and Ultrafast Optics, which sparked an excitement in me to pursue research involving optical techniques. At the onset of my project, I had very useful discussions with Professor Zhong and his group members that helped me get started on my project. I would like to thank Dr Joseph Schauerte for helping me get started with the laser system that I would go on to use for all my experiments. Both he and Kathleen Wisser helped me a great deal in the process that was required to prepare samples of surfactant encapsulated SWCNTs. I am also grateful to all the staff members in EECS and Physics who have helped me tremendously over the past five years.

My former and current group members have contributed immensely to having a very productive and cooperative work environment in the lab. I would like to thank Dr Leon Webster, Dr Bo Sun, Dr Katherine Truex, Dr Erik Kim, Dr Xiaodong Xu, Dr Aaron Rury for helping me get started and dealing with all my pesky little questions. Leon and John Schaibley have especially provided a lot of ideas and feedback on my project. A lot of my data might not have been possible without using a noise-eater put together by John. I also want to thank Leon for taking time out to proof-read this thesis. The future of the lab looks very bright with Colin, Alex, Cameron, and Victoria leading the way.

I have to thank my wife Sulochana Dhar for being really affectionate and patient throughout the last few years. My sister Nandita Lal, and my parents have provided me with a lot of support that helped me throughout my work. I am very grateful for all my other family and friends, both here in the US and back home in India who have always encouraged me, and held out hope even through the toughest of times.

TABLE OF CONTENTS

LIST OF FIGURES

Figure

ABSTRACT

Nonlinear Optical Spectroscopy of Single Walled Carbon Nanotubes

by

Vasudev Lal

Chair: Duncan G Steel

Single Walled Carbon Nanotubes (SWCNTs) have attracted immense attention for making molecular-scale transistors to replace silicon transistors in the post-CMOS era. Moreover, their direct bandgap nature, along with the quantized energy level structure due to reduced dimensionality makes them useful elements in chip-based photonic devices for sensing and communications. Despite the incredible amount of progress in the last few years, many aspects of the physical processes that are involved in the light-matter interaction for this system are not completely understood. This thesis reports results from optical experiments devoted to measuring small changes in the resonant energies of SWCNTs. These changes are attributed to nanomechanical effects resulting from an interaction between the optically excited excitonic states with the underlying lattice of the SWCNTs. Theoretical calculations in the literature have predicted that strong exciton-phonon coupling in SWCNTs causes a differential change in the SWCNT diameter due to optically excited population. It is inferred that such a structural change in the SWCNT leads to excitation induced shifts in the resonant energy for successive excitations on the SWCNT. These spectral shifts are detected by measuring the time-resolved nonlinear optical response of the SWCNTs.

Experiments are conducted with two synchronized lasers whose colors can be independently tuned. The obtained probe energy depedent delay scans can be globally fitted to three timescales of 8.5, 19.4 and 60.1 ps, which also allows the extraction of the decay associated spectra (DAS). A model is proposed that incorporates excitation induced spectral shifts in the interaction of resonant light with SWCNTs and predicts the derivative-like spectral lineshapes observed in the DAS. The implication of this result for SWCNT based photonic devices is explored, and further experiments to test the hypothesis in this thesis are discussed.

CHAPTER I

Novel Nano-Photonic Opportunities of Carbon Nanostructures

The surprising discovery of new allotropes of carbon(fullerenes in 1985[27], nanotubes in 1991[22], and graphene in 2004[38]) during the past thirty years has sparked intense global research initiatives. These discoveries have had major implications for fundamental science, and have led to the Nobel prize in Chemistry in 1996 for the discovery of fullerenes, and the Nobel prize in Physics in 2011 for the discovery of graphene. The interest, however, has not been limited to the pure sciences: carbon nanostructures are being actively pursued as a material system that would form the backbone of future nanoscale devices for electronics, photonics and sensing. In this chapter, some of the exciting applications, especially of Single Walled Carbon Nanotubes (SWCNTs) will be surveyed. With important applications of carbon based nanostructures set to emerge in the near future, it is vital to gain a deeper understanding of the physical processes involved that can serve as a guide for emerging applications. This is one of the key motivations behind the optical spectroscopy studies conducted for this dissertation, which aim to understand some of the fundamental effects that are at play in the interaction of resonant light with SWCNTs.

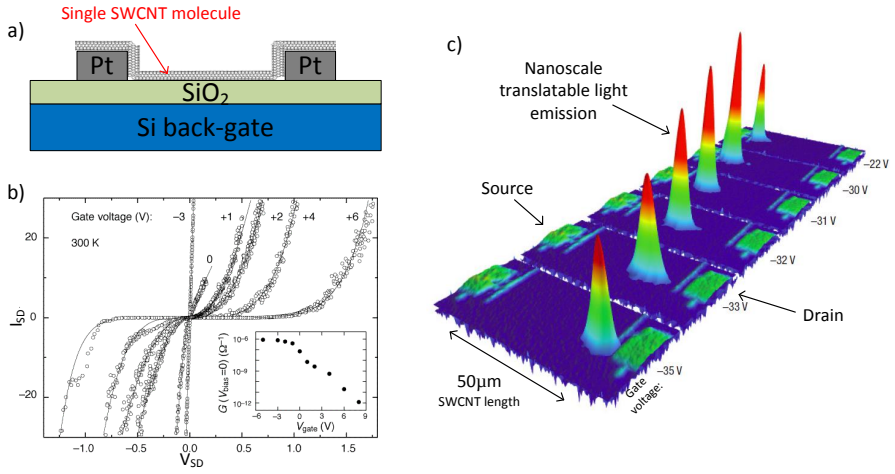

Figure 1.1: Electronic and photonics applications of SWCNT.a)Field effect transistor schematic. b)Performance characteristics of the first SWCNT based transistor[48]. c) Electroluminescence obtained from air-suspended SWCNTs[2].

1.1 SWCNT Field Effect Transistor (FET)

Figure(1.1a) shows the schematic for the very first SWCNT based transistor that was developed in 1998 [48]. Figure(1.1b) shows classic transistor behavior from the device, in which the conductance of the channel (in this case the nanotube between the metal electrodes) changes by six orders of magnitude, when the gate voltage changes by 15V. However, there still remain considerable challenges to be overcome before SWCNTs could replace silicon transistors: engineers do not have sufficient control in the self-assembly process of the growth of nanotubes, to get identical structures at predefined sites with absolute accuracies. Despite the hurdles, SWCNT based transistors are one of the leading candidates for transistor technology, once scaling of Si transistors reaches physical barriers, which is expected to happen around 2025.

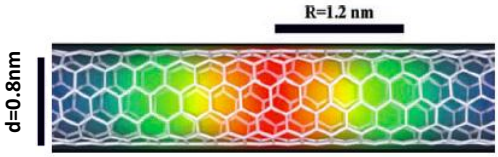

Figure 1.2: Calculated density of the exciton envelope function. Figure adapted from [52] .

1.2 Chip-scale Light Emitters

About two thirds of the SWCNTs are direct bandgap semiconductors and show fluorescence from their lowest excitonic transition. However, photoluminescence was not detected from SWCNTs till 2002[41] when the process to individualize the SWCNTs using surfactants was discovered. This discovery paved the way for quick optical characterization of samples containing a wide range of possible chiralities of SWCNTs[3]. The direct band gap nature of SWCNTs has been exploited to make nanoscale light emitters using air-suspended SWCNTs. Figure(1.1c) shows electroluminescence from a SWCNT when holes and electrons injected into an ambipolar device configuration combine and radiatively decay [2]. Unlike conventional semiconductor p-n junctions, there is no need for chemical doping [13], and gate electrodes can be used to tune the local fermi energy levels inside the SWCNT. The light emission takes place from about a micron-sized length of the tube, and this length can be translated along the SWCNT using a combination of the gate and the source voltage. Another study has found evidence of photon antibunching in the fluorescence obtained from SWCNTs[21], which implies that SWCNTs may be used as a single photon source.

1.3 Stability of Excitons at Room Temperature in SWCNT

In 2005, it was shown by a study that employed two-photon excitation spectroscopy experiments that the optical absorption in SWCNT creates excitons[52].

The binding energy of the exciton was determined to be 400 meV, which was a significant fraction of the bandgap energy of 1.3 eV of the SWCNTs used in that study. Since the binding energy is significantly greater than room temperature thermal energy, these excitons are stable at room temperature. The exciton radius in that study was estimated to be 1.2 nm, and the density of the exciton envelope wavefunction is pictured in Figure(1.2). Note that the spatial extent of the exciton is larger than the unit cell size.

1.4 Potential Use of SWCNTs in Photovoltaics

SWCNTs can also be used as integrated photodetectors, and it has been recently demonstrated that there is efficient multiple electron-hole generation on photoexcitation at energies greater than the bandgap[14]. This could have important consequences for photovoltaics, as in most bulk materials there is rapid thermalization after photoexcitation at energies greater than the bandgap, which leads to an upper limit on the efficiency of solar cells, called the Shockley Queisser limit. It is interesting to note that the same SWCNT can be used as a transistor, light emitter or a light sensor just by modifying the voltages across the device[2]. This opens up the possibility of using SWCNTs as a platform for integrating optical technology with electronics at a nanoscale level[1].

1.5 SWCNT Saturable Absorbers for Mode-locking

SWCNTs have carved out a niche for themselves as saturable absorbers for passively mode-locking fiber lasers[54]. Their fast response, ease of saturation, and broad wavelength range due to various chiralities, makes them a good alternative to the III-V multi-quantum well mirrors that are traditionally used and involve expensive and complex MBE growth and have limited wavelength range. Additionally, tech-

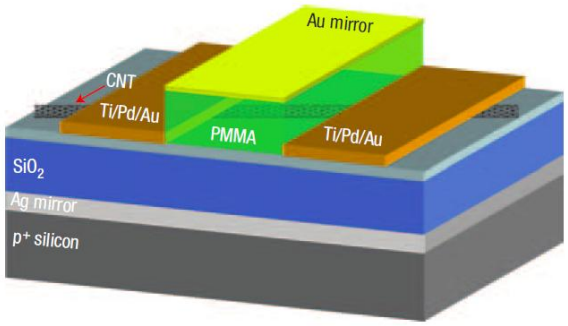

Figure 1.3: Device geometry of SWCNT embedded in a planar cavity with a Q of 40. Figure from [56].

niques have been developed which facilitate the deposition on SWCNTs on an optical fiber[37]. This eliminates the need for free space coupling which is required for the multi-quantum well mirrors. This has resulted in SWCNTs being used extensively to mode-lock fiber lasers.

1.6 Coupling SWCNTs to a Cavity

An important step towards active optical devices based on SWCNTs would be to interface them with optical cavities. Figure(1.3) depicts the schematic of a device used in a study[56] which estimated the enhancement of the radiative rate by a factor of 4, due to the cavity. There has not been a demonstration of a nanotube based laser to date, despite some evidence of optical gain[16]. It might be interesting to see if coupling of SWCNTs to high Q resonators can achieve lasing.

1.7 Nanophotonic Graphene Devices

Light-matter interaction in the underlying lattice structure that makes up the SWCNT is so strong, that a single atom thick layer of C atoms - graphene - can be seen with the naked eye[35] as shown is Figure(1.4a). This optical absorption of graphene

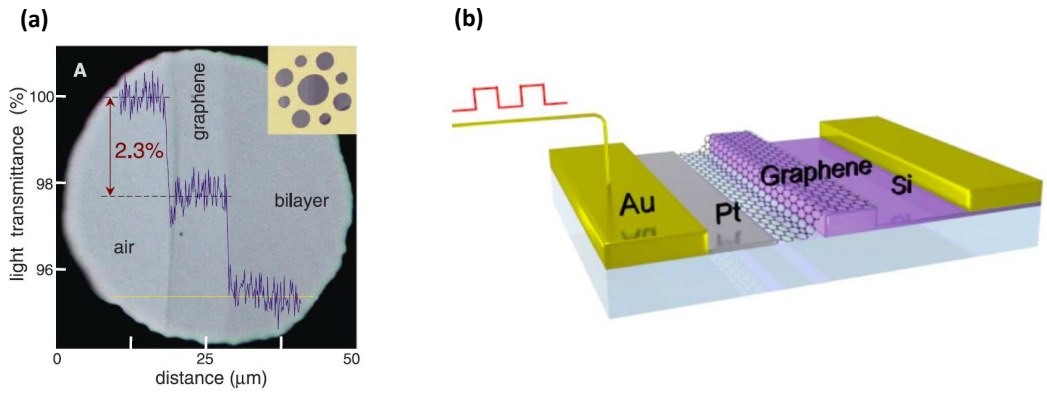

Figure 1.4: Graphene based photonics. (a) The strong optical absorption of graphene makes it visible to the naked eye [35] (b) The absorption can be tuned electrically, and this effect can be used to modulate light [29]. The graphene sheet interacts with the evanescent field of the optical mode in the waveguide.

is very broadband, staying constant over a wide range of energies. It has been found, that this optical absorption can also be changed through electrical gating[53]. This effect has been exploited to make broadband nanoscale optical modulators[29], a schematic for which is shown in Figure(1.4b). Such nanoscale optical modulators have a form factor of $25\,\mu m^2$, and can modulate at speeds exceeding 1 GHz. Other graphene-based photonic components that have already been demonstrated include broadband polarizers[4] and photodetectors[33].

1.8 Thesis Outline

In this chapter, some of the motivation that has driven intensive research on carbon based nanostructures in the recent past was discussed. For some of these applications to emerge, a thorough understanding is needed of the physical processes that determine the properties of these nanostructures. In this thesis, fundamental processes that lie at the heart of the interaction of resonant light with SWCNTs are considered. This chapter is concluded below by presenting an outline of this

dissertation.

Chapter II: Theoretical Prediction of Optical Excitation Induced Structural Changes in SWCNTs

The energy level structure that emerges for a SWCNT from considering the band-structure of graphene, along with boundary conditions on the azimuthal component of the wave-vectors of the charge carriers is depicted. The transitions between these energy levels, which are studied in optical measurements made in this thesis, are shown. Results of theoretical calculations are presented that predict structural distortions of SWCNTs due to excited excitonic population. From these results, it is inferred that an excitation induced shift in the resonant energy will happen for successive excitations on the SWCNT, and the experimental efforts in this thesis are devoted to measuring such effects using nonlinear optical spectroscopy techniques.

Chapter III: Nonlinear Optical Response and Pump-Probe Spectroscopy

Simple ideas behind differential transmission (dT), the main optical spectroscopy technique used in this thesis are presented. The formalism of semi-classical light matter interaction involving the density matrix approach is introduced.

Chapter IV: Signature of Excitation Induced Resonant Energy Shifts in Third Order Nonlinear Signals

The signature effects of an excitation induced change in the resonant energy in the time-resolved, homodyne detected third order nonlinear optical response is derived, considering a prototype 2-level system interacting with nearly resonant optical fields. This analysis leads to a prescription for analyzing experimental data, so that such effects can be made readily apparent.

Chapter V: Sample Characterization and Optical Setup

The techniques that are used to optically characterize the sample are shown. The experimental setups used for the nonlinear optical spectroscopy measurements is discussed.

Chapter VI: Experimental Observation of Excitation Induced Resonant Energy Shifts

Experimental data on the two color dT experiments on SWCNTs is shown. The Decay Associated Spectra (DAS) is extracted from the parameters obtained from global fits to this data. The characteristic lineshapes in the DAS is shown to reveal experimental detection of excitation induced shifts in the resonant energy. A tentative energy level model is proposed that will lead to some of the characteristics in the experimental DAS.

Chapter VII: Summary and Future Work

Future experiments are proposed that can test out some of the hypothesis in this thesis. The implications of this work to proposed SWCNT applications is discussed.

CHAPTER II

Theoretical Prediction of Optical Excitation Induced Structural Changes in SWCNTs

In this chapter, it will be shown that some basic understanding of the optical and electronic properties of SWCNTs can be achieved through a two step process: the bandstructure for the underlying graphene lattice can be derived in the tight binding scheme, and then a SWCNT can be imagined as a rolled up cylinder of this graphene sheet. Due to the the boundary conditions imposed on the azimuthal component of the wavevector in the rolled-up geometry, discrete energy levels emerge, and it is the energy separation between these levels that is studied in the optical measurements made in this thesis. Results from theoretical models are also presented from the literature that predict that a differential change in the SWCNT diameter is driven by optically excited population. Such distortions in the diameter of the SWCNT would lead to corrections in the bandgap energy, and hence will alter the spectral position of the energy resonance for exciting successive excitons on the SWCNT.

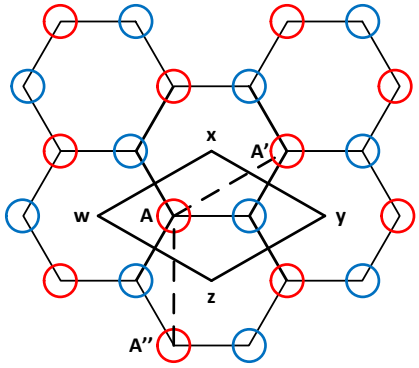

Figure 2.1: Hexagonal sheet of graphene is made up of two triangular sub-lattices. The lattice sites belonging to triangular sub-lattice A are color coded by red circles, and those belonging to sub-lattice B are color coded by blue circle. Alternatively, we can also say the unit cell of the sheet is the rectangle WXYZ comprising of two atoms.

2.1 Bandstructure of Graphene in the Tight Binding Scheme

The wavefunction of a single electron in a crystal satisfying the Bloch condition is of form

$$\psi = \sum_{A} \exp(2\pi i k R_A) X(r - R_A) \tag{2.1}$$

Here the sum is over the lattice points generated by the primitive vectors. $X(r - R_A)$ denotes the atomic orbital of the atom at a particular lattice site. For the case of graphene it is the $2p_z$ orbital of the C atoms that takes part in the band-formation. However, the honeycomb lattice of graphene can be thought to be comprised of two triangular sub-lattices A and B as shown in Figure 2.1. Hence the Bloch wavefunction is modified to include summation over both the sub-lattices[50]

$$\psi = \sum_{A} \exp(2\pi i k R_A) X(r - R_A) + \lambda \sum_{B} \exp(2\pi i k R_B) X(r - R_B) \tag{2.2}$$

To simplify, let us denote:

$$\phi_A = \sum_A \exp(2\pi i k R_A) X(r - R_A) \tag{2.3a}$$

$$\phi_B = \sum_B \exp(2\pi i k R_B) X(r - R_B) \tag{2.3b}$$

$$\Rightarrow \psi = \phi_A + \lambda \phi_B \tag{2.3c}$$

The wavefunction ψ must satisfy Schrödinger's equation:

$$H(\phi_A + \lambda \phi_B) = E(\phi_A + \lambda \phi_B) \tag{2.4}$$

By multiplying Equation((2.4)) by ϕ_A^* and integrating all over the lattice space we get:

$$\int \phi_A^* H \phi_A \, d\tau + \lambda \int \phi_A^* H \phi_A \, d\tau = E \int \phi_A^* \phi_A \, d\tau + E\lambda \int \phi_A^* \phi_B \, d\tau \tag{2.5}$$

We will assume that there is no overlap between the wavefunctions of any two distinct C atoms, and hence the term $\int \phi_A^* \phi_B \, d\tau$ will go to zero. We can then rearrange this equation to get:

$$\int \phi_A^* H \phi_A \, d\tau - E \int \phi_A^* \phi_A \, d\tau + \lambda \int \phi_A^* H \phi_B \, d\tau = 0 \tag{2.6}$$

Similarly by multiplying Equation((2.4)) by ϕ_B^* and integrating all over the lattice

space we get:

$$\int \phi_B^* H \phi_A \, d\tau + \lambda \left[\int \phi_B^* H \phi_B \, d\tau - E \int \phi_B^* \phi_B \, d\tau \right] = 0 \tag{2.7}$$

For there to be a consistent solution to Equation((2.6)) and Equation(2.7) we need the determinant of the matrix of the coefficients to be zero:

$$\begin{vmatrix} \int \phi_A^* H \phi_A \, d\tau - E \int \phi_A^* \phi_A \, d\tau & \int \phi_A^* H \phi_B \, d\tau \\ \int \phi_B^* H \phi_A \, d\tau & \int \phi_B^* H \phi_B \, d\tau - E \int \phi_B^* \phi_B \, d\tau \end{vmatrix} = 0 \tag{2.8}$$

Our aim is to solve this determinant for the eigenvalue energies E. Let us expand out $\int \phi_A^* \phi_A \, d\tau$ using Equation((2.3a))

$$\int \phi_A^* \phi_A \, d\tau = \int \sum_{A'} \exp(-2\pi i k R_A^{'}) X^*(r - R_A^{'}) \, d\tau \sum_A \exp(2\pi i k R_A) X(r - R_A) \tag{2.9}$$

We will neglect the overlap of the p_z wavefunction centered on different atoms. Hence only those terms will survive for which $A^{'} = A$. This gives us:

$$\int \phi_A^* \phi_A \, d\tau = \int \sum_A X^*(r - R_A) X(r - R_A) \, d\tau \tag{2.10}$$

The order of the integral and the summation can be exchanged in Equation((2.10)). Since the $2p_z$ wavefunction are normalized, the integral is unity. The sum is over the number of unit cells in the crystal which we can assume to be N. Since a similar argument holds also for $\int \phi_B^* \phi_B \, d\tau$ we get:

$$\int \phi_A^* \phi_A \, d\tau = \int \phi_B^* \phi_B \, d\tau = N \tag{2.11}$$

Substituting Equation((2.11)) in the determinant in Equation((2.8)), and solving for the eigen-energies, we get:

$$E = \frac{1}{N} \left[\int \phi_A^* H \phi_A \, d\tau \pm \left| \int \phi_A^* H \phi_B \, d\tau \right| \right] \tag{2.12}$$

The first term can be simplified to show that it is the energy associated with the bare $2p_z$ orbital, E_0:

$$\frac{1}{N} \int \phi_A^* H \phi_A \, d\tau = \int X^*(r - R_A) H X(r - R_A) \, d\tau = E_0$$

The positive and negative signs in Equation((2.12)) indicate that the parameter λ in Equation((2.2)) can assume values of ± 1. The positive (negative) value means that the neighboring atomic orbitals add constructively (destructively) and a *bonding*(*anti-bonding*) state is formed. The energy difference between the two bands is:

$$\Delta E = \frac{2}{N} \int \phi_A^* H \phi_B \, d\tau \tag{2.13}$$

We can use Equations((2.3a) ,(2.3b)) in Equation((2.13)) to get:

$$\Delta E = \frac{2}{N} \sum_A \sum_B \exp(-2\pi i k (R_A - R_B)) \int X^*(r - R_A) H X(r - R_B) \, d\tau \tag{2.14}$$

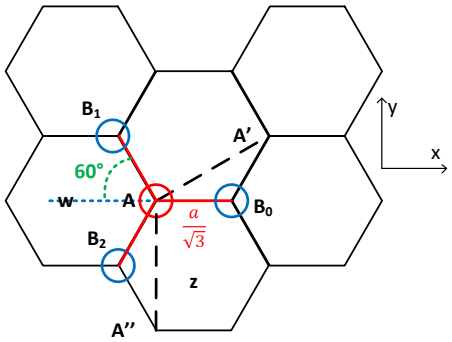

Figure 2.2: Nearest neighbors in graphene. The fundamental lattice displacements are $AA^{'} = AA^{''} = a = 0.142$nm. The nearest neighbor distance is $AB = AB_1 = AB_2 = \rho = \frac{a}{\sqrt{3}}$

Now for each atom belonging to the A sub-lattice we will compute only the contributions in the sum in Equation(2.14) due to three nearest neighbors from the B sub-lattice. These are depicted as the lattice sites B_0, B_1, B_2 in Figure(2.2). Also, we will denote the nearest neighbor overlap integral by:

$$\gamma = \int X^*(r - R_A) H X(r - R_B)\, d\tau \tag{2.15}$$

For each A atom there will only be three terms contributing in the summation over B lattice points as shown below:

1. B_0 :

$$\Delta E_{B_0} = \frac{2}{N} \sum_A \exp(-2\pi i k_x \frac{a}{\sqrt{3}})\gamma$$

The summation simply sums to N and we get:

$$\Delta E_{B_0} = 2\gamma \exp(-2\pi i k_x \frac{a}{\sqrt{3}}) \tag{2.16}$$

2. B_1 :

$$\Delta E_{B_1} = \frac{2}{N}\sum_A \exp(-2\pi i((-k_x\frac{a}{\sqrt{3}}\cos(60^\circ)) + (k_y\frac{a}{\sqrt{3}}\sin(60^\circ))))\gamma$$

$$\Rightarrow \Delta E_{B_1} = 2\gamma\exp(2\pi i k_x\frac{a}{2\sqrt{3}})\exp(-2\pi i k_y\frac{a}{2}) \quad (2.17)$$

3. B_2 :

$$\Delta E_{B_2} = \frac{2}{N}\sum_A \exp(-2\pi i((-k_x\frac{a}{\sqrt{3}}\cos(60^\circ)) - (k_y\frac{a}{\sqrt{3}}\sin(60^\circ))))\gamma$$

$$\Rightarrow \Delta E_{B_2} = 2\gamma\exp(2\pi i k_x\frac{a}{2\sqrt{3}})\exp(2\pi i k_y\frac{a}{2}) \quad (2.18)$$

On adding the expressions (2.16) – (2.18) together we get:

$$\Delta E = 2\gamma\exp(-2\pi i k_x\frac{a}{\sqrt{3}}) + 2\gamma\exp(2\pi i k_x\frac{a}{2\sqrt{3}})\exp(-2\pi i k_y\frac{a}{2}) \quad (2.19)$$
$$+2\gamma\exp(2\pi i k_x\frac{a}{2\sqrt{3}})\exp(2\pi i k_y\frac{a}{2})$$
$$\Rightarrow \Delta E = 2\gamma(\exp(-2\pi i k_x\frac{a}{\sqrt{3}}) + \exp(2\pi i k_x\frac{a}{2\sqrt{3}})(\exp(-2\pi i k_y\frac{a}{2}) + \exp(2\pi i k_y\frac{a}{2})))$$
$$\Rightarrow \Delta E = 2\gamma(\exp(-2\pi i k_x\frac{a}{\sqrt{3}}) + 2\exp(2\pi i k_x\frac{a}{2\sqrt{3}})\cos(2\pi k_y\frac{a}{2})) \quad (2.20)$$

On taking the square of the magnitude, we obtain:

$$|\Delta E|^2 = 4\gamma^2(\exp(-2\pi i k_x\frac{a}{\sqrt{3}}) + 2\exp(2\pi i k_x\frac{a}{2\sqrt{3}})\cos(2\pi k_y\frac{a}{2}))(\exp(2\pi i k_x\frac{a}{\sqrt{3}})$$
$$+ 2\exp(-2\pi i k_x\frac{a}{2\sqrt{3}})\cos(2\pi k_y\frac{a}{2}))$$
$$= 4\gamma^2(1 + 4\cos^2(\pi k_y a) + 2\cos(\pi k_y a)(\exp(i\pi k_x\sqrt{3}a) + \exp(-i\pi k_x\sqrt{3}a)))$$

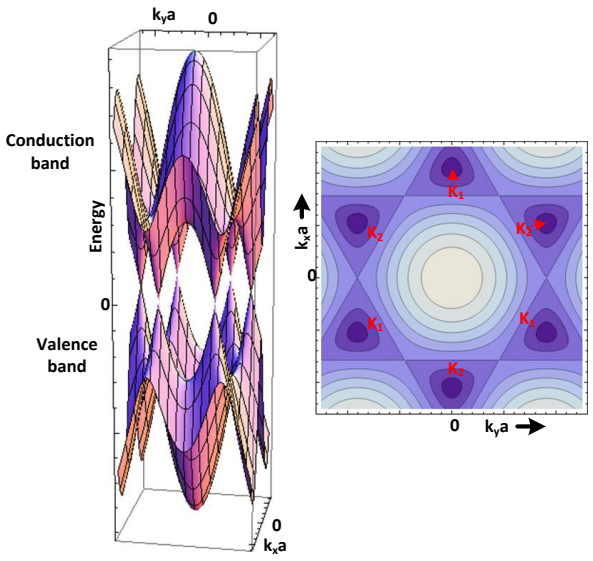

Figure 2.3: Bandstructure of Graphene.

$$\Rightarrow |\Delta E| = \pm 2\gamma \sqrt{1 + 4\cos^2(\pi k_y a) + 4\cos(\pi k_y a)\cos(\pi k_x \sqrt{3} a)} \tag{2.21}$$

In Figure(2.3) the dispersion relation given by Equation((2.21)) is plotted to visualize the bandstructure of graphene. Some of the exciting properties of graphene that become readily apparent from the bandstructure are briefly discussed below:

1. The conduction band and valence bands touch each other at six k-points in one Brillouin zone. This makes graphene a zero-bandgap semiconductor, or a semi-metal.

2. The dispersion around these 6 k-points is conical and is reminiscent of the dispersion of photons in vacuum. The effective mass of the charge carriers is given by:

$$m^* = \hbar^2 \left[\frac{d^2 E}{dk^2} \right]^{-1}$$

Since $\frac{d^2E}{dk^2}$ blows up at each of the 6 k-points, the effective mass of electrons and holes is zero in graphene near these k-points. The group velocity of the carriers is given by:

$$v_g = \frac{1}{\hbar}\frac{dE}{dk}$$

Hence the group velocity of electrons and holes in graphene is independent of their energies due to the linear dispersion near the six k-points. The carriers zip through graphene at an effective speed of light $c/300$, and act as massless Dirac fermions[39].

3. Out of the 6 k-points, there are two sets of distinct points denoted by K_1 and K_2 in Figure(2.3). This leads to an orbital degeneracy of two, in addition to the two-fold spin degeneracy.

2.2 Zone Folding Scheme for SWCNT

A SWCNT can be imagined as a rolled up cylinder from a graphene sheet. In Figure(2.4a), a 2D graphene sheet is depicted along with the lattice vectors $\vec{a}_1$ and $\vec{a}_2$ whose magnitude is a. The green arrow represents the SWCNT roll up vector $\vec{R} = n\vec{a}_1 + m\vec{a}_2$, with the dotted red lines coming together as the SWCNT is formed. The chiralities of various SWCNT that can be formed are indicated by the (n, m) indices written at the end of the roll up vector.

We will now limit the discussion to zigzag SWCNTs ($m = 0$) depicted in Figure(2.4b). For satisfying the boundary condition, the wavefunction for a charge carrier in a SWCNT will have to repeat itself about the circumference:

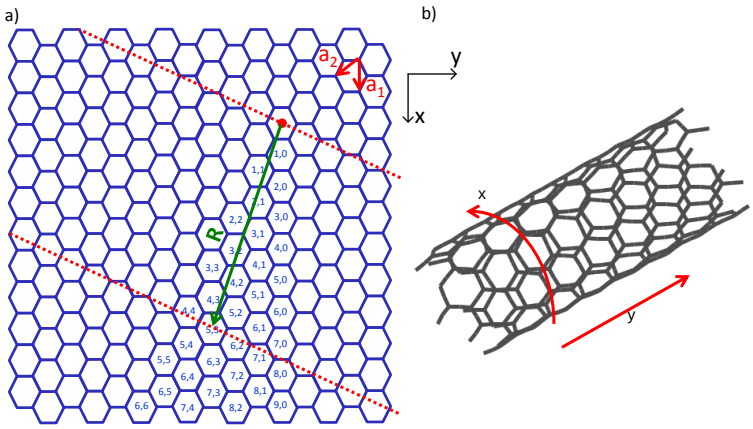

Figure 2.4: SWCNT visualized as rolled up cylinders from graphene. a) The graphene sheet with a few chiralities of SWCNTs that can be formed are labeled. b)Geometry for a zigzag ($m = 0$) SWCNT. SWCNT figure credit:[32]

$$\begin{aligned} \psi(x,y) =& \psi(x + 2\pi r, y) \\ =& \exp(ik_x 2\pi r)\psi(x,y) \qquad (2.22) \\ \Rightarrow k_x =& \frac{j}{r} \qquad (2.23) \end{aligned}$$

Here j is any integer. Hence only certain values of the azimuthal component of the angular momentum are permitted in a SWCNT for the charge carriers. If an allowed k_x state passes through any of the 6 k-points where the conduction and valence band meet for the graphene sheet, then the SWCNT will be metallic, otherwise a bandgap emerges leading to a direct bandgap semiconductor. It can be shown that the condition for metallic/semiconductor nature depends on the geometry of the roll-up, and can be expressed as[24]

$$\text{mod}\ ((n-m), 3) = 0 : \text{metallic}$$

$$\text{mod}\ ((n-m), 3) = 1, 2 : \text{semiconducting}$$

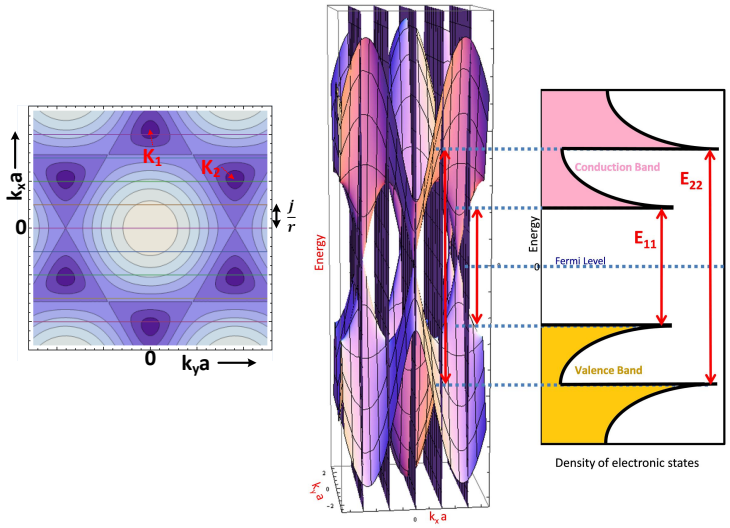

Figure 2.5: Bandstructure and energy level diagram for SWCNT.

Hence, roughly one third of the SWCNTs are metallic, and the rest are direct bandgap semiconductors. There are two families of semiconducting SWCNTs depending on the value of $\text{mod}((n-m),3)$. We will denote the family with $\text{mod}((n-m),3) = 1$ as mod(1), and the other family as mod(2).

The energy difference between two successive allowed states for the azimuthal component of the wavevector is on the order of 1eV. Since this difference is large compared to room temperature thermal energy, there is only one remaining degree of freedom (the longitudinal component of the wavevector) and thus, a SWCNT forms a very ideal 1-D system.

In Figure(2.5) we have depicted the allowed k_x states for a semiconducting zigzag tube, and the energy levels that emerge. The allowed states for the nanotube are visualized by the intersection of the cutting planes representing the allowed k_x values, with the bandstructure of graphene. The density of states of the energy levels that emerge at the intersection scales as $(E - E_i)^{-\frac{1}{2}}$ as for a one dimensional system. The two lowest direct bandgap optically allowed transitions E_{11} and E_{22} are also shown in Figure(2.5). The allowed optical transitions are characterized by two subscripts:

the first denotes the index of the valence band state in which the hole is created, and the second the index of the conduction band state where the electron is created. Since the charge carriers have a quantized value of angular momentum along the SWCNT axis, in the dipole approximation only transitions of the form E_{ii}, where the excited electron and hole have equal and opposite values of the circumferential angular momentum are allowed.

From what we have considered so far it would seem, that assuming a linear dispersion for graphene, and the azimuthal wave-vector quantization relation given by Equation(2.22), the energy spacings between the levels will scale inversely as the SWCNT diameter. In fact, there are many mechanisms that lead to deviations from this simple picture. For example, the markedly enhanced Coulomb interaction in this one dimensional system, which leads to the optical excitations being dominated by excitonic effects[52] leads to corrections to the energy spacing. There are also effects due to curvature[19] and a chirality-dependent trigonal warping effect[44] that also influence the energy separation. The dependance of the energy of the E_{22} resonance for particular chiral angles of the SWCNTs that are considered in this thesis, on the diameter has been empirically determined by fitting photoluminescence excitation (PLE) data for various chiralities as[3]:

$$\epsilon_{22}(\mathrm{cm}^{-1}) = \frac{10^7}{145.6 + 575.6d} + \frac{687.5}{d^2}$$

where d is the tube diameter in nm. Substituting $d = 0.8$nm in this formula gives us $\epsilon_{22} = 569\,\mathrm{nm}$, which as it will be shown in Chapter(V) is close to the position of the E_{22} transition measured for the $(6, 5)$ SWCNTs used in this thesis.

2.3 Theoretical Predictions of Optical Excitation Induced Structural Changes in SWCNT

Recent theoretical work predicts that optically exciting carriers into the E_{22} or E_{11} levels causes structural changes in a SWCNT, especially the distortion of the SWCNT in the radial direction[45] due to strong electron-phonon couplings in this system. This effect can be understood in the context of molecules where there is a certain equilibrium position of the nuclei when the electron cloud is in the ground state. This equilibrium distance between the nuclei is determined by the configuration that minimizes the energy of the molecule. However, in general, the equilibrium position of the nuclei that minimizes the configurational energy changes from their position in the ground state, when the electron cloud is excited. For nanotubes, such a change in the radial position of the nuclei on optical excitation of the excitonic population will lead to corrections in the bandgap energy, that would either decrease/increase the energy separation between the levels that emerge from the periodic boundary condition in the azimuthal direction. It is predicted that the tube diameter can either increase or decrease depending on which energy level gets populated, and also which family type the SWCNT belongs too, and hence, both blue and red shifts in the resonant energy are predicted. In the theoretical models, the change in diameter is driven by the excited state populations. The upper limit on the exciton density for the $(6, 5)$ chirality studied in this thesis has been inferred to be about 1.6×10^6 excitons/cm[46] before saturation effects set in. For the average length of about 1μm for the SWCNTs in the samples studied in this thesis, this number corresponds to about 160 excitons per nanotube. The theory also predicts diameter oscillations at early times subsequent to femtosecond optical excitation. The resulting oscillation in the energy level has been inferred by femtosecond dT/T measurements where the probe transmission gets modulated at the frequency of the coherent phonon mode excited[15, 25]. These

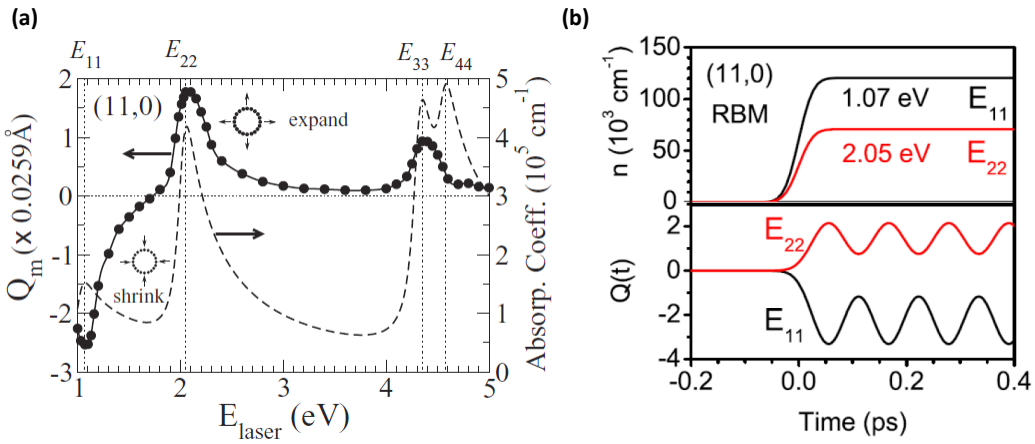

Figure 2.6: Results of theoretical calculations predicting change in diameter of (11,0) SWCNT belonging to mod(2) family upon optical excitation. (a) Plots of the phonon amplitude with the linear absorption. (b)Top:Photoexcited carrier density due to optical excitation at the E_{11} (black) and E_{22} (red) energy levels. Bottom: The tube diameter initially increases(decreases) for excitation at the $E_{22}(E_{11})$ energy level and then oscillates around the new equilibrium position. Figure adapted from [40] and [45].

results will be shown in Chapter(VI). Using narrower band picosecond pulses we are interested in detecting any spectral changes in the resonant energy of the E_{22} transition, as seen in the probe spectra of the time resolved optical nonlinear signal, after photoexcitation by a pump pulse at the E_{22} energy level.

A phonon amplitude $Q(t)$ can be defined which governs the motion of the C atoms in phase, in the the radial direction. $Q(t)$ is proportional to the differential change in the diameter of the tube. It has been shown, that the steady state value of $Q(t)$ depends on the photoexcited carrier distribution function $\delta f(k,t)$ [45]

$$Q(t) \propto -\frac{2\omega_q}{\hbar} \sum_k M_{el-ph}(k)\, \delta f(k,t)$$

where $M_{el-ph}(k)$ is the k -dependent radial breathing mode (RBM) matrix element. In Figure (2.6a), the differential change in diameter of a $(11,0)$ SWCNT (belonging to the mod(2) family) is plotted as a function of the excitation energy re-

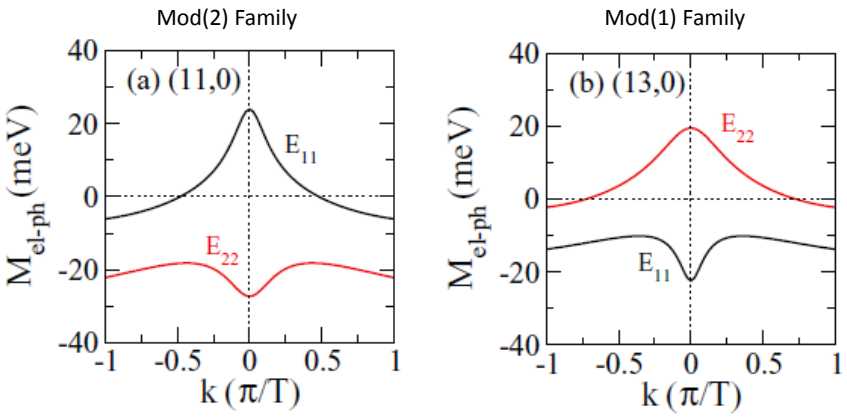

Figure 2.7: The sign of the electron-phonon matrix element changes sign for excited state population in either E_{22} or E_{11} state for a given family of SWCNTs. The matrix element also changes signs between the mod(1) and mod(2) families. Figure from [40]

sponsible for optical excitation. In Figure (2.6b), the results of a calculation assuming 50 fs excitation pulse is reproduced from[45], which predicts that the SWCNT diameter oscillates at the RBM frequency. For the SWCNTs belonging to mod(2) family like the $(11, 0)$ chirality, photoexcitation at the E_{11} energy level causes the tube diameter to initially decrease and then oscillates around a smaller equilibrium diameter. Conversely, photoexcitation at the E_{22} energy level causes the tube diameter to expand and oscillate around a larger tube diameter. Note that in these theoretical models, population decay timescales have been ignored. With the inclusion of population decay, we guess that the SWCNT diameter will relax back to its ground state equilibrium position as the excited state population decays.

The theoretical prediction for mod(1) family of tubes is reversed from what was just stated, as the theory predicts a change in the signs of M_{el-ph} between the mod(1) and mod(2) families. This is shown in Figure(2.7). Another theoretical study[42] has also indicated that the nanotube lattice distorts dynamically in the presence of a single exciton (the position of which is assumed to be fixed in this calculation), and that this distortion is long ranged as shown in Figure(2.8). This study also found a

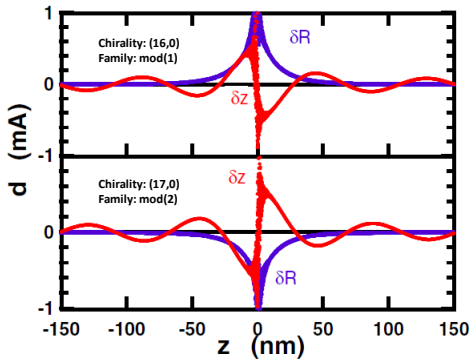

Figure 2.8: Calculated lattice distortion of SWCNTs due to the presence of an exciton in the E_{11} state for the two SWCNT families. The hole is assumed to be fixed at the origin. The atomic displacements in the radial direction are given by δR and the displacements parallel to the SWCNT axis are given by δz. Figure from [42]

change in the sign of the radial distortion between the two families of SWCNT, and also between excitons in the E_{11} and E_{22} states.

The theoretical results presented in this section imply that for the $(6, 5)$ chirality SWCNTs belonging to the mod(1) family that are studied in this thesis, the excited state population in the E_{22} (E_{11}) state will result in a decrease (increase) in the SWCNT diameter, which would cause a blue (red) shift in the resonant energy. It is this excitation induced change in the spectral position of the E_{22} resonance that we aim to measure using time-resolved nonlinear optical spectroscopy techniques with narrow-band picosecond pulses. Basic concepts for understanding these techniques are presented in Chapter(III).

2.4 Chapter Summary

In this chapter, the bandstructure of graphene was presented within a tight binding method. Some of the novel properties of this material were sought to be explained on the basis of the unique nature of its bandstructure. For a SWCNT, the azimuthal boundary conditions around the circumference leads to cutting planes in the band-

structure of graphene, where discrete energy levels emerge that are characterized by the one dimensional density of states. This makes some of the SWCNTs direct bandgap semiconductors, with their optical properties being dominated by excitonic effects due to increased coulomb interactions in this reduced dimensionality system. The energy spacing between these levels is a function of the SWCNT diameter. Results of microscopic theories from the literature were presented, which indicate that due to strong excitonic-phonon coupling in SWCNTs, optically excited population in these energy states will drive a differential change in the SWCNT diameter. Such a distortion in the SWCNT diameter is expected to change the spacing between the energy levels, an effect that we will seek to measure using techniques of time-resolved nonlinear optical spectroscopy.

CHAPTER III

Nonlinear Optical Response and Pump-Probe Spectroscopy

In this chapter some simple concepts are presented about differential transmission(dT) - the main optical spectroscopy technique used in this dissertation. This is followed up with a more formal semi-classical formulation of light matter interaction where an understanding is sought on the physical mechanism by which the nonlinear optical signal can be measured with this technique. Lastly, some data is presented on a test sample in which the some of the terms contributing to the nonlinear signal can be identified.

3.1 Introduction to Differential Transmission

In simplest terms, differential transmission is the change in the transmission of a probe beam due to a nonlinear optical response generated in the sample by a pump beam. The dT signal can be expressed as:

$$I_{\text{signal}} = I_{\text{probe,pump on}} - I_{\text{probe,pump off}} \tag{3.1}$$

where, $I_{\text{probe,pump on}}$ is the photocurrent generated in a detector in the probe path when the pump beam is on, and $I_{\text{probe,pump off}}$ is the photocurrent generated in the same detector when the pump is off. Let the linear response of the sample to the probe field E_{probe} be given by $E^{(1)}_{\text{probe}}$. For centrosymmetric materials (materials having inversion symmetry[6]), the next order response will be $E^{(3)}_{\text{probe}}$. Neglecting higher order responses due to their diminishing contribution we get

$$I_{\text{signal}} \propto \left| E_{\text{probe}} + E^{(1)}_{\text{probe}} + E^{(3)}_{\text{probe}} + E^{(3)}_{\text{pump,probe}} \right|^2 - \left| E_{\text{probe}} + E^{(1)}_{\text{probe}} + E^{(3)}_{\text{probe}} \right|^2 \quad (3.2)$$

where the response $E^{(3)}_{\text{pump,probe}}$ can be written as a cross-term involving both the pump and probe fields:

$$E^{(3)}_{\text{pump,probe}} \propto \chi^{(3)} E_{\text{pump}} E^*_{\text{pump}} E_{\text{probe}} \quad (3.3)$$

The justification for this kind of a term will be developed later in this chapter. We can now simplify

$$\begin{aligned} I_{\text{signal}} \propto & \left| E_{\text{probe}} + E^{(1)}_{\text{probe}} + E^{(3)}_{\text{probe}} \right|^2 + \left| E^{(3)}_{\text{pump,probe}} \right|^2 \\ & + 2\text{Re}(E^{(3)}_{\text{pump,probe}}(E_{\text{probe}} + E^{(1)}_{\text{probe}} + E^{(3)}_{\text{probe}})^*) \\ & - \left| E_{\text{probe}} + E^{(1)}_{\text{probe}} + E^{(3)}_{\text{probe}} \right|^2 \end{aligned}$$

We can neglect $\left| E^{(3)}_{\text{pump,probe}} \right|^2$ to get:

$$I_{\text{signal}} \propto 2\text{Re}(E^{(3)}_{\text{pump,probe}}(E_{\text{probe}} + E^{(1)}_{\text{probe}} + E^{(3)}_{\text{probe}})^*) \quad (3.4)$$

By neglecting $E^{(1)}_{\text{probe}}$ and $E^{(3)}_{\text{probe}}$ in comparison with E_{probe} we obtain:

$$I_{\text{signal}} \propto 2\text{Re}(E^{(3)}_{\text{pump,probe}} E^{*}_{\text{probe}}) \tag{3.5}$$

This equation shows that the dT signal is proportional to the third order optical response of the sample, homodyne detected with the probe. Furthermore, we can make use of Equation(3.3) to obtain:

$$I_{\text{signal}} \propto \chi^{(3)} \left|E_{\text{pump}}\right|^2 \left|E_{\text{probe}}\right|^2 \tag{3.6}$$

Thus we see that the dT signal will scale linearly with both the pump and probe powers in the $\chi^{(3)}$ limit. In the next section, a formalism that helps describe light matter interaction will be discussed. It is within this formalism, that the $\chi^{(3)}$ response measured in a dT experiment, can be calculated.

3.2 Semiclassical Theory of Light-Matter Interaction

In many cases, the interaction of light resonantly with a material system can be approximated to a problem consisting of two quantum levels interacting with a classical field[5]. We can describe the two level system, without considering the effects of the optical field by a Hamiltonian $\hat{H}_0$, with the eigenfunctions $|0\rangle$ and $|1\rangle$ satisfying the time independent Schrodinger equation:

$$\begin{aligned} \hat{H}_0|0\rangle &= \mathcal{E}_0|0\rangle \\ \hat{H}_0|1\rangle &= \mathcal{E}_1|1\rangle \end{aligned}$$

In the energy basis, the Hamiltonian is simply the diagonal matrix:

$$\hat{H}_0 = \begin{pmatrix} \mathcal{E}_0 & 0 \\ 0 & \mathcal{E}_1 \end{pmatrix}$$

The interaction of light with this two level system modifies the Hamiltonian to be of the form $\hat{H} = \hat{H}_0 + \hat{V}(t)$ where the perturbation $\hat{V}(t)$ in the dipole approximation[5, 6] can be written as:

$$\hat{V}(t) = \hat{\mu}E(t)$$

Here $\hat{\mu}$ is the dipole operator and can be written as $\hat{\mu} = e\hat{r}$,where $\hat{r}$ is the position operator. Since the position operator typically has odd parity, the diagonal matrix elements of $\hat{r}$ go to zero. Hence, the operator $\hat{V}(t)$ has only off-diagonal elements. The perturbation to the original Hamiltonian is considered to be small, so any state vector can be expanded using the unperturbed eigenfunctions of $\hat{H}_0$:

$$|\psi(t)\rangle = \sum_n a_n(t)|n\rangle \tag{3.7}$$

The time evolution of the wavefunction is governed by Schrödinger's equation:

$$i\hbar\frac{\partial}{\partial t}|\psi(t)\rangle = \left(\hat{H}_0 + \hat{V}(t)\right)|\psi(t)\rangle \tag{3.8}$$

We can substitute Equation(3.7) in Equation(3.8) to get:

$$i\hbar\frac{\partial}{\partial t}\left(\sum_n a_n(t)|n\rangle\right) = \left(\sum_n a_n(t)\mathcal{E}_n|n\rangle\right) + \hat{V}(t)\left(\sum_n a_n(t)|n\rangle\right) \tag{3.9}$$

Multiplying (3.9) by $\langle m|$ and using the fact that the eigenvectors are orthonormal, we get:

$$i\hbar\frac{\partial}{\partial t}a_m(t) = \mathcal{E}_m|m\rangle + \sum_n \langle m|\hat{V}(t)|n\rangle a_n(t)$$

This equation can be recast into the following matrix equation[5]:

$$i\hbar\dot{\boldsymbol{a}}(t) = \hat{H}_0\boldsymbol{a}(t) + \hat{V}(t)\boldsymbol{a}(t) \tag{3.10}$$

The above equation of motion can be conceptually simplified by moving to the interaction representation, in which the time varying part of $a(t)$ that is due to the unperturbed Hamiltonian H_0 is pulled out:

$$|\psi(t)\rangle = \sum_n e^{-i\mathcal{E}_n t/\hbar} c_n |n\rangle$$

The matrices of the two sets of coefficients are related as:

$$\boldsymbol{a}(t) = U_0(t)\boldsymbol{c}(t) \tag{3.11}$$

Where $U_0(t)$ is the time evolution operator and is given by:

$$U_0(t) = e^{-i\hat{H}_0 t/\hbar} \tag{3.12}$$

Using Equation(3.10), we get:

$$i\hbar\left(U_0(t)\dot{\boldsymbol{c}}(t) + \dot{U}_0(t)\boldsymbol{c}(t)\right) = \hat{H}_0 U_0(t)\boldsymbol{c}(t) + \hat{V}(t)U_0(t)\boldsymbol{c}(t) \tag{3.13}$$

By differentiating Equation(3.12), we get:

$$\dot{U}_0(t) = -\frac{i}{\hbar}\hat{H}_0 U_0(t) \tag{3.14}$$

By using the time derivative of the time evolution operator given by Equation(3.14) in Equation(3.13), we will find that the second term on the left hand side, will cancel with the first term on right hand side. Thus the following is obtained:

$$U_0(t)\dot{\boldsymbol{c}}(t) = -\frac{i}{\hbar}\hat{V}(t)U_0(t)\boldsymbol{c}(t) \tag{3.15}$$

By multiplying Equation(3.15) by $U_0^\dagger(t)$, we get:

$$\dot{\boldsymbol{c}}(t) = -\frac{i}{\hbar}U_0^\dagger(t)\hat{V}(t)U_0(t)\boldsymbol{c}(t) \tag{3.16}$$

The Interaction Hamiltonian can be defined as follows[5]:

$$\hat{V}^I(t) = U_0^\dagger(t)\hat{V}(t)U_0(t) = U_0^\dagger(t)\hat{\mu}.E(t)U_0(t) = E(t)U_0^\dagger(t)\hat{\mu}U_0(t)$$

Here, the dipole operator in the interaction representation can be written as:

$$\hat{\mu}(t) = U_0(t)^\dagger\hat{\mu}U_0(t) \tag{3.17}$$

Thus we get for the interaction Hamiltonian:

$$\hat{V}^I(t) = E(t)\hat{\mu}(t) \tag{3.18}$$

Using the definition of the interaction Hamiltonian, Equation(3.16) can be written as

$$\dot{\boldsymbol{c}}(t) = -\frac{i}{\hbar}\hat{V}^I(t)\boldsymbol{c}(t) \tag{3.19}$$

Often, the results of experiments are impossible to describe using just the wave-function picture. This is because a quantum system in the laboratory almost always interacts with a bath, and we often have no way of knowing all the quantum states in the bath. The effects caused by interaction with a bath, for example, pure dephasing due to "collision" type processes, and spontaneous emission due to interaction with the vacuum field can be phenomenologically included in what is known as the density matrix picture[34, 6]. Moreover, if we are dealing with ensembles, it is not possible

to write a wavefunction, and a density matrix is defined as follows:

$$\rho = \sum_s p(s)|\psi_s\rangle\langle\psi_s|$$

where the $p(s)$ is the statistical probability of finding the system in a pure state $|\psi_s\rangle$. In this picture, it can be shown that the expectation value of an operator is given by:

$$\langle A\rangle = \mathrm{Tr}\,(\mathrm{A}\rho) \tag{3.20}$$

In terms of the amplitudes, the density matrix is defined as:

$$\rho(t) = \boldsymbol{a}(t)\boldsymbol{a}^{\dagger}(t)$$

Making use of Equation(3.11), we get:

$$\rho(t) = U_0(t)\boldsymbol{c}(t)\boldsymbol{c}^{\dagger}(t)U_0^{\dagger}(t)$$

We define the density matrix in the interaction representation by:

$$\rho^I(t) = \boldsymbol{c}(t)\boldsymbol{c}^{\dagger}(t) \tag{3.21}$$

and the density matrices in the two representations are related by:

$$\rho(t) = U_0(t)\rho^I(t)U_0^{\dagger}(t) \tag{3.22}$$

It is important to note that in calculating expectation values using Equation (3.20), the density matrix in the interaction representation has to be converted back to the Schrödinger picture[5]. Now we can take the time derivative of Equation(3.21) to obtain:

$$\frac{d\rho^I(t)}{dt} = \dot{\boldsymbol{c}}(t)\boldsymbol{c}^\dagger(t) + \boldsymbol{c}(t)\dot{\boldsymbol{c}}^\dagger(t)$$

We can use the equation of motion for $\boldsymbol{c}(t)$ given by Equation(3.19), to obtain:

$$\begin{aligned}\frac{d\rho^I(t)}{dt} &= -\frac{i}{\hbar}\left(\hat{V}^I(t)\boldsymbol{c}(t)\boldsymbol{c}^\dagger(t) - \boldsymbol{c}(t)\boldsymbol{c}^\dagger(t)\hat{V}^I(t)\right) \\ &= -\frac{i}{\hbar}\left(\hat{V}^I(t)\rho^I(t) - \rho^I(t)\hat{V}^I(t)\right)\end{aligned}$$

We can identify the commutator on the right hand side to obtain:

$$\frac{d\rho^I(t)}{dt} = -\frac{i}{\hbar}\left[\hat{V}^I(t), \rho^I(t)\right] \tag{3.23}$$

As was mentioned earlier, relaxation terms are added phenomenologically to this equation to account for pure dephasing and spontaneous emission[5]. In the next section, this equation of motion for the density matrix will be perturbatively solved. We will not consider the decay terms right now, since the emphasis of the next section is to show the physics behind perturbation pathways and time ordering that determines the nonlinear response. We will start to include the decay terms in Chapter(IV) where we will use the equations of motion to describe physical models that have some relevance to our experiments.

3.3 Perturbation Calculation of 3^{rd} Order Optical Response

We can integrate[34, 20] Equation(3.23) from $t = -\infty$ to $t = t$ to get:

$$\rho^I(t) = \rho^I(-\infty) - \frac{i}{\hbar}\int_{-\infty}^{t} \mathrm{d}\tau \left[\hat{V}^I(\tau), \rho^I(\tau)\right]$$

Now we plug the above expression for $\rho^I(t)$ into the $\rho^I(\tau)$ appearing in the commutator to obtain:

$$\begin{aligned}
\rho^I(t) &= \rho^I(-\infty) - \frac{i}{\hbar}\int_{-\infty}^{t} \mathrm{d}\tau \left[\hat{V}^I(\tau), \rho^I(-\infty) - \frac{i}{\hbar}\int_{-\infty}^{\tau} \mathrm{d}\tau_1 \left[\hat{V}^I(\tau_1), \rho^I(\tau_1)\right]\right] \\
&= \rho^I(-\infty) - \frac{i}{\hbar}\int_{-\infty}^{t} \mathrm{d}\tau \left[\hat{V}^I(\tau), \rho^I(-\infty)\right] + \\
&\quad \left(-\frac{i}{\hbar}\right)^2 \int_{-\infty}^{\tau_2} \mathrm{d}\tau_2 \left[\hat{V}^I(\tau_2), \left[\hat{V}^I(\tau_1), \rho^I(\tau_1)\right]\right]
\end{aligned}$$

where we have changed the the label of the integration variable from τ to τ_2 for the right most integral. We can repeat this process to obtain the series:

$$\begin{aligned}
\rho^I(t) &= \rho^I(-\infty) + \sum_{n=1}^{\infty} \left(-\frac{i}{\hbar}\right)^n \int_{-\infty}^{t} \mathrm{d}\tau_n \int_{-\infty}^{\tau_n} \mathrm{d}\tau_{\mathrm{n}-1} \int_{-\infty}^{\tau_{\mathrm{n}-1}} \mathrm{d}\tau_{\mathrm{n}-2} \ldots \int_{-\infty}^{\tau_2} \mathrm{d}\tau_1 \\
&\quad \left[\hat{V}^I(\tau_n), \left[\hat{V}^I(\tau_{n-1}), \left[\hat{V}^I(\tau_{n-2}), \ldots \left[\hat{V}^I(\tau_1), \rho^I(-\infty)\right] \ldots\right]\right]\right]
\end{aligned}$$

Since we are interested in computing the expectation value of the dipole operator using the density matrix, we will have to move back to the density matrix in the Schrödinger picture by using Equation(3.22). We will denote the first term in the new series by $\rho^{(0)}(t) = U_0(t)\rho^I(-\infty)U_0^\dagger(t)$, which is the solution to the zeroth order in the fields. Hence we get an expansion of $\rho(t)$ in powers of the applied fields, which can be expressed as:

$$\rho(t) = \rho^{(0)}(t) + \sum_{n=1}^{\infty} \rho^{(n)}(t)$$

where the n^{th} order response is given by

$$\rho^{(n)}(t) = \left(-\frac{i}{\hbar}\right)^n \int_{-\infty}^{t} \mathrm{d}\tau_n \int_{-\infty}^{\tau_n} \mathrm{d}\tau_{\mathrm{n-1}} \int_{-\infty}^{\tau_{\mathrm{n-1}}} \mathrm{d}\tau_{\mathrm{n-2}} ... \int_{-\infty}^{\tau_2} \mathrm{d}\tau_1$$
$$U_0(t) \left[\hat{V}^I(\tau_n), \left[\hat{V}^I(\tau_{n-1}), \left[\hat{V}^I(\tau_{n-2}), ... \left[\hat{V}^I(\tau_1), \rho(-\infty)\right] ...\right]\right]\right] U_0(t)^\dagger$$

Now, we will use the definition of the interaction Hamiltonian given by Equation (3.18) to get:

$$\rho^{(n)}(t) = \left(-\frac{i}{\hbar}\right)^n \int_{-\infty}^{t} \mathrm{d}\tau_n \int_{-\infty}^{\tau_n} \mathrm{d}\tau_{\mathrm{n-1}} \int_{-\infty}^{\tau_{\mathrm{n-1}}} \mathrm{d}\tau_{\mathrm{n-2}} ... \int_{-\infty}^{\tau_2} \mathrm{d}\tau_1 \, U_0(t)$$
$$[E(\tau_n)\hat{\mu}(\tau_n), [E(\tau_{n-1})\hat{\mu}(\tau_{n-1}), [E(\tau_{n-2})\hat{\mu}(\tau_{n-2}), ... [E(\tau_1)\hat{\mu}(\tau_1), \rho(-\infty)] ...]]]$$
$$U_0(t)^\dagger$$

We can pull out all the electric field terms from inside the commutators to get:

$$\rho^{(n)}(t) = \left(-\frac{i}{\hbar}\right)^n \int_{-\infty}^{t} \mathrm{d}\tau_n \int_{-\infty}^{\tau_n} \mathrm{d}\tau_{\mathrm{n-1}} \int_{-\infty}^{\tau_{\mathrm{n-1}}} \mathrm{d}\tau_{\mathrm{n-2}} ... \int_{-\infty}^{\tau_2} \mathrm{d}\tau_1 E(\tau_n)E(\tau_{n-1})E(\tau_{n-2})...E(\tau_1)$$
$$U_0(t) \left[\hat{\mu}(\tau_n), [\hat{\mu}(\tau_{n-1}), [\hat{\mu}(\tau_{n-2}), ... [\hat{\mu}(\tau_1), \rho(-\infty)] ...]]\right] U_0(t)^\dagger$$

We are mainly interested in the third order response in the fields, we get:

$$\rho^{(3)}(t) = \left(-\frac{i}{\hbar}\right)^3 \int_{-\infty}^{t} \mathrm{d}\tau_3 \int_{-\infty}^{\tau_3} \mathrm{d}\tau_2 \int_{-\infty}^{\tau_2} \mathrm{d}\tau_1 E(\tau_3)E(\tau_2)E(\tau_1)$$
$$U_0(t) \left[\hat{\mu}(\tau_3), [\hat{\mu}(\tau_2), [\hat{\mu}(\tau_1), \rho(-\infty)]]\right] U_0(t)^\dagger$$

The expectation value of the dipole moment operator is the macroscopic polarization induced by the the incident fields. As we will show later in this chapter, this macroscopic polarization produced in the material acts as a source term in Maxwell's equation, and leads to the creation of the fields that are generated by the material in response to the incident fields. The macroscopic polarization induced is the expectation value of the dipole operator:

$$P(t) = \langle \hat{\mu} \rangle = \mathrm{Tr}(\hat{\mu}\rho(\mathrm{t}))$$

Since the density matrix can be written in the form of an expansion series, the same can be done for the induced polarization to get:

$$P(t) = P^{(0)}(t) + \sum_{n=1}^{\infty} P^{(n)}(t)$$

where the n^{th} order induced polarization can be expressed as:

$$\begin{aligned} P^{(n)}(t) &= \left(-\frac{i}{\hbar}\right)^n \int_{-\infty}^{t} \mathrm{d}\tau_n \int_{-\infty}^{\tau_n} \mathrm{d}\tau_{\mathrm{n-1}} \int_{-\infty}^{\tau_{\mathrm{n-1}}} \mathrm{d}\tau_{\mathrm{n-2}} ... \int_{-\infty}^{\tau_2} \mathrm{d}\tau_1 E(\tau_n)E(\tau_{n-1})E(\tau_{n-2})...E(\tau_1) \\ &\quad \mathrm{Tr}\left(\hat{\mu}U_0(t)\left[\hat{\mu}(\tau_n),[\hat{\mu}(\tau_{n-1}),[\hat{\mu}(\tau_{n-2}),...\left[\hat{\mu}(\tau_1),\rho(-\infty)\right]...\right]\right]U_0(t)^{\dagger}\right) \end{aligned}$$

The trace operation in insensitive to cyclical permutation, so by rearranging the terms inside the trace we get:

$$\begin{aligned} P^{(n)}(t) &= \left(-\frac{i}{\hbar}\right)^n \int_{-\infty}^{t} \mathrm{d}\tau_n \int_{-\infty}^{\tau_n} \mathrm{d}\tau_{\mathrm{n-1}} \int_{-\infty}^{\tau_{\mathrm{n-1}}} \mathrm{d}\tau_{\mathrm{n-2}} ... \int_{-\infty}^{\tau_2} \mathrm{d}\tau_1 E(\tau_n)E(\tau_{n-1})E(\tau_{n-2})...E(\tau_1) \\ &\quad \mathrm{Tr}\left(U_0(t)^{\dagger}\hat{\mu}U_0(t)\left[\hat{\mu}(\tau_n),[\hat{\mu}(\tau_{n-1}),[\hat{\mu}(\tau_{n-2}),...\left[\hat{\mu}(\tau_1),\rho(-\infty)\right]...\right]\right]\right) \end{aligned}$$

By using Equation(3.17) inside the trace we get:

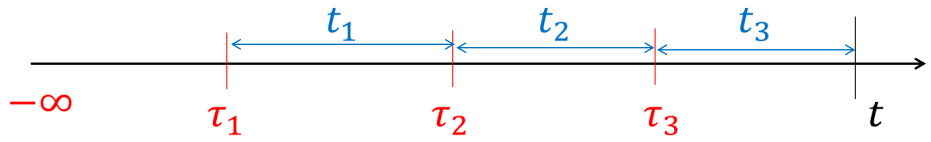

Figure 3.1: This figure depicts the relation between the time points τ_1, τ_2, τ_3 and the time intervals t_1, t_2, t_3

$$P^{(n)}(t) = \left(-\frac{i}{\hbar}\right)^n \int_{-\infty}^{t} \mathrm{d}\tau_n \int_{-\infty}^{\tau_n} \mathrm{d}\tau_{\mathrm{n}-1} \int_{-\infty}^{\tau_{\mathrm{n}-1}} \mathrm{d}\tau_{\mathrm{n}-2} \ldots \int_{-\infty}^{\tau_2} \mathrm{d}\tau_1 E(\tau_n)E(\tau_{n-1})E(\tau_{n-2})\ldots E(\tau_1)$$
$$\mathrm{Tr}\left(\hat{\mu}(t)\left[\hat{\mu}(\tau_n), [\hat{\mu}(\tau_{n-1}), [\hat{\mu}(\tau_{n-2}), \ldots [\hat{\mu}(\tau_1), \rho(-\infty)] \ldots]\right]\right])$$

Hence, to 3$^{\mathrm{rd}}$ order in the fields, the induced polarization is given by:

$$P^{(3)}(t) = \left(-\frac{i}{\hbar}\right)^3 \int_{-\infty}^{t} \mathrm{d}\tau_3 \int_{-\infty}^{\tau_3} \mathrm{d}\tau_2 \int_{-\infty}^{\tau_2} \mathrm{d}\tau_1 E(\tau_3)E(\tau_2)E(\tau_1)$$
$$\mathrm{Tr}\left(\hat{\mu}(t)\left[\hat{\mu}(\tau_3), [\hat{\mu}(\tau_2), [\hat{\mu}(\tau_1), \rho(-\infty)]\right]\right]) \tag{3.24}$$

We will now effect a change of variables of integration[34, 20] from the time points τ_1, τ_2, τ_3 to the time intervals t_1, t_2, t_3 as shown in Figure 3.3. This will allow us to express all the integrals between the same limits and will enhance our physical understanding of the terms for the induced polarization. We can express the time t as a sum over these time intervals:

$$t = t_1 + t_2 + t_3$$

The two sets of variables are related to each other according to the relations given in Table 3.1 .

To convert the integrals, consider the integral $\int_{\tau_1=-\infty}^{\tau_2} \mathrm{d}\tau_1$. By differentiating $t_1 =$

Time Intervals	Time Points
$t_1 = \tau_2 - \tau_1$	$\tau_1 = t - (t_3 + t_2 + t_1)$
$t_2 = \tau_3 - \tau_2$	$\tau_2 = t_1 = t - (t_3 + t_2)$
$t_3 = t - \tau_3$	$\tau_3 = t_1 + t_2 = t - (t_3)$

Table 3.1: Relations between the various time intervals and points.

$\tau_2 - \tau_1$ we get $dt_1 = -d\tau_1$. For the limits, we get that $\tau_1 = -\infty$ maps to $t_1 = \infty$, and $\tau_1 = \tau_2$ maps to $t_1 = 0$. Hence the integral transforms as:

$$\int_{\tau_1=-\infty}^{\tau_2} \mathrm{d}\tau_1 ... \rightarrow -\int_{t_1=\infty}^{0} \mathrm{d}t_1 ... \rightarrow \int_{t_1=0}^{\infty} \mathrm{d}t_1 ...$$

Similarly, the other two integrals transform as $\int_{\tau_2=-\infty}^{\tau_3} \mathrm{d}\tau_2 \rightarrow \int_{t_2=0}^{\infty} \mathrm{d}t_2$ and $\int_{\tau_3=-\infty}^{0} \mathrm{d}\tau_3 \rightarrow \int_{t_3=0}^{\infty} \mathrm{d}t_3$. With these new variables and taking $\tau_1 = 0$, Equation(3.24) can be rewritten as:

$$\begin{aligned} P^{(3)}(t) &= \left(-\frac{i}{\hbar}\right)^3 \int_0^{\infty} \mathrm{d}t_3 \int_0^{\infty} \mathrm{d}t_2 \int_0^{\infty} \mathrm{d}t_1 E\left(t - t_3\right) E\left(t - t_3 - t_2\right) E\left(t - t_3 - t_2 - t_1\right) \\ &\quad \mathrm{Tr}\left(\hat{\mu}(t_3 + t_2 + t_1)\left[\hat{\mu}(t_1 + t_2), \left[\hat{\mu}(t_1), \left[\hat{\mu}(0), \rho(-\infty)\right]\right]\right]\right) \end{aligned}$$

As promised, now we can have a physical understanding of the induced polarization: the 3$^{\mathrm{rd}}$ order induced polarization can be expressed as a convolution of 3 electric fields along with a 3$^{\mathrm{rd}}$order response function.

$$P^{(3)}(t) = \int_0^{\infty} \mathrm{d}t_3 \int_0^{\infty} \mathrm{d}t_2 \int_0^{\infty} \mathrm{d}t_1 E\left(t - t_3\right) E\left(t - t_3 - t_2\right) E\left(t - t_3 - t_2 - t_1\right) S^{(3)}\left(t_3, t_2, t_1\right) \tag{3.25}$$

where the response function is given by:

$$S^{(3)}(t_3, t_2, t_1) = \left(-\frac{i}{\hbar}\right)^3 \mathrm{Tr}\left(\hat{\mu}(t_3 + t_2 + t_1)\left[\hat{\mu}(t_1 + t_2), [\hat{\mu}(t_1), [\hat{\mu}(0), \rho(-\infty)]]\right]\right) \quad (3.26)$$

The physical interpretation of this is that interactions at times 0,t_1,$t_1 + t_2$ leads to an induced polarization at time $t = t_3 + t_2 + t_1$. We will make use of this physical interpretation to draw double sided Feynman diagrams that show some of the perturbation pathways that lead to the third order response.

3.3.1 Perturbation Pathways for the 3rd Order Response

The three nested commutators in Equation(3.26) contribute 2^3 terms. However half of them are complex conjugates of each other, for example the terms $\hat{\mu}(t_1 + t_2)\hat{\mu}(t_1)\hat{\mu}(0)\rho(-\infty)$ and $\rho(-\infty)\hat{\mu}(0)\hat{\mu}(t_1)\hat{\mu}(t_1 + t_2)$. For an experiment done with two optical fields, referred to as pump and probe, the electric field $E(t)$ can be written as:

$$E(t) = E_{pu}(t)\left(e^{-i\omega_{pu}t + ik_{pu}r} + e^{i\omega_{pu}t - ik_{pu}r}\right) + E_{pr}(t)\left(e^{-i\omega_{pr}t + ik_{pr}r} + e^{i\omega_{pr}t - ik_{pr}r}\right)$$

Thus, the convolution of the three electric fields in (3.25) has 4^3 terms, and for Equation(3.25) we get 512 terms. However, by invoking the rotating wave approximation, choosing a time sequence of pulses, and arranging the experimental geometry for phase matching, only a few terms will contribute in an experimental configuration. For example, if the pulses are considered as δ functions, with the pump pulse preceding probe pulse we can write:

$$E(t) = E'_{pu}\delta(t) + E'_{pr}\delta(t - \tau)$$

where we have pulled the frequency and wave-vector information into the coefficients. Now, the product of the three electric fields in Equation(3.25) is given by:

$$\begin{aligned} E\left(t-t_3\right)E\left(t-t_3-t_2\right)E\left(t-t_3-t_2-t_1\right) &= \left(E_{pu}^{'}\delta\left(t-t_3\right)+E_{pr}^{'}\delta\left(t-t_3-\tau\right)\right) \\ &\quad \left(E_{pu}^{'}\delta\left(t-t_3-t_2\right)\right. \\ &\quad \left.+E_{pr}^{'}\delta\left(t-t_3-t_2-\tau\right)\right) \\ &\quad \left(E_{pu}^{'}\delta\left(t-t_3-t_2-t_1\right)\right. \\ &\quad \left.+E_{pr}^{'}\delta\left(t-t_3-t_2-t_1-\tau\right)\right) \end{aligned} \tag{3.27}$$

Now we will show, how the strict time ordering of the pulses will drive some of the terms to zero. For example, if we consider the following term:

$$E_{pu}^{'}\delta\left(t-t_3\right)E_{pr}^{'}\delta\left(t-t_3-t_2-\tau\right)E_{pr}^{'}\delta\left(t-t_3-t_2-t_1-\tau\right)$$

This term has to be zero for a non-zero positive τ. Only terms with strict time ordering, where the pump field acts first and then the probe field acts survive. An example of such a term is:

$$E_{pr}^{'}\delta\left(t-t_3-\tau\right)E_{pu}^{'}\delta\left(t-t_3-t_2\right)E_{pu}^{'}\delta\left(t-t_3-t_2-t_1\right)$$

This discussion demonstrates the power of time resolved nonlinear optical spectroscopy: by controlling the time order of the sequences of pulses hitting the sample we can measure the contribution to the nonlinear signal from distinct perturbation pathways. This goes a long way in elucidating the $\chi^{(3)}$ response of a material.

In a standard differential transmission (dT) geometry, the nonlinear signal is detected along the probe direction. This imposes a phase matching condition due to

which only certain terms in the product (3.27) survive. The direction of the nonlinear signal is given by the sum of the k vectors of the 3 electric fields, expressing the law of conservation of linear momentum. Hence, the terms that contribute are going to be of the form $E_{pr}E^*_{pu}E_{pu}$ where the asterisk refers to the term that goes like $e^{i\omega_{pu}t-ik_{pu}r}$. Hence this term will contribute to a signal in the $k_{pr} - k_{pu} + k_{pu} = k_{pr}$ direction and thus will be detected in a dT experiment. The frequency of the nonlinear signal is also similarly determined by the law of conservation of energy and for the above term will go like ω_{pr}.

The various perturbation pathways that contribute to the nonlinear response can be conveniently represented by double sided Feynman diagrams[6, 34]. The two sides are necessary to represent both the $|\psi\rangle$ and the $\langle\psi|$ of the density matrix, as we have to keep track of whether the interactions due to the time dependent dipole operator happens from the left side or the right side of the density matrix when evaluating the commutator in (3.26). Time increases from bottom to top in these diagrams. Electric fields of form $e^{-i\omega t+ikr}$ are depicted as going from left to right, while the direction is reversed for the complex conjugate term. In general, arrows pointing towards the diagram cause an excitation of the corresponding density matrix element; arrows pointing away from the diagram causes a de-excitation of the same term. More details on the convention of drawing double sided Feynman diagram can be found in [34]. Figure (3.2) shows a diagram that depicts a pathway that leads to a 3^{rd} order response in the probe direction and in which the time ordering of the pump and probe are considered. Note how the incoming (outgoing) interaction causes an excitation (de-excitation) of the corresponding density matrix element. We can take $\rho(-\infty) = |0\rangle\langle 0|$, since initially all population is in the ground state and all the coherences are zero, which means the only nonzero matrix element is ρ_{00}.

Feynman diagrams make it very easy to make what is called the Rotating Wave Approximation (RWA), also known as the resonance approximation, just by inspec-

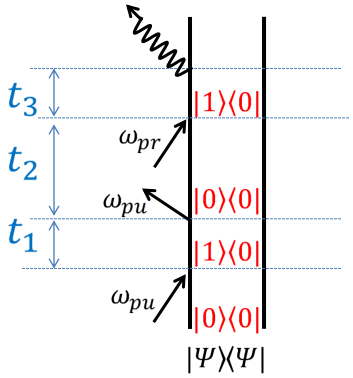

Figure 3.2: Feynman diagram representation of a perturbation term that will result in a signal along the probe direction. The first two interactions are due to the pump pulse with k vectors k_{pu} and $-k_{pu}$ respectively.

tion. The physical justification for the RWA lies in the fact that in a frame rotating at the field frequency, out of the two terms of an electric field $e^{-i\omega t}$ and $e^{i\omega t}$, one of these leads to terms that oscillate at 2ω that have a diminishing contribution once they are integrated over. In a Feynman diagram these two terms of the electric fields are represented by arrows in the opposite sense. Taking the example of Figure(3.2), if the first interaction by the pump was by a away-going arrow, this would cause a de-excitation of the ground state and such pathways are eliminated within the RWA.

3.3.2 Maxwell Bloch Equation

The preceding sections have shown how a nonlinear polarization can be generated in the sample due to the interaction of two optical fields. This finite polarization becomes a source term in Maxwell's equation and leads to the generation of an electric field. Under the slowly varying amplitude approximation and steady state conditions, it can be shown[5], that

$$\frac{\partial E}{\partial z} = \frac{ik}{\epsilon_0} P \tag{3.28}$$

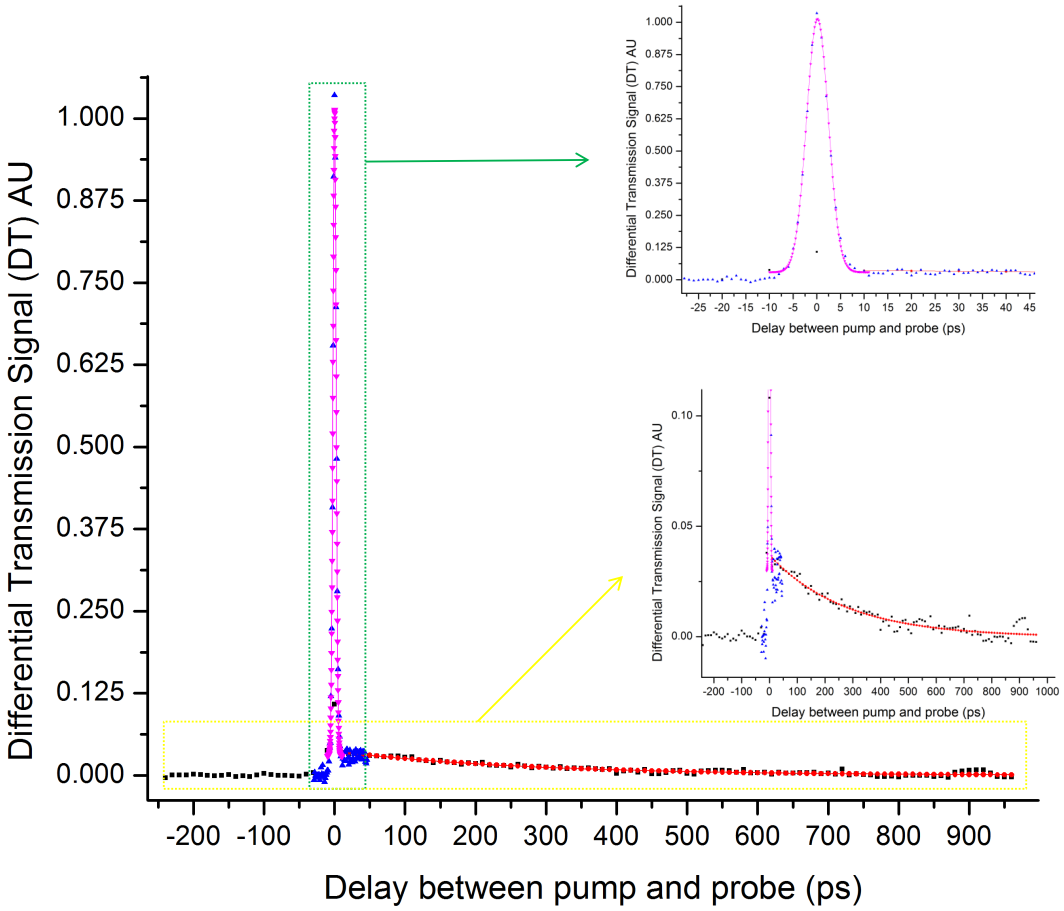

Figure 3.3: Differential Transmission signal on LDS821. The inset on the top right shows the coherent spike at zero delay between the pump and probe pulses. The inset on the bottom right shows the decay signal when the probe pulse is time advanced compared to the pump pulse.

For an optically thin sample, this equation can simply be integrated. Hence, the third order polarization causes a third order electric field of the form:

$$E^{(3)} = \frac{ik}{\epsilon_0} z \chi^{(3)} E_1 E_2 E_3 \tag{3.29}$$

This is the physical justification of the term in Equation(3.3).

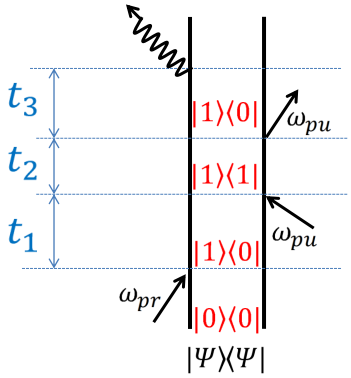

Figure 3.4: Feynman diagram representation of a perturbation pathway that leads to the coherent spike. The time ordering of the pump and probe is not followed since the coherent spike occurs at zero delay.

3.4 Experimental Data on Test Sample: LDS821

In this section we will show some differential transmission data on a test sample of LDS821, which is a common laser dye. We will defer the description of the experimental details to a later chapter. Figure(3.3) shows a typical dT data-set obtained from LDS821. There is a spike in the dT signal at zero pump-probe delay which is often referred to as the coherent artifact. In addition to this spike, we see an exponential decay as the probe is delayed with respect to the pump. The coherent spike signal is observed when the pump and probe are overlapped in time and contain contributions from Feynman diagrams in which the time ordering of the pump and probe is not followed. Due to strict time ordering, these diagrams do not contribute to the dT signal when the probe is delayed by some amount with respect to the pump. Hence different perturbation pathways lead to the dT signal observed for zero delay, and positive delay.

One of the perturbation pathways that leads to the coherent spike is shown in Figure(3.4). The first interaction with the probe leads to a nonzero coherence ρ_{10}. The second interaction with the pump pulse results in excited state population ρ_{11}.

The third interaction with the pump pulse causes the population to stimulate down, and results in coherence ρ_{10}. Now this non-zero coherence leads to a macroscopic polarization, which results in an electric field along the phase-matched direction of the probe.

3.5 Chapter Summary

The optical spectroscopy technique of differential transmission was discussed, and it was shown that dT measures the third order optical response of the system homodyne detected with the probe. It was also seen that in the $\chi^{(3)}$ limit, the dT signal would scale linearly with the pump and probe powers. A semi-classical description of light-matter interaction was introduced, and an equation of motion of the density matrix was developed. Solutions to the third order in the optical fields were obtained for this equation of motion, and it was shown that the third order polarization can be written as a convolution of three electric fields along with a third order response function. Some of the perturbation pathways that lead to the third order response were discussed, and double sided Feynman diagrams were introduced to visualize them. Lastly, some experimental data on a test sample was presented to show how the various perturbation pathways could show up in a simple experiment.

CHAPTER IV

Signature of Excitation Induced Resonant Energy Shifts in Third Order Nonlinear Signals

In Chapter(II) it was shown that a microscopic model predicts a configurational change in the diameter of a SWCNT upon optical excitation. The easiest way to measure energy shifts arising from such configurational changes would be through simple spectroscopy measurements, for example, by determining energy shifts in absorption from the ground state, and photoluminescence(PL) from the excited state. However for small changes in the resonant energy, compared to the linewidth of the transition, this would be a difficult effect to measure in a time-integrated PL measurement, especially if the changes in the resonant energy are associated with short-timescale dynamics. In this chapter we will aim to show how time-resolved nonlinear optical spectroscopy serves as a powerful tool to detect such small excitation induced changes in the resonant energy levels. The signature of such effects on the time-resolved, homodyne detected third order (in the applied fields) nonlinear optical response of a sample is derived.

We will start with the simplest case of a single 2-level system interacting with a nearly resonant optical field. Following the prescription of perturbatively calculating the nonlinear response that was introduced in Chapter(III), we will calculate what form the measured dT signal should be for this simple system. Then we will

consider two independent 2-level systems in a product Hilbert space. This does not add any new physics to the problem, but serves to illustrate all possible perturbation sequences which sum up to the expected result. Next, a small interaction is turned on between the two 2-level systems such that excitation of one of the systems causes a configurational change over a certain timescale, that modifies the transition energy for the second excitation. From the functional form of the expression for the dT signal for this problem, a data analysis method is constructed that allows to search for signature signs of an excitation induced change in the resonant energy.

4.1 Time Domain Perturbation Calculation of a 2- Level System

Here we will obtain perturbative results to the third order in the fields for a 2-level system. We will consider a pump probe geometry, in which we will consider only the terms that will lead to phase matched signals in the probe direction, at the probe frequency. These are the only terms that will contribute in a differential transmission (dT) experiment, in which the nonlinear signal is homodyne detected with the probe as was shown in Chapter(III). We will also consider a strict time ordering between the pump and probe pulses, so that the first two interactions are with the pump, and the third one is with the probe. We will invoke what is known as the rate approximation, in which it shall be obtained that the coherences adiabatically follow the population difference. We will also consider pulses to be delta functions in time just to simplify the maths.

Consider a 2-level system, with the states $|0\rangle$ and $|1\rangle$. The energy of the ground state can be chosen to be zero, and the unperturbed Hamiltonian can be written as:

$$H_0 = \begin{pmatrix} 0 & 0 \\ 0 & \hbar\omega_0 \end{pmatrix}$$

The time evolution operator is given by:

$$U_0 = \begin{pmatrix} 1 & 0 \\ 0 & e^{-i\hbar\omega_0 t} \end{pmatrix}$$

The interaction of this two level system with a pump and probe field adds another term to the Hamiltonian given by:

$$V = \hbar \begin{pmatrix} 0 & \chi \\ \chi & 0 \end{pmatrix}$$

where $\chi = \left(\chi_{pu} e^{-i\omega_{pu}t + ik_{pu}r} + \text{cc}\right) + \left(\chi_{pr} e^{-i\omega_{pr}t + ik_{pr}r} + \text{cc}\right)$. Here χ_{pu} is one half the Rabi frequency and is defined as[5]:

$$\chi_{pu} = -\frac{\mu_{10} E_{pu}}{2\hbar} \tag{4.1}$$

where μ_{10} is the transition dipole moment. We go into an interaction representation with following interaction Hamiltonian

$$V^I(t) = U_0^\dagger(t) V(t) U_0(t)$$

Neglecting the terms in $V^I(t)$,that oscillate at 2ω(RWA) and putting detuning $\delta_{pu,pr} = \omega_0 - \omega_{pu,pr}$ we get

$$V^I = \hbar \begin{pmatrix} 0 & \chi^*_{pu} e^{-i\delta_{pu}t - ik_{pu}r} + \chi^*_{pr} e^{-i\delta_{pr}t - ik_{pr}r} \\ \chi_{pu} e^{i\delta_{pu}t + ik_{pu}r} + \chi_{pr} e^{i\delta_{pr}t + ik_{pr}r} & 0 \end{pmatrix}$$

The equation of motion of the density matrix in the interaction representation is given by:

$$\frac{d\rho^I(t)}{dt} = -\frac{i}{\hbar}\left[\hat{V}^I(t), \rho^I(t)\right] - \left.\frac{d\rho^I(t)}{dt}\right|_{\text{relaxation}}$$

By expanding out the commutator, and writing the decay terms, the following equations of motion are obtained:

$$\begin{aligned}
\dot{\rho}^I_{01} &= -i\left(\chi^*_{pu} e^{-i\delta_{pu}t - ik_{pu}r} + \chi^*_{pr} e^{-i\delta_{pr}t - ik_{pr}r}\right)(\rho_{11} - \rho_{00}) - \gamma\rho^I_{01} \\
\dot{\rho}^I_{10} &= i\left(\chi_{pu} e^{i\delta_{pu}t + ik_{pu}r} + \chi_{pr} e^{i\delta_{pr}t + ik_{pr}r}\right)(\rho_{11} - \rho_{00}) - \gamma\rho^I_{10} \\
\dot{\rho}_{11} &= i\left(\chi^*_{pu} e^{-i\delta_{pu}t - ik_{pu}r} + \chi^*_{pr} e^{-i\delta_{pr}t - ik_{pr}r}\right)\rho^I_{10} \\
&- i\left(\chi_{pu} e^{i\delta_{pu}t + ik_{pu}r} + \chi_{pr} e^{i\delta_{pr}t + ik_{pr}r}\right)\rho^I_{01} - \gamma_2\rho_{11} \\
\dot{\rho}_{00} &= -i\left(\chi^*_{pu} e^{-i\delta_{pu}t - ik_{pu}r} + \chi^*_{pr} e^{-i\delta_{pr}t - ik_{pr}r}\right)\rho^I_{10} \\
&+ i\left(\chi_{pu} e^{i\delta_{pu}t + ik_{pu}r} + \chi_{pr} e^{i\delta_{pr}t + ik_{pr}r}\right)\rho^I_{01} + \gamma_2\rho_{11}
\end{aligned}$$

4.1.1 Perturbation Solution

We will solve these equations perturbatively in the applied fields to third order. We will enforce time ordering in the sequence that is calculated below, with the first two interactions due to the pump, and the third due to the probe. The terms in this calculation can be visualized by the Feynman diagrams shown in Figure 4.1

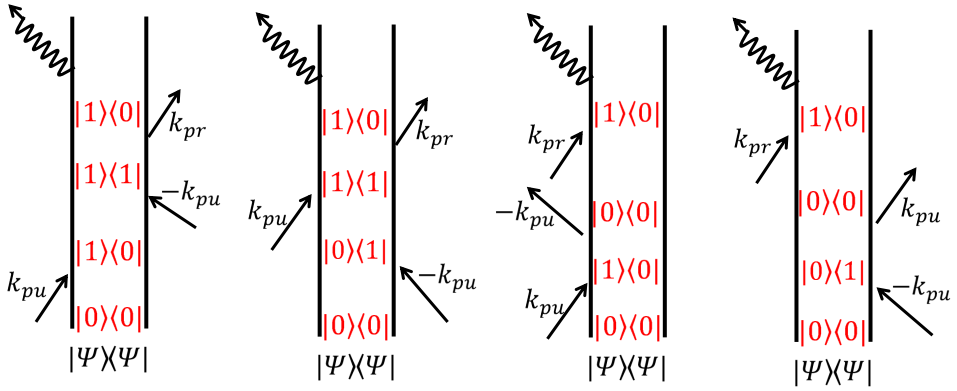

Figure 4.1: Double sided Feynman diagrams representing the terms contributing to the third order signal for a 2-level system.

4.1.1.1 First Order

$$\dot{\rho}_{10}^{I(1)} = i\chi_{pu} e^{i\delta_{pu}t + ik_{pu}r} \left(\rho_{11}^{(0)} - \rho_{00}^{(0)}\right) - \gamma\rho_{10}^{I(1)}$$

We can assume the solution to this differential equation to be of the form:

$$\rho_{10}^{I(1)} = \rho_{10} e^{i\delta_{pu}t} \tag{4.2}$$

$$\dot{\rho}_{10} e^{i\delta_{pu}t} + i\delta_{pu}\rho_{10} e^{i\delta_{pu}t} = i\chi_{pu} e^{i\delta_{pu}t + ik_{pu}r} \left(\rho_{11}^{(0)} - \rho_{00}^{(0)}\right) - \gamma\rho_{10} e^{i\delta_{pu}t}$$

Canceling the exponential factors, and rearranging we get

$$\dot{\rho}_{10} + (\gamma + i\delta_{pu})\,\rho_{10} = i\chi_{pu} e^{ik_{pu}r} \left(\rho_{11}^{(0)} - \rho_{00}^{(0)}\right) \tag{4.3}$$

Rate Equation Approximation We will now show explicit time dependence by writing $\rho_{10}(t)$. By using the integrating factor $e^{(\gamma + i\delta_{pu})t}$ we get

$$\rho_{10}(t)e^{(\gamma+i\delta_{pu})t} - \rho_{10}(0) = i\int_0^t \chi_{pu}e^{ik_{pu}r}\left(\rho_{11}^{(0)} - \rho_{00}^{(0)}\right)e^{(\gamma+i\delta_{pu})t'}\mathrm{d}t'$$

$$\implies \rho_{10}(t) = \rho_{10}(0)e^{-(\gamma+i\delta_{pu})t} + i\int_0^t \chi_{pu}e^{ik_{pu}r}\left(\rho_{11}^{(0)} - \rho_{00}^{(0)}\right)e^{-(\gamma+i\delta_{pu})(t-t')}\mathrm{d}t' \quad (4.4)$$

Integrating $\int_0^t \chi_{pu}e^{ik_{pu}r}\left(\rho_{11}^{(0)} - \rho_{00}^{(0)}\right)e^{-(\gamma+i\delta_{pu})(t-t')}\mathrm{d}t'$ by parts we get:

$$\left[\frac{\chi_{pu}e^{ik_{pu}r}\left(\rho_{11}^{(0)} - \rho_{00}^{(0)}\right)e^{-(\gamma+i\delta_{pu})(t-t')}}{(\gamma+i\delta_{pu})}\right]_{t'=0}^{t} - \int_0^t \frac{d}{dt}\left\{\chi_{pu}e^{ik_{pu}r}\left(\rho_{11}^{(0)} - \rho_{00}^{(0)}\right)\right\}\frac{e^{-(\gamma+i\delta_{pu})(t-t')}}{(\gamma+i\delta_{pu})}\mathrm{d}t'$$

Putting explicit time dependence in the population terms and the fields, we get

$$\int_0^t \chi_{pu}e^{ik_{pu}r}\left(\rho_{11}^{(0)} - \rho_{00}^{(0)}\right)e^{-(\gamma+i\delta_{pu})(t-t')}\mathrm{d}t' = \frac{\chi_{pu}(t)e^{ik_{pu}r}}{(\gamma+i\delta_{pu})}\left(\rho_{11}^{(0)}(t) - \rho_{00}^{(0)}(t)\right) - \frac{\chi_{pu}(0)e^{ik_{pu}r}}{(\gamma+i\delta_{pu})}\left(\rho_{11}^{(0)}(0) - \rho_{00}^{(0)}(0)\right)e^{-(\gamma+i\delta_{pu})t} - \int_0^t \frac{d}{dt}\left\{\chi_{pu}e^{ik_{pu}r}\left(\rho_{11}^{(0)} - \rho_{00}^{(0)}\right)\right\}\frac{e^{-(\gamma+i\delta_{pu})(t-t')}}{(\gamma+i\delta_{pu})}\mathrm{d}t' \quad (4.5)$$

Now, in the limit that the Rabi frequency is much smaller that the linewidth (more formally, $\chi(t)(\rho_{22}(t) - \rho_{00}(t))$ is slowly varying on the timescale of $\frac{1}{\gamma - i\delta}$), the second and third terms in the RHS of Equation (4.5) quickly and exponentially go to zero[5], and we have:

$$\int_0^t \chi_{pu} e^{ik_{pu}r} \left(\rho_{11}^{(0)} - \rho_{00}^{(0)}\right) e^{-(\gamma+i\delta_{pu})(t-t')} \mathrm{d}t' \approx \frac{\chi_{pu}(t) e^{ik_{pu}r}}{(\gamma + i\delta_{pu})} \left(\rho_{11}^{(0)}(t) - \rho_{00}^{(0)}(t)\right)$$

So going back to Equation (4.4) we have:

$$\rho_{10}(t) \approx \rho_{10}(0) e^{-(\gamma+i\delta_{pu})t} + \frac{i\chi_{pu}(t) e^{ik_{pu}r}}{(\gamma + i\delta_{pu})} \left(\rho_{11}^{(0)}(t) - \rho_{00}^{(0)}(t)\right)$$

The first term above also exponentially decays to zero. Now we get

$$\rho_{10} \approx \frac{i\chi_{pu}}{\gamma + i\delta_{pu}} e^{ik_{pu}r} \left(\rho_{11}^{(0)} - \rho_{00}^{(0)}\right), \tag{4.6}$$

where to simplify notation, the explicit time dependence is not written anymore. The key thing to note here is that in the rate equation approximation, the coherence is given by the product of the Rabi frequency and the population difference. Note that this is the same expression we would have got by putting $\dot{\rho}_{10} = 0$ in Equation(4.3). Putting $\rho_{00}^{(0)} = 1$ in Equation(4.6) and substituting in Equation(4.2) we get

$$\rho_{10}^{I(1)} = \frac{-i\chi_{pu}}{\gamma + i\delta_{pu}} e^{i\delta_{pu}t + ik_{pu}r}$$

We also get the complex conjugate:

$$\rho_{01}^{I(1)} = \frac{i\chi_{pu}^*}{\gamma - i\delta_{pu}} e^{-i\delta_{pu}t - ik_{pu}r}$$

4.1.1.2 Second Order

$$\begin{aligned}
\dot{\rho}_{11}^{(2)} &= i\chi_{pu}^{*} e^{-i\delta_{pu}t - ik_{pu}r}\rho_{10}^{I(1)} - i\chi_{pu} e^{i\delta_{pu}t + ik_{pu}r}\rho_{01}^{I(1)} - \gamma_2\rho_{11}^{(2)} \\
&= i\chi_{pu}^{*} e^{-i\delta_{pu}t - ik_{pu}r}\left(\frac{-i\chi_{pu}}{\gamma + i\delta_{pu}} e^{i\delta_{pu}t + ik_{pu}r}\right) \\
&- i\chi_{pu} e^{i\delta_{pu}t + ik_{pu}r}\left(\frac{i\chi_{pu}^{*}}{\gamma - i\delta_{pu}} e^{-i\delta_{pu}t - ik_{pu}r}\right) - \gamma_2\rho_{11}^{(2)}
\end{aligned}$$

Rearranging the terms we get:

$$\begin{aligned}
\dot{\rho}_{11}^{(2)} + \gamma_2\rho_{11}^{(2)} &= |\chi_{pu}|^2\left(\frac{1}{(\gamma + i\delta_{pu})} + \frac{1}{(\gamma - i\delta_{pu})}\right) \\
&= \frac{2\gamma\,|\chi_{pu}|^2}{\gamma^2 + \delta_{pu}^2}
\end{aligned}$$

Using the integrating factor $e^{\gamma_2 t}$, we get

$$\dot{\rho}_{11}^{(2)}(t) = \frac{2\gamma}{\gamma^2 + \delta_{pu}^2}\int_0^t \mathrm{d}t'\ |\chi_{pu}|^2\, e^{-\gamma_2(t-t')}$$

For delta pulses, we have $|\chi_{pu}|^2 = |\chi_{pu,0}|^2\,\delta(t)$. Here $|\chi_{pu,0}|^2$ has units of 1/[time]. So we get

$$\rho_{11}^{(2)} = \frac{2\gamma\,|\chi_{pu}|^2}{\gamma^2 + \delta_{pu}^2} e^{-\gamma_2 t}$$

From population conservation we also get

$$\rho_{00}^{(2)} = -\frac{2\gamma\,|\chi_{pu}|^2}{\gamma^2 + \delta_{pu}^2} e^{-\gamma_2 t}$$

To make the notation simpler, the subscript 0 has been dropped from $|\chi_{pu,0}|^2$. Hence, it is obtained that for fixed pump power and detuning, the second order change in

the populations can be written as the product of a dimensionless constant and an exponential decay.

4.1.1.3 Third Order

$$\dot{\rho}_{10}^{I(3)} = i\chi_{pr}e^{i\delta_{pr}t+ik_{pr}r}\left(\rho_{11}^{(2)} - \rho_{00}^{(2)}\right) - \gamma\rho_{10}^{I(3)}$$

Take $\rho_{10}^{I(3)} = \rho_{10}e^{i\delta_{pr}t}$. We get

$$\dot{\rho}_{10}e^{i\delta_{pr}t} + i\delta_{pr}\rho_{10}e^{i\delta_{pr}t} = i\chi_{pr}e^{i\delta_{pr}t+ik_{pr}r}\left(\rho_{11}^{(2)} - \rho_{00}^{(2)}\right) - \gamma\rho_{10}e^{i\delta_{pr}t}$$

In the rate equation limit, as before we get:

$$\rho_{10} = \frac{i\chi_{pr}e^{ik_{pr}r}}{\gamma + i\delta_{pr}}\left(\rho_{11}^{(2)} - \rho_{00}^{(2)}\right)$$

So we get:

$$\rho_{10}^{I(3)} = \frac{i\chi_{pr}}{\gamma + i\delta_{pr}}\frac{2\gamma\left|\chi_{pu}\right|^2}{\gamma^2 + \delta_{pu}^2}2e^{-\gamma_2 t}e^{i\delta_{pr}t+ik_{pr}r} \tag{4.7}$$

4.1.2 Nonlinear Signal

To calculate the expectation value of the dipole operator, the density matrix terms need to be to be converted from the interaction representation back to the Schrödinger picture

$$\rho = U_0\rho^I U_0^\dagger$$

In terms of matrix elements we get

$$\rho_{nm}^{(3)} = \rho_{nm}^{I(3)}e^{-i(E_n - E_m)t} \tag{4.8}$$

It is easy to see that in the expression of the coherences calculated to the third order in Equation(4.7), the term $e^{i\delta_{pr}t}$ will be replaced by $e^{-i\omega_{pr}t}$ in going from the interaction to the Schrödinger picture. The nonlinear polarization is given by:

$$\begin{aligned} P^{(3)} &= \mathrm{Tr}\left(\mu\rho^{(3)}\right) \\ &= \mu_{01}\rho_{10}^{(3)} + \mathrm{c.c} \end{aligned}$$

Making use of Equation(4.7) we get

$$P^{(3)} = \frac{i\mu_{01}\chi_{pr}}{\gamma + i\delta_{pr}} \frac{2\gamma\left|\chi_{pu}\right|^2}{\gamma^2 + \delta_{pu}^2} 2e^{-\gamma_2 t} e^{-i\omega_{pr}t + ik_{pr}r} \tag{4.9}$$

This nonlinear polarization acts as a source term in Maxwell's equation and generates an electric field given by Equation(3.28)

$$E^{(3)} = \frac{ikl}{\epsilon_0} \frac{i\mu_{01}\chi_{pr}}{\gamma + i\delta_{pr}} \frac{2\gamma\left|\chi_{pu}\right|^2}{\gamma^2 + \delta_{pu}^2} 2e^{-\gamma_2 t} e^{-i\omega_{pr}t + ik_{pr}r}$$

By using Equation(4.1), we get:

$$E^{(3)} = \frac{kl}{2\hbar\epsilon_0} \frac{\mu_{01}^2 E_{pr}}{\gamma + i\delta_{pr}} \frac{2\gamma\left|\chi_{pu}\right|^2}{\gamma^2 + \delta_{pu}^2} 2e^{-\gamma_2 t} e^{-i\omega_{pr}t + ik_{pr}r}$$

This signal is homodyne detected with the probe field to give the dT signal. Using Equation (3.5)

$$\begin{aligned} \mathrm{dT} &= 2\mathrm{Re}\left(E_{pr}^* E^{(3)}\right) \\ &= \frac{2kl\mu_{01}^2}{2\hbar\epsilon_0} \frac{2\gamma\left|E_{pr}\right|^2}{\gamma^2 + \delta_{pr}^2} \frac{2\gamma\left|\chi_{pu}\right|^2}{\gamma^2 + \delta_{pu}^2} 2e^{-\gamma_2 t} \end{aligned}$$

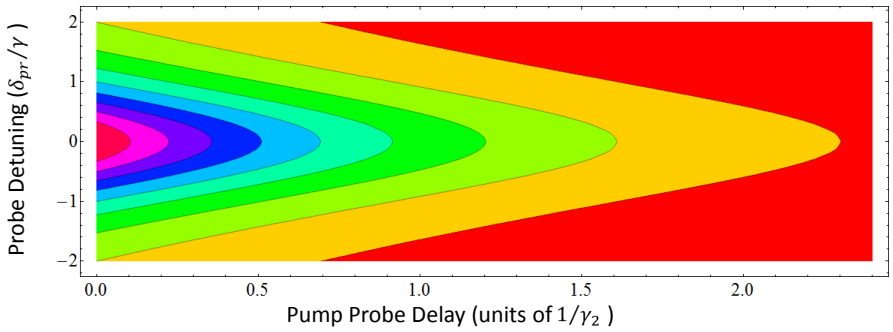

Figure 4.2: Simulated dT signal for a 2 level system.

Making use of Equation(4.1) again, we get:

$$\mathrm{dT} = \frac{4kl\hbar}{\epsilon_0}\frac{2\gamma\left|\chi_{pr}\right|^2}{\gamma^2+\delta_{pr}^2}\frac{2\gamma\left|\chi_{pu}\right|^2}{\gamma^2+\delta_{pu}^2}2e^{-\gamma_2 t} \tag{4.10}$$

Key points to note in dT signal

1. The dT signal scales linearly with both the pump and probe power. This proves to be a useful way to check if experimental data should be modeled by a $\chi^{(3)}$ process or not. For the data obtained in this thesis, it was verified that the signal scaled linearly with the pump and probe powers as shown in Chapter(V).

2. The main experimental technique discussed in this thesis involve two color dT measurements: The pump wavelength is fixed at a value, and the probe wavelength is scanned. For each probe wavelength used, the delay between the pump and probe is adjusted to get delay scans. Hence, datasets are obtained where the dT signal is mapped out as a function of probe wavelength, and the delay between the pump and probe.

3. From the functional form of Equation(4.10), such two color datasets can be simulated and one such simulation is shown in Figure(4.2). Thus, the time slices in this plot will be single exponential decays, and the wavelength slices

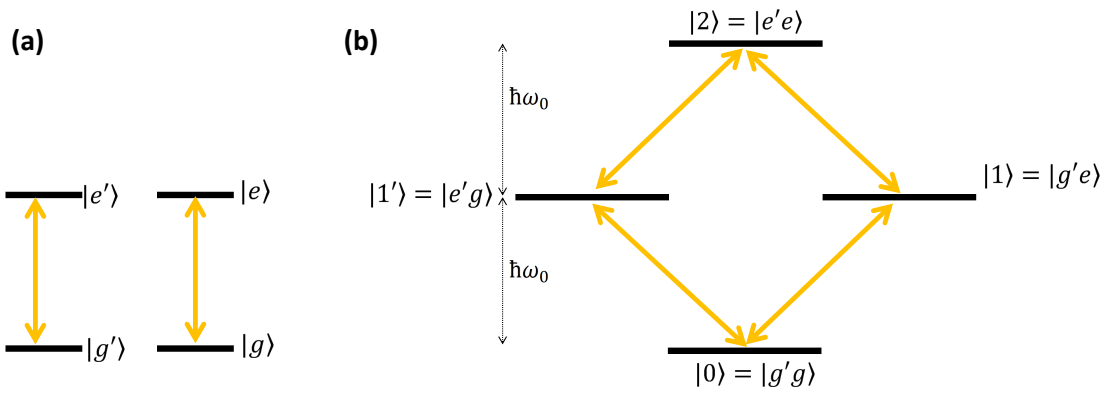

Figure 4.3: (a) Two independent 2 level systems. (b) The two systems depicted in a product space.

will be single lorentzian lineshapes.

4.2 Perturbation Calculation of Two Independent 2-Level systems

The focus of this section will be to demonstrate how the $\chi^{(3)}$ response can be sensitive to two excitations in a system. This follows simply from energy conservation considerations: two interactions with the pump pulse results in creating population in one of the excitations, with the third interaction with the probe pulse probing all possible transitions, including the possibility of exciting another excitation. This will lead to multiple perturbation sequences contributing to the nonlinear signal, with the total signal being summed over. We will demonstrate this for two independent 2-level systems as shown in Figure(4.3a). Physically, it is expected that the dT signal for this system should just be twice that of the single 2-level system which is given by Equation (4.10). This will be proved mathematically by considering the system in the product Hilbert space of the two 2-level systems. This product Hilbert space is shown in Figure(4.3b).

In this product space, the unperturbed Hamiltonian can be written as

$$H_0 = \text{Diag}\,(0, E_1, E_1, 2E_1)$$

and the time evolution operator as

$$U_0 = \text{Diag}\left(1, e^{-iE_1 t}, e^{-iE_1 t}, e^{-i2E_1 t}\right)$$

The light-matter interaction will add a term to the unperturbed Hamiltonian that is given by

$$V = \begin{pmatrix} 0 & \chi & \chi & 0 \\ \chi & 0 & 0 & \chi \\ \chi & 0 & 0 & \chi \\ 0 & \chi & \chi & 0 \end{pmatrix}$$

Here χ is the sum of the pump and probe fields. Switching to the interaction representation, we get the equations of motion:

$$\begin{aligned}
\dot{\rho}^I_{01} &= -i\left(\chi^*_{pu} e^{-i\delta_{pu}t - ik_{pu}r} + \chi^*_{pr} e^{-i\delta_{pr}t - ik_{pr}r}\right)(\rho_{11} - \rho_{00}) - \gamma\rho^I_{01} \\
\dot{\rho}^I_{10} &= i\left(\chi_{pu} e^{i\delta_{pu}t + ik_{pu}r} + \chi_{pr} e^{i\delta_{pr}t + ik_{pr}r}\right)(\rho_{11} - \rho_{00}) - \gamma\rho^I_{10} \\
\dot{\rho}^I_{01'} &= -i\left(\chi^*_{pu} e^{-i\delta_{pu}t - ik_{pu}r} + \chi^*_{pr} e^{-i\delta_{pr}t - ik_{pr}r}\right)(\rho_{1'1'} - \rho_{00}) - \gamma\rho^I_{01'} \\
\dot{\rho}^I_{1'0} &= i\left(\chi_{pu} e^{i\delta_{pu}t + ik_{pu}r} + \chi_{pr} e^{i\delta_{pr}t + ik_{pr}r}\right)(\rho_{1'1'} - \rho_{00}) - \gamma\rho^I_{1'0} \\
\dot{\rho}^I_{12} &= -i\left(\chi^*_{pu} e^{-i\delta_{pu}t - ik_{pu}r} + \chi^*_{pr} e^{-i\delta_{pr}t - ik_{pr}r}\right)(\rho_{22} - \rho_{11}) - \gamma\rho^I_{12} \\
\dot{\rho}^I_{21} &= i\left(\chi_{pu} e^{i\delta_{pu}t + ik_{pu}r} + \chi_{pr} e^{i\delta_{pr}t + ik_{pr}r}\right)(\rho_{22} - \rho_{11}) - \gamma\rho^I_{21}
\end{aligned}$$

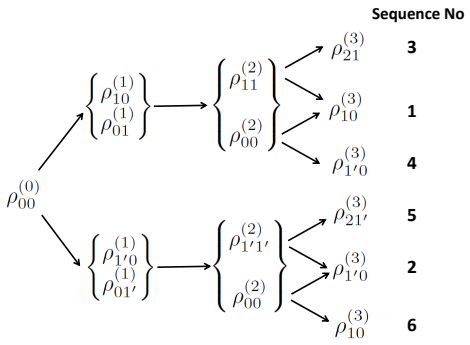

Figure 4.4: Perturbation sequences leading to the $\chi^{(3)}$ signal for two independent 2-level systems.

$$
\begin{aligned}
\dot{\rho}^I_{1'2} &= -i\left(\chi^*_{pu}e^{-i\delta_{pu}t-ik_{pu}r}+\chi^*_{pr}e^{-i\delta_{pr}t-ik_{pr}r}\right)(\rho_{22}-\rho_{1'1'})-\gamma\rho^I_{1'2}\\
\dot{\rho}^I_{21'} &= i\left(\chi_{pu}e^{i\delta_{pu}t+ik_{pu}r}+\chi_{pr}e^{i\delta_{pr}t+ik_{pr}r}\right)(\rho_{22}-\rho_{1'1'})-\gamma\rho^I_{21'}\\
\dot{\rho}_{00} &= -i\left(\chi^*_{pu}e^{-i\delta_{pu}t-ik_{pu}r}+\chi^*_{pr}e^{-i\delta_{pr}t-ik_{pr}r}\right)\left(\rho^I_{10}+\rho^I_{1'0}\right)\\
&\quad +i\left(\chi_{pu}e^{i\delta_{pu}t+ik_{pu}r}+\chi^*_{pr}e^{i\delta_{pr}t+ik_{pr}r}\right)\left(\rho^I_{01}+\rho^I_{01'}\right)\\
&\quad +\gamma_2\left(\rho_{11}+\rho_{1'1'}\right)\\
\dot{\rho}_{11} &= i\left(\chi^*_{pu}e^{-i\delta_{pu}t-ik_{pu}r}+\chi^*_{pr}e^{-i\delta_{pr}t-ik_{pr}r}\right)\left(\rho^I_{10}-\rho^I_{21}\right)\\
&\quad -i\left(\chi_{pu}e^{i\delta_{pu}t+ik_{pu}r}+\chi_{pr}e^{i\delta_{pr}t+ik_{pr}r}\right)\left(\rho^I_{01}-\rho^{(I)}_{12}\right)\\
&\quad +\gamma_2\left(\rho_{22}-\rho_{11}\right)\\
\dot{\rho}_{1'1'} &= i\left(\chi^*_{pu}e^{-i\delta_{pu}t-ik_{pu}r}+\chi^*_{pr}e^{-i\delta_{pr}t-ik_{pr}r}\right)\left(\rho^I_{1'0}-\rho^I_{21'}\right)\\
&\quad -i\left(\chi_{pu}e^{i\delta_{pu}t+ik_{pu}r}+\chi_{pr}e^{i\delta_{pr}t+ik_{pr}r}\right)\left(\rho^I_{01'}-\rho^I_{1'2}\right)\\
&\quad +\gamma_2\left(\rho_{22}-\rho_{1'1'}\right)\\
\dot{\rho}_{22} &= i\left(\chi^*_{pu}e^{-i\delta_{pu}t-ik_{pu}r}+\chi^*_{pr}e^{-i\delta_{pr}t-ik_{pr}r}\right)\left(\rho^I_{21}+\rho^I_{21'}\right)\\
&\quad -i\left(\chi_{pu}e^{i\delta_{pu}t+ik_{pu}r}+\chi_{pr}e^{i\delta_{pr}t+ik_{pr}r}\right)\left(\rho^I_{12}+\rho^I_{1'2}\right)\\
&\quad -2\gamma_2\rho_{22}
\end{aligned}
$$

The six perturbation sequences that contribute are shown in Figure(4.4).

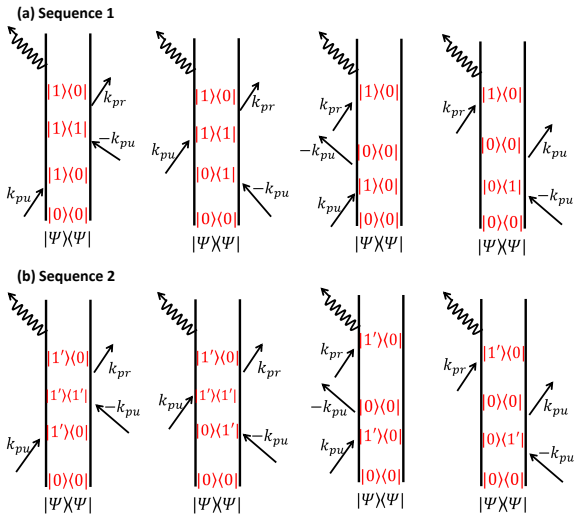

Figure 4.5: Terms that contribute to (a)Sequence 1. (b)Sequence 2.

Sequence 1

The terms in the first sequence can be visualized by the double sided Feynman diagrams in Figure(4.5). We get the same result as in the case of a single 2-level system given by Equation(4.7)

$$\rho_{10}^{I(3)} = \frac{i\chi_{pr}}{\gamma + i\delta_{pr}} \frac{2\gamma \left|\chi_{pu}\right|^2}{\gamma^2 + \delta_{pu}^2} 2e^{-\gamma_2 t} e^{i\delta_{pr} t + ik_{pr} r} \tag{4.11}$$

Sequence 2

Again, we get the same result as in the case of a single two level system.

$$\rho_{1'0}^{I(3)} = \frac{i\chi_{pr}}{\gamma + i\delta_{pr}} \frac{2\gamma \left|\chi_{pu}\right|^2}{\gamma^2 + \delta_{pu}^2} 2e^{-\gamma_2 t} e^{i\delta_{pr} t + ik_{pr} r} \tag{4.12}$$

Sequence 3

The terms in the third sequence can be visualized by the Feynman diagrams in Figure(4.6a). To the second order in the pump fields, we get the non zero population terms as:

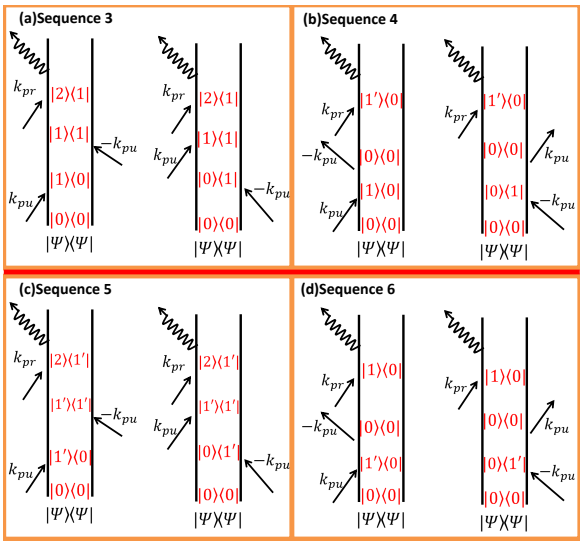

Figure 4.6: Terms that contribute to (a)Sequence 3. (b) Sequence 4. (c)Sequence 5. (b) Sequence 6. The nonlinear signal that arises out of Sequences 3 and 5, cancels with the what is obtained from Sequences 4 and 6.

$$\rho_{11}^{(2)} = \frac{2\gamma \left|\chi_{pu}\right|^2}{\gamma^2 + \delta_{pu}^2} e^{-\gamma_2 t}$$

$$\rho_{00}^{(2)} = -\frac{2\gamma \left|\chi_{pu}\right|^2}{\gamma^2 + \delta_{pu}^2} e^{-\gamma_2 t}$$

To the third order we get:

$$\dot{\rho}_{21}^{I(3)} = i\chi_{pr} e^{i\delta_{pr} t + ik_{pr} r} \left(\rho_{22}^{(2)} - \rho_{11}^{(2)}\right) - \gamma \rho_{21}^{I(3)}$$

Here $\rho_{22}^{(2)} = 0$. In the rate approximation limit, we get

$$\rho_{21}^{I(3)} = -\frac{i\chi_{pr}}{\gamma + i\delta_{pr}} \frac{2\gamma \left|\chi_{pu}\right|^2}{\gamma^2 + \delta_{pu}^2} e^{-\gamma_2 t} e^{i\delta_{pr} t + ik_{pr} r} \tag{4.13}$$

Sequence 4

Again, to the second order in the pump fields, we get the non-zero population terms as:

$$\rho_{11}^{(2)} = \frac{2\gamma \left|\chi_{pu}\right|^2}{\gamma^2 + \delta_{pu}^2} e^{-\gamma_2 t}$$

$$\rho_{00}^{(2)} = -\frac{2\gamma \left|\chi_{pu}\right|^2}{\gamma^2 + \delta_{pu}^2} e^{-\gamma_2 t}$$

To the third order we get:

$$\dot{\rho}_{1'0}^{I(3)} = i\chi_{pr} e^{i\delta_{pr}t + ik_{pr}r} \left(\rho_{1'1'}^{(2)} - \rho_{00}^{(2)}\right) - \gamma \rho_{1'0}^{I(3)}$$

Here $\rho_{1'1'}^{(2)} = 0$. In the rate approximation limit, we get

$$\rho_{1'0}^{I(3)} = \frac{i\chi_{pr}}{\gamma + i\delta_{pr}} \frac{2\gamma \left|\chi_{pu}\right|^2}{\gamma^2 + \delta_{pu}^2} e^{-\gamma_2 t} e^{i\delta_{pr}t + ik_{pr}r} \tag{4.14}$$

Sequence 5

The terms contributing in this sequence are visualized by the diagrams in Figure(4.6a). To the second order in the pump fields, we get the non-zero population terms as:

$$\rho_{1'1'}^{(2)} = \frac{2\gamma \left|\chi_{pu}\right|^2}{\gamma^2 + \delta_{pu}^2} e^{-\gamma_2 t}$$

$$\rho_{00}^{(2)} = -\frac{2\gamma \left|\chi_{pu}\right|^2}{\gamma^2 + \delta_{pu}^2} e^{-\gamma_2 t}$$

To the third order we get:

$$\dot{\rho}_{21'}^{I(3)} = i\chi_{pr} e^{i\delta_{pr}t + ik_{pr}r} \left(\rho_{22}^{(2)} - \rho_{1'1'}^{(2)}\right) - \gamma \rho_{21'}^{I(3)}$$

Here $\rho_{22}^{(2)} = 0$. In the rate approximation limit, we get

$$\rho_{21'}^{I(3)} = -\frac{i\chi_{pr}}{\gamma + i\delta_{pr}} \frac{2\gamma \left|\chi_{pu}\right|^2}{\gamma^2 + \delta_{pu}^2} e^{-\gamma_2 t} e^{i\delta_{pr}t + ik_{pr}r} \tag{4.15}$$

Sequence 6

Again, to the second order in the pump fields, we get the non-zero population terms as:

$$\rho_{1'1'}^{(2)} = \frac{2\gamma \left|\chi_{pu}\right|^2}{\gamma^2 + \delta_{pu}^2} e^{-\gamma_2 t}$$

$$\rho_{0'0'}^{(2)} = -\frac{2\gamma \left|\chi_{pu}\right|^2}{\gamma^2 + \delta_{pu}^2} e^{-\gamma_2 t}$$

To the third order we get:

$$\dot{\rho}_{10}^{I(3)} = i\chi_{pr} e^{i\delta_{pr}t + ik_{pr}r} \left(\rho_{11}^{(2)} - \rho_{00}^{(2)}\right) - \gamma \rho_{10}^{I(3)}$$

Here $\rho_{11}^{(2)} = 0$. In the rate approximation limit, we get

$$\rho_{10}^{I(3)} = \frac{i\chi_{pr}}{\gamma + i\delta_{pr}} \frac{2\gamma \left|\chi_{pu}\right|^2}{\gamma^2 + \delta_{pu}^2} e^{-\gamma_2 t} e^{i\delta_{pr}t + ik_{pr}r} \tag{4.16}$$

4.2.1 Nonlinear Signal

The expressions for the third order coherences calculated in Equations(4.11, 4.12, 4.13, 4.14, 4.15, 4.16) are in the interaction representation, and they can be converted to the Schrödinger picture by using Equation (4.8). It is easy to see that this transformation will result in the term $e^{i\delta_{pr}t}$ being replaced by $e^{-i\omega_{pr}t}$ in going from the interaction to the Schrödinger picture. The nonlinear polarization is given by:

$$\begin{aligned} P^{(3)} &= \mathrm{Tr}\left(\mu\rho^{(3)}\right) \\ &= \mu_{01}\rho_{10}^{(3)} + \mu_{01'}\rho_{1'0}^{(3)} + \mu_{12}\rho_{21}^{(3)} + \mu_{1'2}\rho_{21'}^{(3)} \end{aligned}$$

Combining together the contribution from the six perturbation sequences we get

$$P^{(3)} = \frac{i\chi_{pr}}{\gamma + i\delta_{pr}} \frac{2\gamma \left|\chi_{pu}\right|^2}{\gamma^2 + \delta_{pu}^2} e^{-\gamma_2 t} e^{-i\omega_{pr} t + ik_{pr} r} \left(2\mu_{01} + 2\mu_{01'} - \mu_{12} + \mu_{01'} - \mu_{1'2} + \mu_{01}\right)$$

where the six terms represent the six sequences. By making an assumption that the values of all the dipole matrix elements are equal, it is obtained

$$P^{(3)} = \frac{i\mu_{01}\chi_{pr}}{\gamma + i\delta_{pr}} \frac{2\gamma \left|\chi_{pu}\right|^2}{\gamma^2 + \delta_{pu}^2} 4e^{-\gamma_2 t} e^{-i\omega_{pr} t + ik_{pr} r}$$

Thus we see that the nonlinear polarization generated by the third and fifth sequences, gets canceled by the nonlinear polarization generated by the fourth and the sixth sequences. The total nonlinear polarization generated is only given by the first and second sequence, which together add up to give what you would get with just two independent two level system, which is what we expected. This third order polarization leads to a third order electric field, which is homodyne detected with the probe to yield the dT signal. The expression for the dT signal for this case is

$$\mathrm{dT} = \frac{4kl\hbar}{\epsilon_0} \frac{2\gamma \left|\chi_{pr}\right|^2}{\gamma^2 + \delta_{pr}^2} \frac{2\gamma \left|\chi_{pu}\right|^2}{\gamma^2 + \delta_{pu}^2} 4e^{-\gamma_2 t} \tag{4.17}$$

Hence we obtain just an additional factor of 2 in the expression of the dT signal for two independent 2-level systems with what we had in the expression obtained for a single 2-level system given in Equation(4.10). From the analysis in this section, it can also be guessed that if there is an interaction between the two 2-level systems, such that exciting one system leads to a shift in the resonant energy, then the cancellation obtained in this section will not hold anymore. This is what will be proved formally in the next section, and signatures of the excitation induced shift in the resonant energy in the dT signal will be derived.

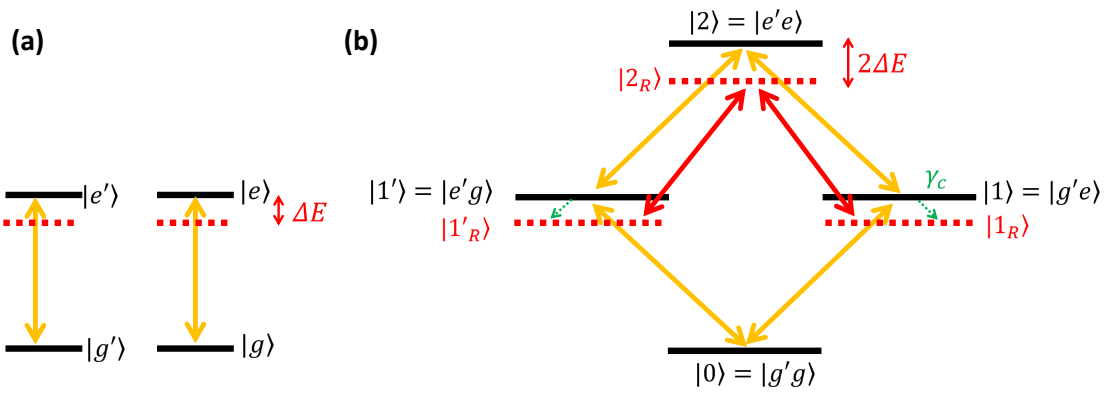

Figure 4.7: Energy level diagram of two interacting 2-level systems.(a)A red shift given by ΔE in the transition energy is included in the system. (b)In the product Hilbert space, transitions at a red shifted energy from the unaltered resonant energy emerge.

4.3 Two 2-level Systems with Excitation Induced Resonant Energy Shift

In this section, it will be considered that optically exciting one of the 2-level systems considered in Section(4.2) leads to a configurational change that red shifts the resonant energy for exciting the other 2-level system. The timescale associated with the configurational change is denoted by $1/\gamma_C$. The energy level diagram of this system can be understood from Figure(4.7). Note that in the limit $\gamma_c = 0$, this system should reduce to the system considered in Section(4.2) of two independent 2 level systems. This fact will be used as a check on the results of the calculation in this section.

For the energy level diagram in Figure(4.7b), two detunings are defined for a given probe energy as follows

$$\delta_{pr} = \omega_0 - \omega_{pr} \tag{4.18}$$

$$\delta'_{pr} = \omega_0 - \Delta E - \omega_{pr} = \delta_{pr} - \Delta E \tag{4.19}$$

The transitions separated by the unaltered energy corresponding to ω_0 are shown by yellow arrows in Figure(4.7b) and the transitions separated by the red shifted energy corresponding to $\omega_0 - \Delta E$ are shown by red arrows in the same figure.

The equations of motion of the density matrix elements are given by

$$\begin{aligned}
\dot{\rho}^I_{10} &= i\left(\chi_{pu}e^{i\delta_{pu}t+ik_{pu}r} + \chi_{pr}e^{i\delta_{pr}t+ik_{pr}r}\right)(\rho_{11}-\rho_{00}) - \gamma\rho^I_{10} \\
\dot{\rho}^I_{21} &= i\left(\chi_{pu}e^{i\delta_{pu}t+ik_{pu}r} + \chi_{pr}e^{i\delta_{pr}t+ik_{pr}r}\right)(\rho_{22}-\rho_{11}) - \gamma\rho^I_{21} \\
\dot{\rho}^I_{2_R1_R} &= i\left(\chi_{pu}e^{i\delta'_{pu}t+ik_{pu}r} + \chi_{pr}e^{i\delta'_{pr}t+ik_{pr}r}\right)(\rho_{2_R2_R}-\rho_{1_R1_R}) - \gamma\rho^I_{2_R1_R} \\
\dot{\rho}^I_{1'0} &= i\left(\chi_{pu}e^{i\delta_{pu}t+ik_{pu}r} + \chi_{pr}e^{i\delta_{pr}t+ik_{pr}r}\right)(\rho_{1'1'}-\rho_{00}) - \gamma\rho^I_{1'0} \\
\dot{\rho}^I_{21'} &= i\left(\chi_{pu}e^{i\delta_{pu}t+ik_{pu}r} + \chi_{pr}e^{i\delta_{pr}t+ik_{pr}r}\right)(\rho_{22}-\rho_{1'1'}) - \gamma\rho^I_{21'} \\
\dot{\rho}^I_{2_R1'_R} &= i\left(\chi_{pu}e^{i\delta'_{pu}t+ik_{pu}r} + \chi_{pr}e^{i\delta'_{pr}t+ik_{pr}r}\right)\left(\rho_{2_R2_R}-\rho_{1'_R1'_R}\right) - \gamma\rho^I_{2_R1'_R} \\
\dot{\rho}_{00} &= -i\left(\chi^*_{pu}e^{-i\delta_{pu}t-ik_{pu}r} + \chi^*_{pr}e^{-i\delta_{pr}t-ik_{pr}r}\right)\left(\rho^I_{10}+\rho^I_{1'0}\right) \\
&\quad +i\left(\chi_{pu}e^{i\delta_{pu}t+ik_{pu}r} + \chi_{pr}e^{i\delta_{pr}t+ik_{pr}r}\right)\left(\rho^I_{01}+\rho^I_{01'}\right) \\
&\quad +\gamma_2\left(\rho_{11}+\rho_{1'1'}+\rho_{1_R1_R}+\rho_{1'_R1'_R}\right) \\
\dot{\rho}_{11} &= i\left(\chi^*_{pu}e^{-i\delta_{pu}t-ik_{pu}r} + \chi^*_{pr}e^{-i\delta_{pr}t-ik_{pr}r}\right)\left(\rho^I_{10}-\rho^I_{21}\right) \\
&\quad -i\left(\chi_{pu}e^{i\delta_{pu}t+ik_{pu}r} + \chi_{pr}e^{i\delta_{pr}t+ik_{pr}r}\right)\left(\rho^I_{01}-\rho^I_{12}\right) \\
&\quad -\gamma_2\rho_{11} - \gamma_c\rho_{11} + \gamma_2\left(\rho_{22}+\rho_{2_R2_R}\right)
\end{aligned}$$

$$
\begin{aligned}
\dot{\rho}_{1_R1_R} &= i\left(\chi^*_{pu}e^{-i\delta'_{pu}t-ik_{pu}r}+\chi^*_{pr}e^{-i\delta'_{pr}t-ik_{pr}r}\right)\left(-\rho^I_{2_R1_R}\right)\\
&\quad -i\left(\chi_{pu}e^{i\delta'_{pu}t+ik_{pu}r}+\chi_{pr}e^{i\delta'_{pr}t+ik_{pr}r}\right)\left(-\rho^I_{1_R2_R}\right)\\
&\quad +\gamma_c\rho_{11}-\gamma_2\rho_{1_R1_R}\\
\dot{\rho}_{1'1'} &= i\left(\chi^*_{pu}e^{-i\delta_{pu}t-ik_{pu}r}+\chi^*_{pr}e^{-i\delta_{pr}t-ik_{pr}r}\right)\left(\rho^I_{1'0}-\rho^I_{21'}\right)\\
&\quad -i\left(\chi_{pu}e^{i\delta_{pu}t+ik_{pu}r}+\chi_{pr}e^{i\delta_{pr}t+ik_{pr}r}\right)\left(\rho^I_{01'}-\rho^I_{1'2}\right)\\
&\quad -\gamma_2\rho_{1'1'}-\gamma_c\rho_{1'1'}+\gamma_2\left(\rho_{22}+\rho_{2_R2_R}\right)\\
\dot{\rho}_{1'_R1'_R} &= i\left(\chi^*_{pu}e^{-i\delta'_{pu}t-ik_{pu}r}+\chi^*_{pr}e^{-i\delta'_{pr}t-ik_{pr}r}\right)\left(-\rho^I_{2_R1'_R}\right)\\
&\quad -i\left(\chi_{pu}e^{i\delta'_{pu}t+ik_{pu}r}+\chi_{pr}e^{i\delta'_{pr}t+ik_{pr}r}\right)\left(-\rho^I_{1'_R2_R}\right)\\
&\quad +\gamma_c\rho_{1'1'}-\gamma_2\rho_{1'_R1'_R}\\
\dot{\rho}_{22} &= i\left(\chi^*_{pu}e^{-i\delta_{pu}t-ik_{pu}r}+\chi^*_{pr}e^{-i\delta_{pr}t-ik_{pr}r}\right)\left(\rho^I_{21}+\rho^I_{21'}\right)\\
&\quad -i\left(\chi_{pu}e^{i\delta_{pu}t+ik_{pu}r}+\chi_{pr}e^{i\delta_{pr}t+ik_{pr}r}\right)\left(\rho^I_{12}+\rho^I_{1'2}\right)\\
&\quad -2\gamma_2\rho_{22}\\
\dot{\rho}_{2_R2_R} &= i\left(\chi^*_{pu}e^{-i\delta_{pu}t-ik_{pu}r}+\chi^*_{pr}e^{-i\delta_{pr}t-ik_{pr}r}\right)\left(\rho^I_{2_R1_R}+\rho^I_{2_R1'_R}\right)\\
&\quad -i\left(\chi_{pu}e^{i\delta_{pu}t+ik_{pu}r}+\chi_{pr}e^{i\delta_{pr}t+ik_{pr}r}\right)\left(\rho^I_{1_R2_R}+\rho^I_{1'_R2_R}\right)\\
&\quad -2\gamma_2\rho_{2_R2R}
\end{aligned}
$$

The equations of motion of the complex conjugate of the coherences are not written anymore. The perturbation sequences from the right part of the energy level diagram leading to the nonlinear signal are shown in Figure(4.8).

First Order

To the first order in the pump field we get the coherences

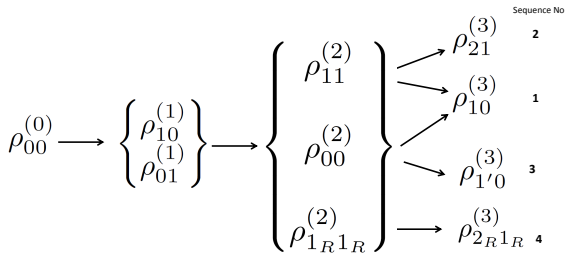

Figure 4.8: Perturbation Sequences from the right part of the energy level diagram.

$$\rho_{10}^{I(1)} = \frac{-i\chi_{pu}}{\gamma + i\delta_{pu}} e^{i\delta_{pu}t + ik_{pu}r}$$

We also get the complex conjugate

$$\rho_{01}^{I(1)} = \frac{i\chi_{pu}^*}{\gamma - i\delta_{pu}} e^{-i\delta_{pu}t - ik_{pu}r}$$

Second Order

To the second order in the pump field we have

$$\begin{aligned} \dot{\rho}_{11}^{(2)} &= i\left(\chi_{pu}^* e^{-i\delta_{pu}t - ik_{pu}r}\right)\left(\rho_{10}^{I(1)}\right) - i\left(\chi_{pu} e^{i\delta_{pu}t + ik_{pu}r}\right)\left(\rho_{01}^{I(1)}\right) \\ &\quad +\gamma_2\left(-\rho_{11}^{(2)}\right) - \gamma_c\rho_{11}^{(2)} \end{aligned}$$

Solving this for delta function pulse gives us:

$$\rho_{11}^{(2)} = \frac{2\gamma\left|\chi_{pu}\right|^2}{\gamma^2 + \delta_{pu}^2} e^{-(\gamma_2+\gamma_c)t} \tag{4.20}$$

For population in the $|1_R\rangle$ state, we get:

$$\dot{\rho}_{1_R1_R}^{(2)} + \gamma_2\rho_{1_R1_R}^{(2)} = \gamma_c\rho_{11}^{(2)} = \gamma_c\frac{2\gamma\left|\chi_{pu}\right|^2}{\gamma^2 + \delta_{pu}^2} e^{-(\gamma_2+\gamma_c)t}$$

Using integrating factor $e^{\gamma_2 t}$ we obtain:

$$\frac{d}{dt}\left(\rho^{(2)}_{1_R 1_R} e^{\gamma_2 t}\right) = \frac{\gamma_c 2\gamma \left|\chi_{pu}\right|^2}{\gamma^2 + \delta^2_{pu}} e^{-\gamma_c t}$$

$$\begin{aligned}
\rho^{(2)}_{1_R 1_R}(t) &= \rho^{(2)}_{1_R 1_R}(0) e^{-\gamma_2 t} + \frac{\gamma_c 2\gamma \left|\chi_{pu}\right|^2}{\gamma^2 + \delta^2_{pu}} e^{-\gamma_2 t} \int_0^t \mathrm{d}t'\, e^{-\gamma_c t'} \\
&= \frac{2\gamma \left|\chi_{pu}\right|^2}{\gamma^2 + \delta^2_{pu}} e^{-\gamma_2 t} \left(1 - e^{-\gamma_c t}\right)
\end{aligned}$$

Hence, we get

$$\rho^{(2)}_{1_R 1_R} = \frac{2\gamma \left|\chi_{pu}\right|^2}{\gamma^2 + \delta^2_{pu}} \left(e^{-\gamma_2 t} - e^{-(\gamma_2 + \gamma_c)t}\right) \tag{4.21}$$

For population in the ground state we get:

$$\dot{\rho}^{(2)}_{00} = -i\left(\chi^*_{pu} e^{-i\delta_{pu} t - i k_{pu} r}\right)\left(\rho^{I(1)}_{10}\right) + i\left(\chi_{pu} e^{i\delta_{pu} t + i k_{pu} r}\right)\left(\rho^{I(1)}_{01}\right) + \gamma_2\left(\rho^{(2)}_{11} + \rho^{(2)}_{1_R 1_R}\right)$$

Plugging in solutions of the first order coherence and the second order decay, and assuming a delta pulse for the pump ($\chi_{pu} = \chi_{pu}\delta(t)$) gives us

$$\begin{aligned}
\dot{\rho}^{(2)}_{00} &= \frac{2\gamma \left|\chi_{pu}\right|^2}{\gamma^2 + \delta^2_{pu}} \left(-\delta(t) + \gamma_2\left(e^{-(\gamma_2+\gamma_c)t} + \left(e^{-\gamma_2 t} - e^{-(\gamma_2+\gamma_c)t}\right)\right)\right) \\
&= \frac{2\gamma \left|\chi_{pu}\right|^2}{\gamma^2 + \delta^2_{pu}} \left(-\delta(t) + \gamma_2 e^{-\gamma_2 t}\right)
\end{aligned}$$

Integrating gives us:

$$\rho^{(2)}_{00} = \frac{2\gamma \left|\chi_{pu}\right|^2}{\gamma^2 + \delta^2_{pu}} \left(-1 + \gamma_2 \frac{1}{\gamma_2}\left(1 - e^{-\gamma_2 t}\right)\right)$$

Hence, we get for the second order ground state population:

$$\rho_{00}^{(2)} = -\frac{2\gamma \left|\chi_{pu}\right|^2}{\gamma^2 + \delta_{pu}^2} e^{-\gamma_2 t} \tag{4.22}$$

Now we can have a check on the calculation by seeing from Equations(4.20,4.21,4.22) that

$$\rho_{00}^{(2)} + \rho_{1_R 1_R}^{(2)} + \rho_{11}^{(2)} = 0$$

Third Order

Sequence 1

$$\dot{\rho}_{10}^{I(3)} = i\left(\chi_{pr} e^{i\delta_{pr}t + ik_{pr}r}\right)\left(\rho_{11}^{(2)} - \rho_{00}^{(2)}\right) - \gamma\rho_{10}^{I(3)}$$

In the rate equation limit, we get:

$$\dot{\rho}_{10}^{I(3)} = \frac{i\chi_{pr} e^{i\delta_{pr}t + ik_{pr}r}}{\gamma + i\delta_{pr}}\left(\rho_{11}^{(2)} - \rho_{00}^{(2)}\right)$$

This gives us

$$\rho_{10}^{I(3)} = \frac{i\chi_{pr}}{\gamma + i\delta_{pr}} \frac{2\gamma \left|\chi_{pu}\right|^2}{\gamma^2 + \delta_{pu}^2}\left(e^{-(\gamma_2+\gamma_c)t} + e^{-\gamma_2 t}\right) e^{i\delta_{pr}t + ik_{pr}r}$$

Sequence 2

$$\dot{\rho}_{21}^{I(3)} = i\left(\chi_{pr} e^{i\delta_{pr}t + ik_{pr}r}\right)\left(\rho_{22}^{(2)} - \rho_{11}^{(2)}\right) - \gamma\rho_{21}^{I(3)}$$

In the rate equation limit

$$\rho_{21}^{I(3)} = \frac{i\chi_{pr}}{\gamma + i\delta_{pr}} \frac{2\gamma \left|\chi_{pu}\right|^2}{\gamma^2 + \delta_{pu}^2}\left(-e^{-(\gamma_2+\gamma_c)t}\right) e^{i\delta_{pr}t + ik_{pr}r}$$

Sequence 3

$$\dot{\rho}_{1'0}^{I(3)} = i\left(\chi_{pr}e^{i\delta_{pr}t+ik_{pr}r}\right)\left(\rho_{1'1'}^{(2)} - \rho_{00}^{(2)}\right) - \gamma\rho_{1'0}^{I(3)}$$

In the rate equation limit

$$\rho_{1'0}^{I(3)} = \frac{i\chi_{pr}}{\gamma + i\delta_{pr}}\frac{2\gamma\left|\chi_{pu}\right|^2}{\gamma^2+\delta_{pu}^2}\left(e^{-\gamma_2 t}\right)e^{i\delta_{pr}t+ik_{pr}r}$$

Here we make another check on the calculation. If we put $\gamma_c = 0$, we see that sequence 2 and sequence 3 will cancel, like they did for the case of two independent 2 level systems.

Sequence 4

$$\dot{\rho}_{2_R1_R}^{I(3)} = i\left(\chi_{pr}e^{i\delta'_{pr}t+ik_{pr}r}\right)\left(\rho_{2_R2_R}^{(2)} - \rho_{1_R1_R}^{(2)}\right) - \gamma\rho_{21_c}^{I(3)}$$

In the rate equation limit

$$\rho_{2_R1_R}^{I(3)} = \frac{i\chi_{pr}}{\gamma + i\delta'_{pr}}\frac{2\gamma\left|\chi_{pu}\right|^2}{\gamma^2+\delta_{pu}^2}\left(e^{-(\gamma_2+\gamma_c)t} - e^{-\gamma_2 t}\right)e^{i\delta'_{pr}t+ik_{pr}r}$$

4.3.1 Nonlinear Signal

By symmetry, the calculation for the left side of Figure(4.7) will proceed just the same way as above, and an additional factor of 2 will be picked up by it. As before, after converting the above calculated coherences to the Schrödinger picture, and finding the expectation value of the dipole operator and putting it in Maxwells equation, and homodyning with the probe, we get:

$$\begin{aligned} \mathrm{dT} &= \frac{4kl\hbar}{\epsilon_0}\frac{2\gamma 2\gamma\left|\chi_{pr}\right|^2\left|\chi_{pu}\right|^2}{\gamma^2+\delta_{pu}^2}\left(\frac{e^{-(\gamma_2+\gamma_c)t}+e^{-\gamma_2 t}}{\gamma^2+\delta_{pr}^2}-\frac{e^{-(\gamma_2+\gamma_c)t}}{\gamma^2+\delta_{pr}^2}\right. \\ &+ \left.\frac{e^{-\gamma_2 t}}{\gamma^2+\delta_{pr}^2}+\frac{e^{-(\gamma_2+\gamma_c)t}-e^{-\gamma_2 t}}{\gamma^2+\delta_{pr}'^2}\right) \end{aligned}$$

This can be simplified to get

$$\mathrm{dT} = \frac{4kl\hbar}{\epsilon_0}\frac{2\gamma 2\gamma\left|\chi_{pr}\right|^2\left|\chi_{pu}\right|^2}{\gamma^2+\delta_{pu}^2}\left(\frac{2e^{-\gamma_2 t}}{\gamma^2+\delta_{pr}^2}+\frac{e^{-(\gamma_2+\gamma_c)t}-e^{-\gamma_2 t}}{\gamma^2+\delta_{pr}'^2}\right)$$

Slightly re-writing this relation and using Equation(4.19), we get

$$\mathrm{dT} = \frac{4kl\hbar}{\epsilon_0}\frac{2\gamma 2\gamma\left|\chi_{pr}\right|^2\left|\chi_{pu}\right|^2}{\gamma^2+\delta_{pu}^2}\left(\frac{2e^{-\gamma_2 t}}{\gamma^2+\delta_{pr}^2}-\frac{e^{-\gamma_2 t}\left(1-e^{-\gamma_c t}\right)}{\gamma^2+\left(\delta_{pr}+\Delta E\right)^2}\right) \tag{4.23}$$

At this point, we can again have a check on our calculation. For $\gamma_c = 0$, the second term above cancels and we are left with just one lorentzian, multiplied by an exponential decay. This is what we had for just two independent two level systems. Now consider that there is a blue shift of the transition for the second excited state, after the first state is excited. Let this be given given by $\Delta E = -\gamma$. Figure (4.9) shows the plot of the simulated decay signals obtained from Equation(4.23) at three different probe wavelengths corresponding to $\delta_{pr} = -0.33\gamma$, 0.77γ, 1.77γ. These plots are normalized to the value of dT at zero delay. Note that a negative (positive) value of δ_{pr} means the probe laser is blue (red) detuned from the transition.

We can further rewrite the expression of dT to obtain:

$$\mathrm{dT} = \frac{4kl\hbar}{\epsilon_0}\frac{2\gamma 2\gamma\left|\chi_{pr}\right|^2\left|\chi_{pu}\right|^2}{\gamma^2+\delta_{pu}^2}\left(\left(\frac{2}{\gamma^2+\delta_{pr}^2}-\frac{1}{\gamma^2+\delta_{pr}'^2}\right)e^{-\gamma_2 t}+\frac{1}{\gamma^2+\delta_{pr}'^2}e^{-(\gamma_2+\gamma_c)t}\right) \tag{4.24}$$

From this expression some key points can be noted:

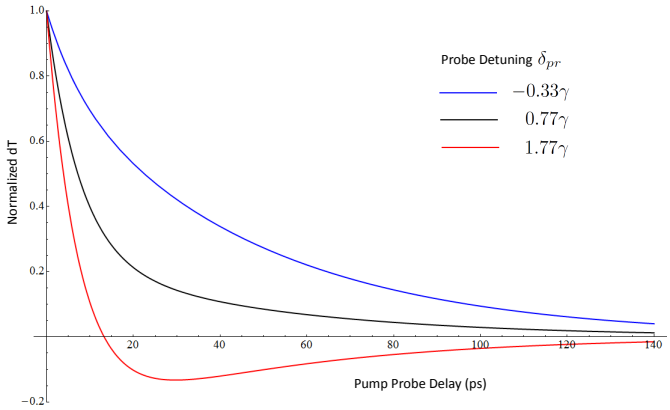

Figure 4.9: Simulation of dT signal for delayed interaction. In the simulation, $\gamma_2 = \frac{1}{47\text{ps}}$ and $\gamma_c = \frac{1}{9\text{ps}}$

1. The dT signal can be expressed as a sum of time exponentials, where the prefactors of the exponentials are probe energy/wavelength dependent.

2. Since the prefactors of the time exponentials are wavelength dependent, each exponential will contribute by different amounts for different probe wavelengths. This will result in the scaled version of the dT signals for various probe wavelengths seemingly having different decay kinetics.

3. The functional form of Equation(4.24) gives us a prescription to analyze dT data that shows probe energy dependent dynamics so that a energy level diagram can be constructed from the analysis. A global fit to the data can be carried out, such that the fit searches for common time exponentials for different probe energy decay scans. Once these common time exponentials are obtained, their prefactors can be plotted out as a function of probe energy, to yield a Decay Associated Spectra (DAS). The spectra in the DAS can then be fitted to sums of lorentzians.

4. If there is an excitation induced change in the resonant energy, then the decomposed fit of the spectra should reveal negative lorentzians that are shifted

in energy.

4.4 Chapter Summary

The nonlinear dT signal was calculated for the simplest case of a nearly resonant laser with a 2-level system. It was shown that in the $\chi^{(3)}$ regime, the nonlinear signal would scale linearly with the pump and probe powers. It was also noted that in the $\chi^{(3)}$ regime, the obtained dT signal can probe two excitations from energy conservation considerations. An energy level diagram was constructed that allows for an optically induced configurational change that modifies the excitation energy of a second excitation, after an initial excitation. From the analytical form of the calculated dT signal for this system, it was seen that by globally fitting probe energy dependent decay scans to common time exponentials, the form of the prefactors as a function of wavelength will have signature effects identifying shifts in the resonant energy. This data analysis technique will be used in Chapter (VI) to analyze the dT data obtained from two color pump-probe experiments on SWCNTs, and to construct a model that could explain some aspects of the data.

CHAPTER V

Sample Characterization and Optical Setup

In this chapter, the SWCNT samples enriched in the $(6,5)$ chiralities used for the experiments in this thesis are described. The process used for individualizing the SWCNTs by embedding them in surfactant micelles is discussed in some detail. Data is presented from linear absorption studies that identifies the excitonic transitions E_{11} and E_{22} of the $(6,5)$ chirality in the sample. It is shown that luminescence can be obtained from this sample, which indicates that the individualization process was successful. Finally the optical setup used in differential transmission (dT) experiments is described, and power-study data is presented that indicate that the dT experiments are in the $\chi^{(3)}$ regime.

5.1 SWCNT Individualization

We obtain SWCNTs enriched in the $(6,5)$ chirality, grown using the CoMoCAT® process from SouthWest NanoTechnologies. The CoMoCAT® can be briefly described as consisting of the following steps[26]:

1. Precursors cobalt nitrate and ammonium heptamolybdate are used to create bi-metallic catalyst (Co-Mo), which gets adsorbed on a silica support

2. Decomposition of CO to C and CO_2 takes place at pressures of $1-10$ atm and

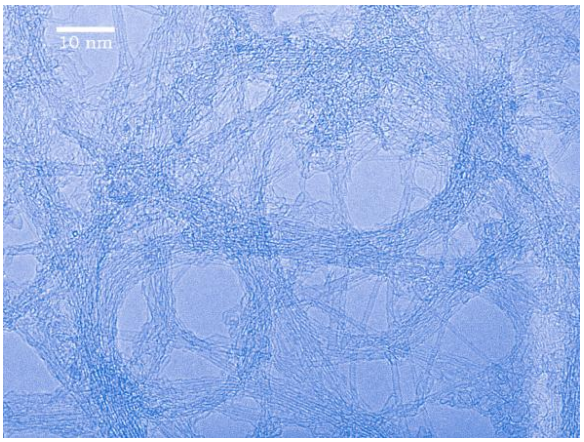

Figure 5.1: A typical TEM image of the SWCNT sample in freeze dried powder form. Source: SouthWest NanoTechnologies

temperatures $700° - 950°$C.

3. Accumulation of C takes place on the catalyst nanoclusters on the silica support, leading to the growth of SWCNTs.

This process can lead to a very narrow chirality distribution of the obtained SWCNTs. The sample obtained by us is in a freeze dried powder form, and a TEM image of such a sample obtained from SouthWest NanoTechnologies is shown in Figure(5.1). This figure indicates the the SWCNTs are inter-twined and bundled. To be able to study properties of pristine SWCNT, it is important to isolate them and prevent tube bundling which leads to rapid relaxation pathways, quenching photoluminescence. We use an anionic surfactant sodium deoxycholate to exfoliate and disperse the SWCNT bundles, with individual nanotubes getting embedded within soap micelles. This process [47] involves the following steps:

1. The surfactant solution is prepared by dissolving 500 mg of sodium deoxycholate in 25 ml of water. The resistivity of the water was measured to be $18.1\,\mathrm{M}\Omega - \mathrm{cm}$.

2. 5 mg of the SWCNT sample in the freeze dried power form, is dissolved in 25 ml of the surfactant solution.

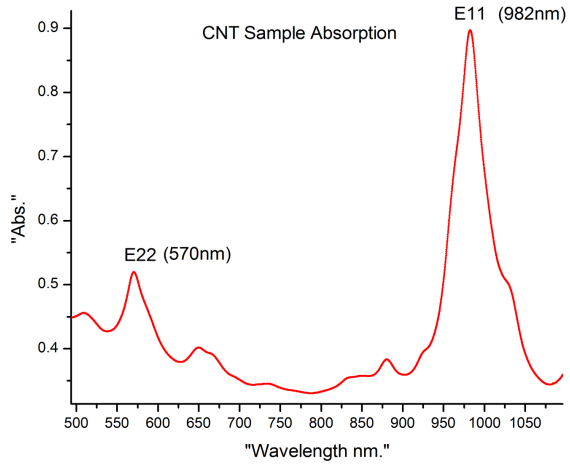

Figure 5.2: VIS-NIR absorption spectrum for SWCNT-surfactant solution. The E_{22} and E_{11} energy levels of the (6,5) SWCNT are labeled.

3. The resulting aqueous solution of the nanotubes and surfactant solution is vigorously sonicated with a cup-horn sonicator (Branson Sonifier 250) operated at 140 Wfor 2 hours. Sonication was done in a pulsed manner, and the mixture was kept in an ice bath to minimize heating the sample during sonication. The surfactant gets adsorbed on the nanotube surface by hydrophobic $\pi - \pi$ interactions, and during sonication helps debundle the tubes by overcoming the van der Waals forces between the tubes through hydrophilic interactions.

4. The resulting solution is kept in a centrifuge (Sorvall RC 5B Plus) for two hours at a centrifugal force of 27,000g. This causes carbonaceous impurities, large nanotube bundles and the catalyst impurities of Co and Mo to settle down and the upper 50% of the resultant supernatant is used in our measurements.

5.2 VIS-NIR and PLE Identification of Energy Levels

The E_{22} and E_{11} energy levels of the (6,5) SWCNT dominantly present in our sample are identified in a VIS-NIR absorption spectrum in Figure(5.2). The smaller

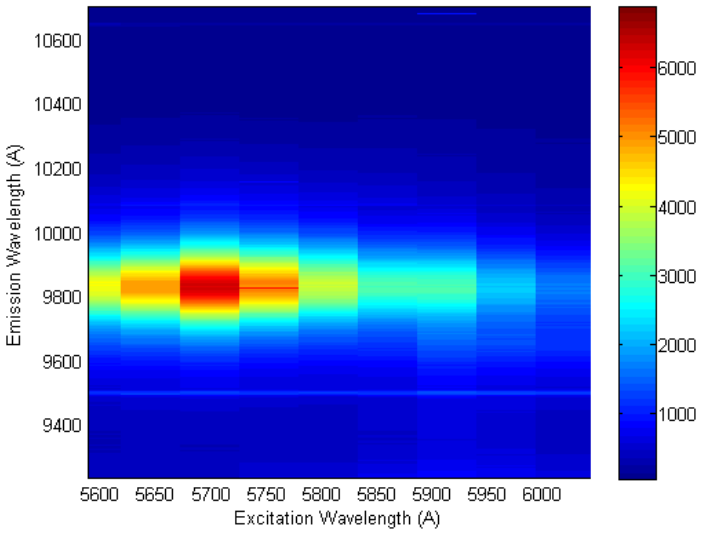

Figure 5.3: Photoluminescence Excitation Spectroscopy (PLE). The resonances in the excitation and emission spectra correspond to the E_{22} and E_{11} energy transitions respectively.

peak at around 650nm corresponds to the E_{22} transition of the (7,6) chirality that is also present in our sample in small amounts. The dominance of the peaks corresponding to the E_{22} and E_{11} transitions of the $(6,5)$ SWCNTs indicates that the sample is enriched in this chirality. We then carried out photoluminescence excitation (PLE) spectroscopy on spin-coated samples on a glass substrate and observed bright fluorescence from the E_{11} level, when the sample is excited at the E_{22} energy resonance using a tunable dye laser. The PL emission was collected in a reflection geometry, and was dispersed using a grating onto a liquid nitrogen cooled CCD. We show a PLE map in Figure(5.3), and the E_{22} and E_{11} energy resonances are clearly identifiable in excitation and emission spectra respectively. The observance of PL from our sample is indicative of the fact that the SWCNT have been well individualized and are encapsulated in surfactant micelles.

5.3 Differential Transmission Setup

In this section we will describe the setup used for obtaining the dT signal. In Section(3.1) it was shown that the differential transmission signal detects the third order nonlinear response of a sample, homodyne detected with the probe

$$I_{\text{probe,pump on}} - I_{\text{probe,pump off}} \propto 2\text{Re}(E^{(3)}_{\text{pump,probe}} E^{*}_{\text{probe}}) \tag{5.1}$$

This expression shows that the third order nonlinear signal can be obtained by simply measuring the transmission of the probe through the sample with the pump laser on, and then subtracting the transmission of the probe through the sample when the pump is off. However since the nonlinear optical response of most samples is very weak, compared to the noise due to intensity fluctuations of the probe laser, this would be a very weak signal to detect. However phase sensitive lockin techniques can be used where the detection bandwidth can be greatly reduced, thereby reducing the contribution of noise in the measurement, and this weak nonlinear signal can easily be extracted out of the noise. This can be achieved by using the kind of setup shown in Figure(5.4). In this setup, the intensity of the pump beam is modulated by acousto-optic modulators (AOM) at a given reference frequency. This causes the nonlinear signal predicted by Equation(5.1), to occur at the reference frequency in the photocurrent obtained from the probe. Thus, by demodulating the photocurrent obtained from the probe by a lockin amplifier at the reference frequency, this weak signal can be isolated from the noise. The advantage of this method is due to the fact that a lockin amplifier acts as a very narrow frequency filter at the reference frequency. So, by modulating the pump intensity, the weak nonlinear signal is upshifted to the reference frequency and the lockin amplifier will be able to extract this signal from the noise background.

The experimental schematic depicted in Figure(5.4) is that of a degenerate ge-

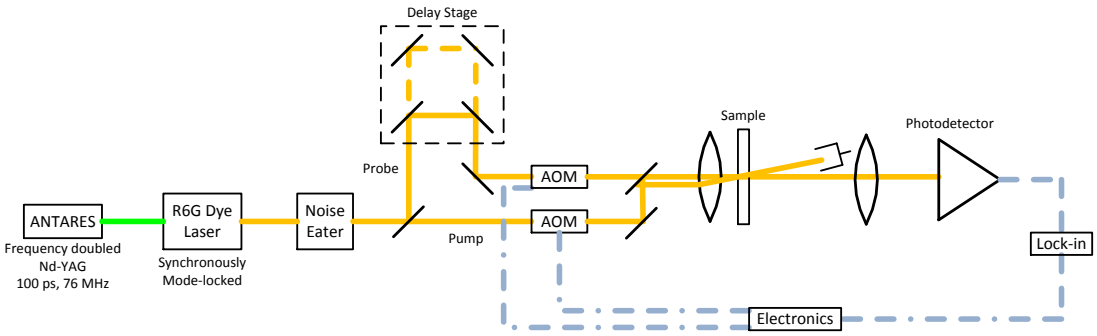

Figure 5.4: Experimental schematic for time-dependent studies. AOM's are used for intensity modulation of the pump and probe beams. The photocurrent obtained due to the probe beam is demodulated using a Lockin amplifier.

ometry: the pump and probe beams are obtained by splitting of the beam from the same laser. These were the first set of dT measurement conducted in this thesis. The pump and probe beams were obtained from a dye laser (Coherent 702) with the Rhodamine 6G dye in it, which is synchronously pumped by mode-locked frequency doubled 100 ps pulses at 532 nm, obtained from a Nd-YAG laser (Coherent Antares) at a repetition rate of 76 MHz. A silicon photodiode monitors the probe transmission through the sample, and a lockin is used to demodulate the photocurrent at the pump modulation frequency to obtain the signal. The pump is spatially blocked after the sample before it reaches the detector. In the double chopping geometry, both the pump and probe are intensity modulated at two different frequencies, and the photocurrent in this case is demodulated by the lockin at the difference of these two frequencies. The double chopping geometry helps get rid of any signal that would be detected in the single chopping scheme due to just the pump scatter, but at the cost of throwing away half of the signal. The pump and probe laser can be tuned to the E_{22} resonance of the $(6, 5)$ chirality SWCNT, that was identified in Figure(5.3). For all the dT data presented, the pump and probe lasers will be tuned to the E_{22} transition. The optical density of the sample at these wavelengths is 0.53, which

means that about 70% of the incident light gets absorbed.

5.3.1 Interferometric Noise at Zero Delay in Degenerate dT Experiments

In the previous section, it was seen that in a differential transmission experiment, only the probe is detected. The nonlinear signal is homodyne detected with the probe. However, if even a tiny bit of the pump laser leaks into the detector, it results in interferometric noise that is referred to as homodyning noise. In our case, the sample scatters a lot of light. So even if the pump and probe beams are spatially separated, or separated using polarization, a small leak through of the pump onto the detector is inevitable. The electric fields for the pump and probe beams just before the detector can be written in the following way:

$$E_{pu}(t) = E_{0,pu} e^{-if_{pu}t} e^{-at^2} e^{-i\omega_{pu}t + i\vec{k}_{pu}.\vec{r} + i\phi(t)}$$

$$E_{pr}(t) = E_{0,pr} e^{-if_{pr}t} e^{-a(t-\tau)^2} e^{-i\omega_{pr}t + i\vec{k}_{pr}.\vec{r}}$$

Here, the optical frequencies are denoted by ω and the modulation frequency is given by f. It is also assumed that the pulses have a Gaussian envelope in time with the pulses being separated by τ in time. We have taken the optical frequencies of the pump and probe to be different for now. The ϕ in the expression for the pump pulse accounts for the phase difference between the pump and probe. If there is interferometric stability between the pump and probe, this ϕ is a constant of time. In general, because of drifts in the optical path caused by vibrations of the optical table, etc, ϕ is a function of time. The photocurrent produced in the detector due to interference of the pump and probe on the detector is proportional to the time average of the square of the electric fields:

$$I_{ph-current} \propto |E_{pu}(t) + E_{pr}(t)|^2$$

The lockin will isolate only those terms in the photocurrent which are at the difference modulation frequency, which in this case is $f_1 - f_2$. Consider the cross-terms that survive:

$$E_{pu}(t)E^*_{pr}(t) + E^*_{pu}(t)E_{pr}(t)$$

These cross terms have a functional form given by the following expression at zero delay between the pump and probe.

$$E_{pu}(t)E^*_{pr}(t) \propto E_{0,pr}E_{0,pu}e^{-i\left((f_{pu}-f_{pr})t+(\omega_{pu}-\omega_{pr})t+\left(\vec{k}_{pr}-\vec{k}_{pu}\right).\vec{r}+\phi(t)\right)} \tag{5.2}$$

Thus, we see that for the degenerate case, when $\omega_{pu} = \omega_{pr}$ this term will oscillate at the difference frequency $f_{pu} - f_{pr}$. Since the lockin picks up signal at this frequency, this will lead to a signal on the lockin. However due to the varying $\phi(t)$ this signal will not be constant, but will vary as the phase between the pump and probe varies. Thus, this term will contribute to a very noisy signal, which is known as the homodyning noise. Now, if the pump and probe frequencies are offset with respect to each other, this term will no longer appear at the difference frequency $f_{pu} - f_{pr}$. The amount of offset should be larger than the bandwidth of detection of the lockin system at the reference frequency of $f_{pu} - f_{pr.}$ For typical values of the lockin time constants used for the dT experiments, the bandwidth of detection is on order of 1 Hz. This frequency offset is easily achieved by using traveling wave AOM's to modulate the beams, where the pump and probe beams are taken as opposite orders. From considerations of energy conservation, the diffracted beam from TW-AOMs undergoes a frequency shift of $n\Omega$, where n is the order of diffraction, and Ω is the acoustic frequency, which is 40 MHz in our case. By taking opposite order diffracted beams for the pump and

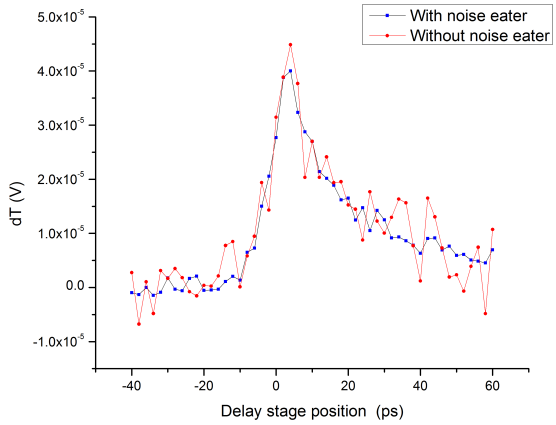

Figure 5.5: dT scans demonstrating reduction in experimental noise with the aid of noise eaters.

probe ($n = \pm 1$), we obtain the frequency offset $|\omega_{pu} - \omega_{pr}| = 80\,\text{MHz}$, which is much larger than the bandwidth of detection, and hence the term given by Equation(5.2) will not be detected by the lockin.

It is interesting to note, that interferometric stability is not required to observe the coherent artifact signal which was mentioned in Section(3.4), even though it occurs at zero delay. The reason is that the homodyne detected coherent artifact signal goes as

$$I_{\text{coherent artifact}} \propto \text{Re}\left(E^{(3)}E^{*}_{pr}\right) = \left(\chi^{(3)}E_{pu}E^{*}_{pu}E_{pr}\right)E^{*}_{pr}$$

In this expression, we see that the phase noise $e^{i\phi(t)}$ cancels out, and thus interferometric stability is not required to observe the coherent artifact. Note that this is true only at the level of presentation used for this thesis. A more complete treatment needs to consider the time rate of change of phase and the various relaxation times in the density matrix equations, which would lead to some terms requiring interferometric stability to be able to be observed in the lab.

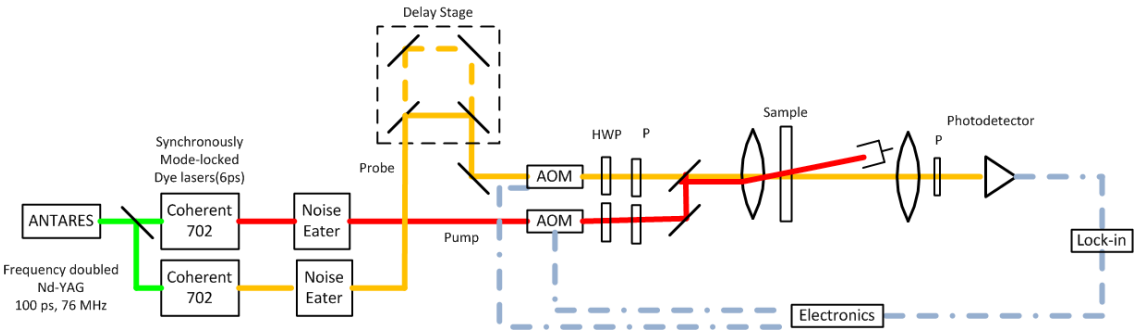

Figure 5.6: Experimental schematic for two color dT studies. The beam from the Antares pump laser is split to synchronously pump the two Coherent 702 dye lasers.

5.3.2 Use of Noise Eaters to Suppress Common-mode Noise

The setup shown in Figure(5.4) also contains a homebuilt noise eater to stabilize the output of the dye laser. The optical power of the first order diffracted beam from an acousto-optic modulator (AOM) is monitored and the RF power to the AOM is adjusted by a PI (Proportional-Integral) controller to keep the optical power constant. This helps in reducing the noise within the measurement bandwidth of about 1 Hz at 2 KHz to go down by a factor of at least 2. This reduction in the noise on the dT signal is shown in Figure(5.5). The design for such a noise eater was suggested by a colleague, John Schaibley.

5.3.3 Two Color Differential Transmission Experiments

The linewidth in the linear absorption for the E_{22} absorption peak shown in Figure(5.2) is about 100 meV. According to photon echo experiments conducted by other groups [18] on the E_{11} transition, the homogeneous linewidth at room temperature has been measured to be 178 cm^{-1}, which corresponds to 22 meV. This indicates that the linewidth in the linear spectroscopy scans is dominated by inhomogeneous broadening. Such inhomogeneous broadening could arise due to variation in

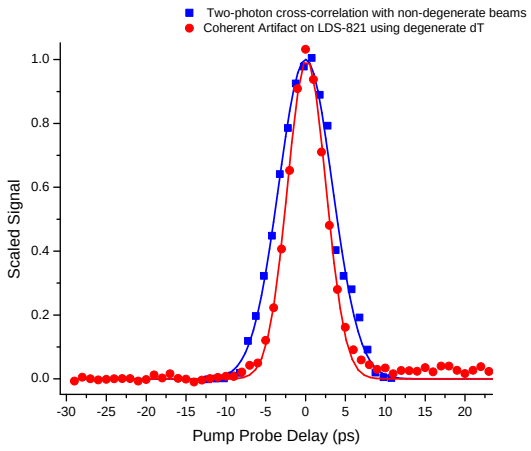

Figure 5.7: Measuring the cross-correlation of the pulses for the degenerate and non-degenerate dT experiments. The red line is a Gaussian fit (FWHM 6 ps) to the coherent artifact obtained in a degenerate experiment on a test sample of LDS-821. The blue line is a Gaussian fit (FWHM 8 ps) to a two photon signal obtained from a wide bandgap GaP photodetector.

the local dielectric environment of the optically excited excitons on the SWCNT[28]. The spectral linewidth of the picosecond dye lasers used in our experiment is about 0.7 meV. Hence in a two color experiment, with the pump laser parked at a given energy/wavelength resonant with the E_{22} transition, we expect to selectively excite the SWCNT excitons which would be resonant with the pump laser. Then, by scanning the wavelength of a second probe laser across the E_{22} resonance, we might be able to detect small changes in the resonant frequency upon optical excitation. In such a scheme, it would be important for the pump and probe laser pulses to be synchronized. Such an experimental configuration is shown in Figure(5.6). In this setup, the same mode-locked pump laser is split to synchronously pump two dye lasers (Coherent 702).

A check on whether the pulses obtained from the two dye lasers in this scheme are synchronized is shown by measuring the instrument response function as shown in Figure(5.7) for both the degenerate and the non-degenerate dT geometry. For the two color experimental geometry, we chose to measure the cross-correlation of the

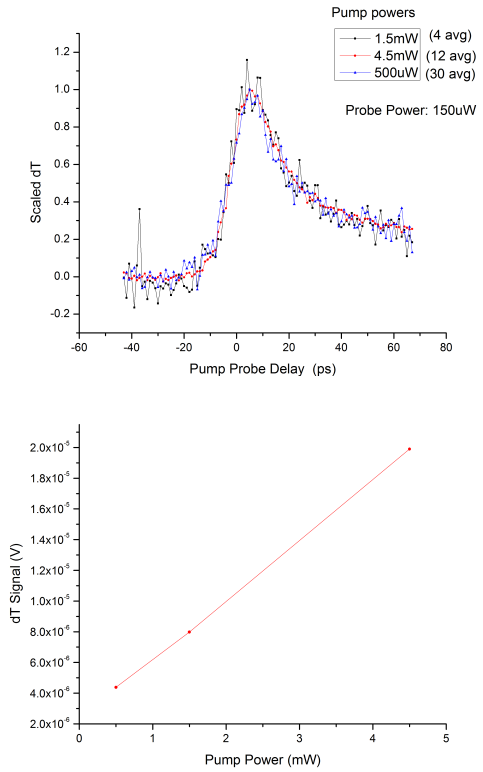

Figure 5.8: Pump power dependence shows dT signals are in the $\chi^{(3)}$ regime. (Top) No change in decay kinetics is observed for different pump powers. (Bottom) The peak dT signal scales linearly with pump power.

pump and probe beam by using two-photon signals obtained in a wide bandgap GaP photodiode. This method is more compact than other ways of measuring the cross correlation since the material with the nonlinear response and the photodiode are combined as one device[43]. The measured cross-correlation for the two color case is only slightly wider than the width of a coherent artifact signal obtained from a laser dye in a degenerate geometry, which is due to jitter between the pulses from the two lasers.

It was shown in Equation(4.10) that in the $\chi^{(3)}$ regime, the measured dT signal should scale linearly with the pump and probe powers. In Figure(5.8) it is shown that this is indeed the case for the highest powers used in the dT experiments in this thesis. We also want to note that we find no dependence in the decay kinetics as a function of

power. This is in contrast to other works in the literature[31] where power dependent decay rates are obtained and attributed to exciton-exciton annihilation. We speculate that this is due to the fact that the high repetition rate of our laser systems allows us to use small values of pump fluence (6μJ/pulse/cm^2=10^{13}photons/pulse/cm^2) on the sample for good signal to noise. Also, the longer pulses used in our experiments give rise to smaller peak powers on the sample compared to experiments that are carried out with femtosecond lasers. A wavelength dependent offset has been subtracted out of the dT signals presented in this thesis. This offset is shown in Appendix((A)), along with a discussion of some physical mechanisms that could be responsible for it.

5.4 Chapter Summary

In this chapter the process that was used to exfoliate and disperse the SWCNT sample so that individual SWCNT could be encapsulated in surfactant micelles was discussed. The linear absorption data on this sample was shown which indicates that the sample is rich in the $(6, 5)$ chirality. SWCNT individualization was confirmed by carrying out PLE, in which it was observed that optically exciting excitons in the E_{22} state results in fluorescence from the E_{11} state. The optical setups used for dT measurements were discussed. It was shown that the obtained dT signals when the pump and probe lasers were resonant with the E_{22} resonance were in the $\chi^{(3)}$ regime.

CHAPTER VI

Experimental Observation of Excitation Induced Resonant Energy Shifts

In this chapter, experimental results of two color pump probe experiments that demonstrate excitation induced resonant energy shifts in SWCNTs are presented. We will quantify the energy shifts and associated timescales of the fits we infer from our data analysis and show the extracted Decay Associated Spectra (DAS). We will use the prescription described in Chapter(IV) to come up with an energy level structure that can describe the results of the two color experiments. The equations of motion of this proposed energy level will be solved perturbatively, to obtain expressions of a form that can justify the DAS obtained from the fits.

6.1 Two Color dT Signal on SWCNT

The experimental setup for the two color experiment was described in Chapter(V). We use one of the synchronously mode-locked Coherent 702 dye laser with the gain medium as Rhodamine 6G to act as a pump in the experiment, and we keep it parked at an energy of 2166.76 meV(corresponding to a wavelength of 572.21 nm). From the PLE data shown in Chapter(V), this corresponds to the pump being resonant with the E_{22} transition. We use another Coherent 702 dye laser (pumped synchronously

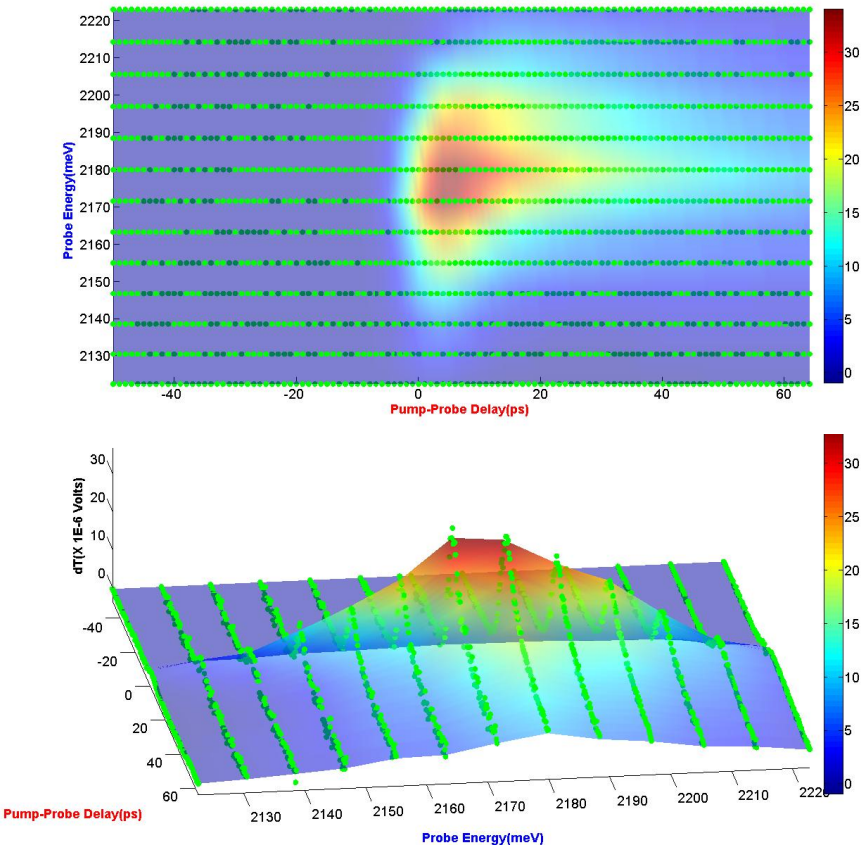

Figure 6.1: Two color dT data on SWCNTs: The green spheres are the data points, and the colored surface is the global fit

with the same pump laser as the first dye laser), and scan its energy from about 2116 meV to about 2214 meV(about 586 nm to 560 nm). Thus the probe is scanned across the E_{22} transition. For each probe energy used in the experiment, time scans were taken by delaying the probe with respect to the pump using an optical delay stage. For each probe energy, the input power going into the sample was adjusted to keep it constant at 150 μW. It was checked that the pump power used was also kept constant at 4.5 mW throughout the scans.This corresponds to a pump fluence on order of 6μJ/pulse/cm^2(10^{13}photons/pulse/cm^2) on the sample. It was verified that these experiments were conducted in the $\chi^{(3)}$ regime by checking that the nonlinear signal scaled linearly with the pump and probe powers. A double modulation scheme was used in the experiment to get rid of pump scatter on the detector, with the

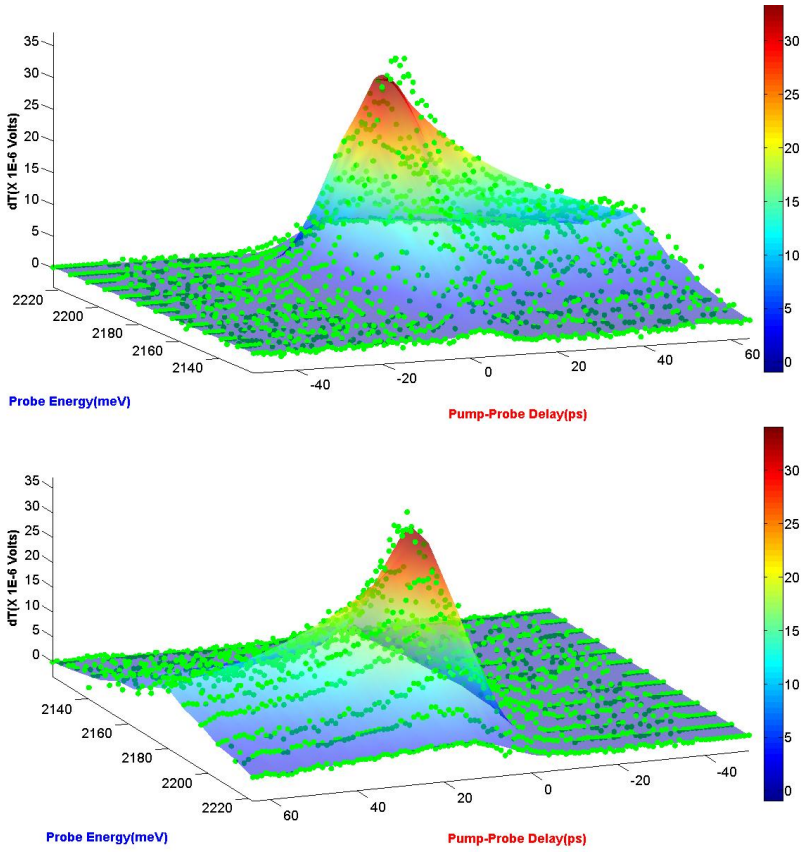

Figure 6.2: Two color dT data on SWCNTs: Alternate view angles for the plots in Figure(6.1).

pump modulated at about 6 kHz and the probe modulated at about 4 kHz using Acousto-Optic Modulators (AOM). The nonlinear signal was detected on a lockin at the difference frequency of about 2 kHz. We will present data in which the pump and probe beams are co-polarized. The position of zero delay and the instrument response function was recorded for each probe energy scan using the two photon signal obtained from a GaP photodiode as mentioned in Chapter(V).

6.1.1 Global Fit of Two Color dT Data

In Figures 6.1 and 6.2, we present the results of the two color data which are globally fitted using a computer program that has been developed in one of our collaborators, Prof Roseanne Sension's group. This fitting program uses the Simplex

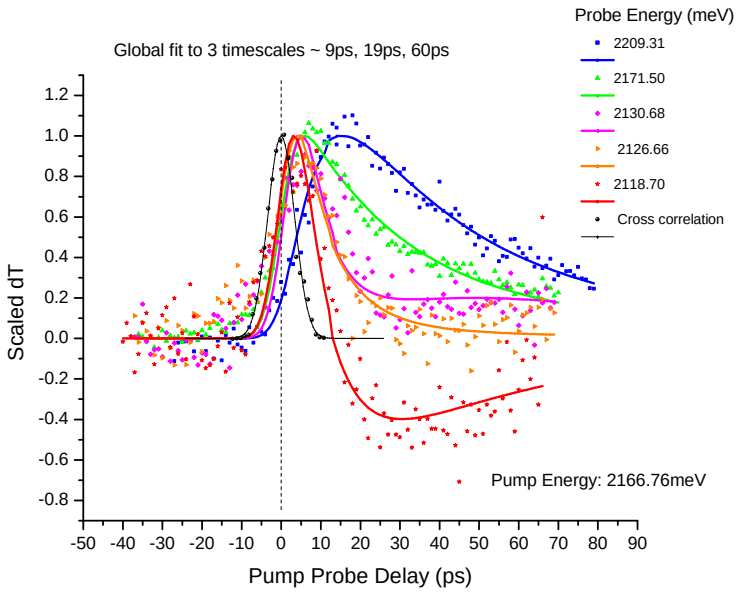

Figure 6.3: Scaled dT lineouts for a few probe energies.

algorithm (also known as the Nelder-Mead Method [36]) to fit the probe energy dependent decay scan data to common time exponentials in a global way: the time exponentials are treated as global variables between the different probe energy scans, and a fit is found for such common time exponentials, with only their prefactors varying with probe energy. We present scaled line-outs of the two color data in Figure (6.3).

If we examine the residue of the fits for the data shown in Figures 6.1 and 6.2, the residue does show some structure, so this fit is not perfect. However, we think the fit is good enough to allow us to look at the probe energy dependence of the prefactors and look for the signature signs of excitation induced resonant energy shifts, as described in Chapter(IV).

6.1.2 Probe Energy Dependent Prefactors: Decay Associated Spectra

The probe energy dependent prefactors obtained from the fits shown in Figures (6.1) and (6.2) is plotted in Figure(6.4). From the analysis carried out in Chapter

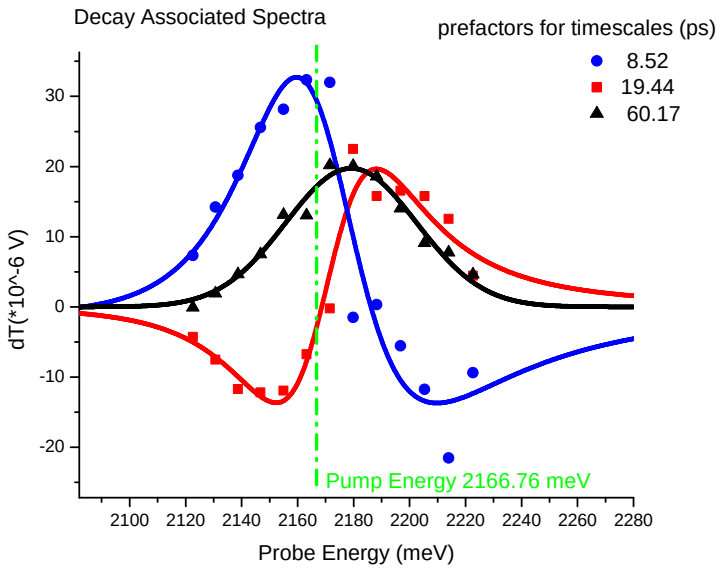

Figure 6.4: Decay Associated Spectra: The prefactors of the timescales obtained from the global fit are plotted as a function of probe energy. The derivative lineshape for the blue and red curves indicates a small change in the resonant energy of SWCNTs subsequent to optical excitation.

(IV), we expect that the prefactors can be fitted to a sum of lorentzians. The blue curve associated with the 8.5 ps timescale is fitted as a sum of two lorentzians: one is a positive lorentzian, and the other is a slightly blue-shifted negative lorentzian. The sum of these slightly energy-offset lorentzians has a characteristic derivative-type lineshape, and indicates an excitation induced shift of the transition for successive excitations. Similarly, the red curve associated with the 19.44 ps timescale is also fitted as a sum of two lorentzians: a positive lorentzian and the other being a slightly red-shifted lorentzian. In Figure(6.5), we plot out the decomposition of the prefactor fits. This figure serves to illustrate that the magnitude of the shifts of about 1 meV, is a tiny fraction of the the linewidth of the decomposed lorentzians which is about 35 meV. This serves to illustrate how time resolved nonlinear optical spectroscopy is such a powerful tool that enables the measurement of tiny time-dependent shifts in the resonant energy compared to the linewidth.

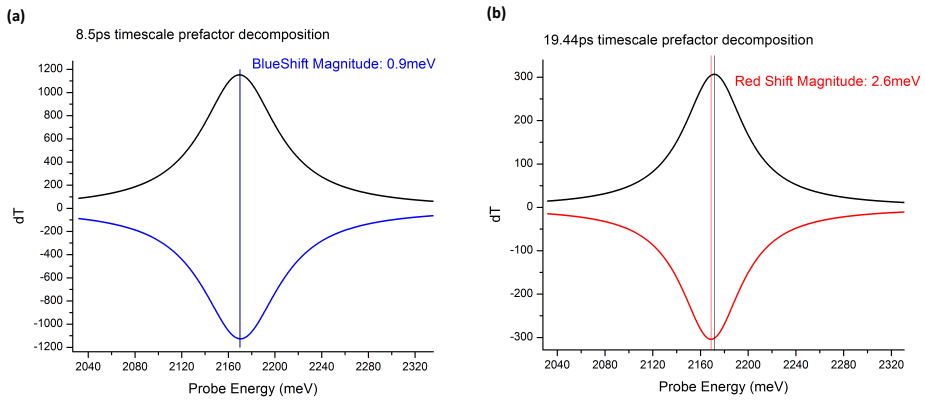

Figure 6.5: Decomposition of prefactors: The two lorentzians that need to be added to fit the prefactors for the timescales (a)8.5 ps (b)19.4 ps. The magnitude of the shift in energy resonance (1 meV) is a small fraction of the linewidth ($\sim$ 35 meV).

6.1.3 Ruling out Excited State Absorption

It should be noted that since the magnitude of the energy shift inferred from the global fits is extremely small, it is unlikely that the negative prefactors are due to further absorption from an excited state. For example, in linear absorption measurements[9, 17] the position of the E_{33} optical transition for the $(6, 5)$ chirality has been found to be at about 350 nm, corresponding to an energy separation of 3550 meV between the ground state and the E_{33} state. This makes the energy separation between the E_{11} and the E_{33} states to be 2300 meV, and the energy separation between the E_{22} and the E_{33} state to be 1400 meV. Similarly, the ground state to the E_{44} excited state energy[17, 55] has been measured to be 4100 meV in PLE. This again, gives the energy separation between the E_{11} and E_{44} states to be 2850 meV , and between the E_{22} and E_{44} states to be 1940 meV. Thus, the detuning of the lasers used in the experiment from the transition energy from either E_{11} or E_{22} to either E_{33} or E_{44} is atleast one order of magnitude bigger than the energy shift inferred from the fits. This gives us reason to believe that the 1 meV shift that our fits indicate cannot be due to such excited state absorption. Furthermore, since the

spectral shape of the negative peak is almost exactly that of the positive peak (with only a small frequency shift), we can also rule out the possibility that the negative peak is due to exciting the excitonic population to free carriers in the continuum that is observed at 4500 meV[8]. Also note that the energy separation between the E_{22} state and the continuum is 2340 meV, and this transition is also sufficiently detuned from our lasers. The fact that the spectral shapes of the two lorentzians that sum up in the fit are almost the same, the signs are different, and that one is just offset by the other by a small energy shift gives us reason to believe that this is a signature of an excitation induced resonant energy shift.

6.2 Energy Level Model of Two Color Data

In this section, we will use the intuition we have developed for simpler problems in Chapter(IV) to come up with an energy level diagram that is consistent with the wavelength dependent prefactors plotted in Figure(6.4). We are also going to keep in mind the microscopic model that was shown in Chapter (II) that predicts that excited state population in the E_{22} (E_{11}) state will drive a differential change in the diameter of the SWCNT that will shrink (expand) the tube in the radial dimension.

6.2.1 Configurational Diagrams and the Born-Oppenheimer Approximation

To gain some understanding of the physics behind the energy level diagram that we want to propose, first consider the configurational diagram in Figure(6.6). Let us consider that the SWCNT system starts in its ground state with an equilibrium diameter d_0. After two interactions with the pump pulse, an excited electronic state population is created in the E_{22} state. Note that due to the different equilibrium diameter of the SWCNT, in the ground state as compared to the E_{22} state, under the Born Oppenheimer approximation, initially an excited vibrational state is also

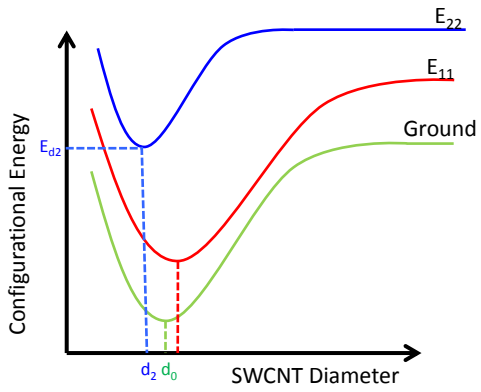

Figure 6.6: SWCNT diameter configuration diagram for excitonic population in the ground, E_{11} and E_{22} states.

created. This is because electronic transition happens on a much faster timescale than the nuclear motion of the lattice. Hence initially the electronic cloud is excited to the E_{22} state, but the configurational change to the shorter tube diameter would not happen as fast. The dynamics of the vibrational state is usually modeled by approximating the energy landscape around the energy minima as a parabolic energy potential [12]:

$$E(d - d_2) = E_{d_2} + \frac{1}{2} m^* \omega_{RBM} (d - d_2)^2$$

where E_{d_2} is the energy minimum that is associated with the E_{22} excited state. This is simply the potential energy of a harmonic oscillator, so the excited vibrational state will, by a physical analogy, correspond to the situation of an excited (compressed or extended) spring. This spring will now start oscillating at its own natural frequency, which for the kind of motion involved here will correspond to the Radial Breathing Mode (RBM) phonon mode frequency. This would physically cause the tube diameter to start oscillating. The oscillating tube diameter will lead to an oscillatory correction to the bandgap energy, and hence the transmission of a probe laser will also oscillate at the RBM frequency. These fast oscillations have been recently measured[25], and

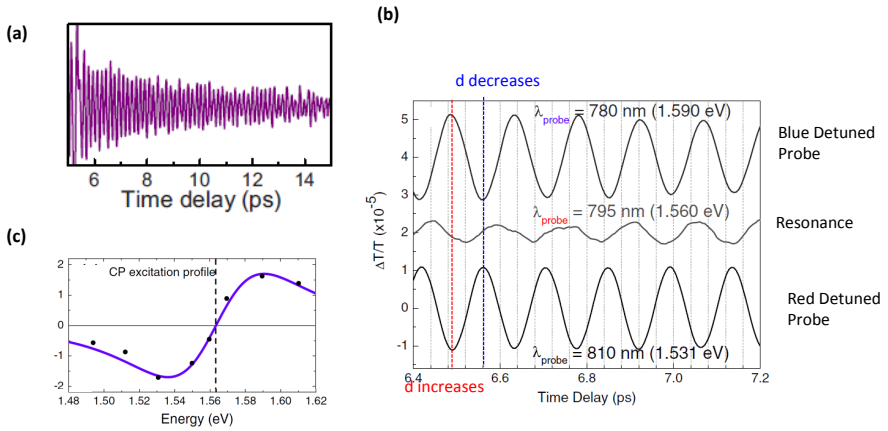

Figure 6.7: Femtosecond dT experimental results on SWCNT indicate oscillating SWCNT diameter.(a) The transmission of a probe laser oscillates at the the RBM mode frequency. (b) The wavelength dependence of the oscillation amplitude provides evidence that the oscillations imply that the bandgap energy itself is oscillating as explained in the text. (c)The coherent phonon oscillation amplitude is a derivative lineshape. Figure adapted from [25].

we reproduce data from their paper in Figure(6.7a). It is thought that these fast oscillations arise due to oscillation in the bandgap as a result of the oscillating SWCNT diameter and the the evidence for this is shown in Figure(6.7b).

The red vertical line in Figure(6.7 b) indicates a time point, where SWCNT diameter is expanding during the oscillation. Due to this expansion, the energy resonance is red shifted. This will reduce the transmission of a red detuned probe, and increase the transmission of a blue detuned probe. A similar explanation holds true for the blue vertical line. From this analysis, it can be understood that the amplitude of the coherent phonon oscillations will have a derivative lineshape as shown in Figure(6.7c). The coherent oscillation amplitude is zero close to resonance, and flips signs for blue-detuned and red-detuned probes.

These oscillations will get damped out, and on some timescale, the SWCNT diameter will reach the new equilibrium position. Due to a changed diameter, the bandgap energy will be slightly shifted, and hence there would be a change in the resonant

energy of successive excitation on the SWCNT. In the next section it will be shown how an energy level diagram of the two color experiment which incorporates such an energy shift on optical excitation will lead to the Decay Associated Spectrum plotted in Figure(6.4).

6.2.2 Proposed Energy Level Diagram

We will now propose an energy level diagram that, keeping the configurational energy diagrams of the previous section in minds, will give us a framework to explain our two color data. The ultimate goal is to numerically fit our data to this energy level model, to get more quantitatively accurate estimates of the spectral shift and the associated timescales. The purpose of this section is to obtain analytical expressions of the form that look like the Decay Associated Spectra curves shown in Figure (6.4). We will be assuming some of the relative decay rates and the branching ratios to get to these analytical expression, but it is only a full fit, and backing by a microscopic theory that can justify the assumptions made. In Figure(6.8a), the pump-probe configuration for two excitations on a SWCNT are shown. Figure(6.8b) shows the energy level diagram of these two excitations in a product Hilbert space , without taking the effect of any excitation induced spectral shifts.

The key to the model that will be presented is that we want to include exciton exciton interactions. Specifically, based on the earlier study discussed in Figure(6.7) and the microscopic models that have been proposed, we develop an energy level model assuming two interacting excitons. The model starts from a Hamiltonian that can be imagined to result from considering the effect of the first exciton on the energy level structure of it and the second exciton. We also assume that since the relaxation from the E_{22} state to the E_{11} state has been measured to be on order of 100 fs[30], which is at least an order of magnitude faster than our pulse-width, we will neglect the optical transitions from states $|2\rangle$ and $|2'\rangle$ to state $|3\rangle$. The physical reason for

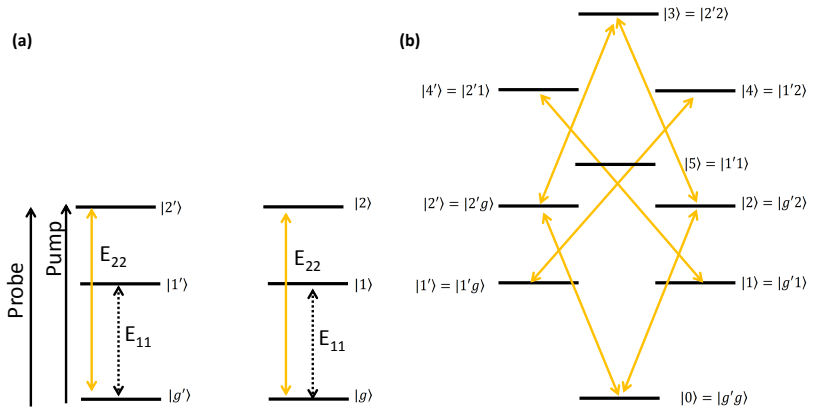

Figure 6.8: Energy Level Diagram for two excitations on a SWCNT. (a)The pump laser is parked close to the E_{22} transition, and the probe laser is scanned across this transition. (b) Two non-interacting excitations considered in a product Hilbert space.

this is that the extremely fast decay rate from state E_{22} to E_{11} implies that there is very little probability of exciting both the excitons to the E_{22} state. Now, a red-shift in the energy level diagram of Figure(6.8b) is incorporated that we speculate arises due to an expansion in the SWCNT diameter due to the presence of an exciton in the E_{11} level. The energy level diagram incorporating this energy shift is shown in Figure(6.9). In this diagram, the allowed optical transitions, following from the Born-Oppenheimer approximation are also shown. The orange arrows in Figure(6.9) denotes transitions that are at an energy separation ω_0, which we assume to be the ground state to E_{22} energy of the unaltered transition. The red arrows in Figure(6.9) denote transitions which are separated in energy by a value $\omega_0 - \Delta E$, where ΔE is the shift in the resonant energy. The detunings for the probe laser can be defined as follows:

$$\delta_{pr} = \omega_0 - \omega_{pr} \tag{6.1}$$

$$\delta'_{pr} = \omega_0 - \Delta E - \omega_{pr} = \delta_{pr} - \Delta E \tag{6.2}$$

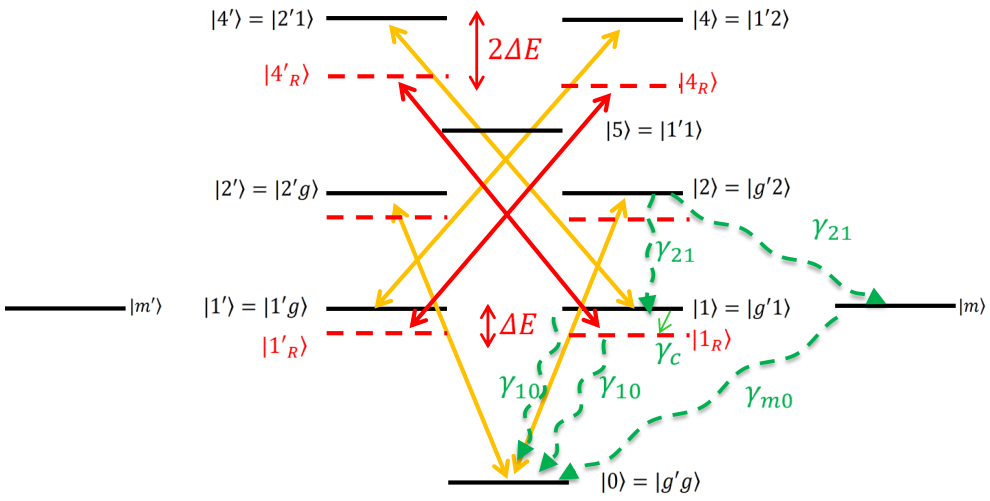

Figure 6.9: Modification of the energy level diagram due to the interactions between the two excitons.

To get an analytical form of the solution, a particular decay scheme is assumed, which is shown in Figure(6.9). There are some assumptions that have been made in this decay scheme: It is assumed that the decay rates from the the levels $|1\rangle$ and $|1_R\rangle$ back to the ground state are equal and given by γ_{10}. Further, it is assumed that there is a decay path from state $|1\rangle$ to state $|1_R\rangle$ denoted by a decay rate of γ_c. This decay represents the configurational change to a larger SWCNT diameter due to an exciton in the E_{11} state. In Figure(6.9) there also is a state denoted by $|m\rangle$ which represents a longer-lived metastable state where some excited state population can get trapped. Such states are thought to occur due to defects and impurities in surfactant wrapped SWCNT samples and are thought to be responsible for the non-unity photoluminescence quantum yield[51]. The equations of motion of the density matrix elements following this decay scheme are given by

$$\begin{aligned}
\dot{\rho}^I_{20} &= i\left(\chi_{pu}e^{i\delta_{pu}t+ik_{pu}r}+\chi_{pr}e^{i\delta_{pr}t+ik_{pr}r}\right)(\rho_{22}-\rho_{00})-\gamma\rho^I_{20} \\
\dot{\rho}^I_{4'1} &= i\left(\chi_{pu}e^{i\delta_{pu}t+ik_{pu}r}+\chi_{pr}e^{i\delta_{pr}t+ik_{pr}r}\right)(\rho_{4'4'}-\rho_{11})-\gamma\rho^I_{4'1}
\end{aligned}$$

$$
\begin{aligned}
\dot{\rho}^I_{4'_R1_R} &= i\left(\chi_{pu}e^{i\delta'_{pu}t+ik_{pu}r}+\chi_{pr}e^{i\delta'_{pr}t+ik_{pr}r}\right)\left(\rho_{4'_R4'_R}-\rho_{1_R1_R}\right)-\gamma\rho^I_{4'_R1_R}\\
\dot{\rho}^I_{2'0} &= i\left(\chi_{pu}e^{i\delta_{pu}t+ik_{pu}r}+\chi_{pr}e^{i\delta_{pr}t+ik_{pr}r}\right)\left(\rho_{2'2'}-\rho_{00}\right)-\gamma\rho^I_{2'0}\\
\dot{\rho}^I_{41'} &= i\left(\chi_{pu}e^{i\delta_{pu}t+ik_{pu}r}+\chi_{pr}e^{i\delta_{pr}t+ik_{pr}r}\right)\left(\rho_{44}-\rho_{1'1'}\right)-\gamma\rho^I_{41'}\\
\dot{\rho}^I_{4_R1'_R} &= i\left(\chi_{pu}e^{i\delta'_{pu}t+ik_{pu}r}+\chi_{pr}e^{i\delta'_{pr}t+ik_{pr}r}\right)\left(\rho_{4_R4_R}-\rho_{1'_R1'_R}\right)-\gamma\rho^I_{4_R1'_R}\\
\dot{\rho}_{22} &= i\left(\chi^*_{pu}e^{-i\delta_{pu}t-ik_{pu}r}+\chi^*_{pr}e^{-i\delta_{pr}t-ik_{pr}r}\right)\left(\rho^I_{20}\right)\\
&\quad -i\left(\chi_{pu}e^{i\delta_{pu}t+ik_{pu}r}+\chi_{pr}e^{i\delta_{pr}t+ik_{pr}r}\right)\left(\rho^I_{02}\right)-2\gamma_{21}\rho_{22}\\
\dot{\rho}_{11} &= i\left(\chi^*_{pu}e^{-i\delta_{pu}t-ik_{pu}r}+\chi^*_{pr}e^{-i\delta_{pr}t-ik_{pr}r}\right)\left(-\rho^I_{4'1}\right)\\
&\quad -i\left(\chi_{pu}e^{i\delta_{pu}t+ik_{pu}r}+\chi_{pr}e^{i\delta_{pr}t+ik_{pr}r}\right)\left(-\rho^I_{14'}\right)\\
&\quad +\gamma_{21}\rho_{22}-\gamma_c\rho_{11}-\gamma_{10}\rho_{11}\\
\dot{\rho}_{1_R1_R} &= i\left(\chi^*_{pu}e^{-i\delta'_{pu}t-ik_{pu}r}+\chi^*_{pr}e^{-i\delta'_{pr}t-ik_{pr}r}\right)\left(-\rho^I_{4'_R1_R}\right)\\
&\quad -i\left(\chi_{pu}e^{i\delta'_{pu}t+ik_{pu}r}+\chi_{pr}e^{i\delta'_{pr}t+ik_{pr}r}\right)\left(-\rho^I_{1_R4'_R}\right)\\
&\quad +\gamma_c\rho_{11}-\gamma_{10}\rho_{1_R1_R}\\
\dot{\rho}_{2'2'} &= i\left(\chi^*_{pu}e^{-i\delta_{pu}t-ik_{pu}r}+\chi^*_{pr}e^{-i\delta_{pr}t-ik_{pr}r}\right)\left(\rho^I_{2'0}\right)\\
&\quad -i\left(\chi_{pu}e^{i\delta_{pu}t+ik_{pu}r}+\chi_{pr}e^{i\delta_{pr}t+ik_{pr}r}\right)\left(\rho^I_{02'}\right)-2\gamma_{21}\rho_{2'2'}\\
\dot{\rho}_{1'1'} &= i\left(\chi^*_{pu}e^{-i\delta_{pu}t-ik_{pu}r}+\chi^*_{pr}e^{-i\delta_{pr}t-ik_{pr}r}\right)\left(-\rho^I_{41'}\right)\\
&\quad -i\left(\chi_{pu}e^{i\delta_{pu}t+ik_{pu}r}+\chi_{pr}e^{i\delta_{pr}t+ik_{pr}r}\right)\left(-\rho^I_{1'4}\right)\\
&\quad +\gamma_{21}\rho_{2'2'}-\gamma_c\rho_{1'1'}-\gamma_{10}\rho_{1'1'}\\
\dot{\rho}_{1'_R1'_R} &= i\left(\chi^*_{pu}e^{-i\delta'_{pu}t-ik_{pu}r}+\chi^*_{pr}e^{-i\delta'_{pr}t-ik_{pr}r}\right)\left(-\rho^I_{4_R1'_R}\right)\\
&\quad -i\left(\chi_{pu}e^{i\delta'_{pu}t+ik_{pu}r}+\chi_{pr}e^{i\delta'_{pr}t+ik_{pr}r}\right)\left(-\rho^I_{1'_R4_R}\right)\\
&\quad +\gamma_c\rho_{1'1'}-\gamma_{10}\rho_{1'_R1'_R}\\
\dot{\rho}_{mm} &= \gamma_{21}\rho_{22}-\gamma_{m0}\rho_{mm}\\
\dot{\rho}_{m'm'} &= \gamma_{21}\rho_{2'2'}-\gamma_{m0}\rho_{m'm'}
\end{aligned}
$$

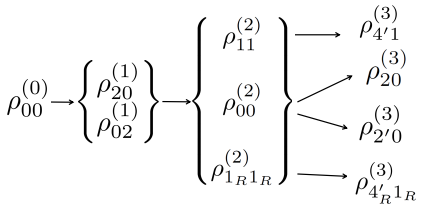

Figure 6.10: Perturbation sequences arising from the right part of the energy level diagram.

$$
\begin{aligned}
\dot{\rho}_{00} &= i\left(\chi_{pu}^{*}e^{-i\delta_{pu}t-ik_{pu}r}+\chi_{pr}^{*}e^{-i\delta_{pr}t-ik_{pr}r}\right)\left(-\rho_{20}^{I}\right)\\
&\quad -i\left(\chi_{pu}e^{i\delta_{pu}t+ik_{pu}r}+\chi_{pr}e^{i\delta_{pr}t+ik_{pr}r}\right)\left(-\rho_{02}^{I}\right)\\
&\quad +i\left(\chi_{pu}^{*}e^{-i\delta_{pu}t-ik_{pu}r}+\chi_{pr}^{*}e^{-i\delta_{pr}t-ik_{pr}r}\right)\left(-\rho_{2'0}^{I}\right)\\
&\quad -i\left(\chi_{pu}e^{i\delta_{pu}t+ik_{pu}r}+\chi_{pr}e^{i\delta_{pr}t+ik_{pr}r}\right)\left(-\rho_{02'}^{I}\right)\\
&\quad +\gamma_{10}\left(\rho_{11}+\rho_{1'1'}\right)+\gamma_{10}\left(\rho_{1_R1_R}+\rho_{1'_R1'_R}\right)\\
&\quad +\gamma_{m0}\left(\rho_{mm}+\rho_{m'm'}\right)
\end{aligned}
$$

The perturbation sequences arising from the right part of the energy level diagram leading to the nonlinear signal are shown in Figure(6.10). There is another symmetric perturbation sequence arising from the left part of energy level diagram which will only contribute a factor of two.

First Order

To the first order in the pump field the following expression for the coherences are obtained

$$\rho_{20}^{I(1)}=\frac{-i\chi_{pu}}{\gamma+i\delta_{pu}}e^{i\delta_{pu}t+ik_{pu}r}$$

The complex conjugate is

$$\rho_{02}^{I(1)} = \frac{i\chi_{pu}^*}{\gamma - i\delta_{pu}} e^{-i\delta_{pu}t - ik_{pu}r}$$

Second Order

To the second order in the pump field it is obtained

$$\dot{\rho}_{22}^{(2)} = i\left(\chi_{pu}^* e^{-i\delta_{pu}t - ik_{pu}r}\right)\left(\rho_{20}^{I(1)}\right) - i\left(\chi_{pu} e^{i\delta_{pu}t + ik_{pu}r}\right)\left(\rho_{02}^{I(1)}\right) - 2\gamma_{21}\rho_{22}^{(2)}$$

Solving this for delta function pulse gives us:

$$\rho_{22}^{(2)} = K_0 e^{-2\gamma_{21}t} \tag{6.3}$$

where

$$K_0 = \frac{2\gamma\left|\chi_{pu}\right|^2}{\gamma^2 + \delta_{pu}^2}$$

For population in the $|1\rangle$ state, the following equation is solved

$$\dot{\rho}_{11}^{(2)} = \gamma_{21}\rho_{22}^{(2)} - \left(\gamma_c + \gamma_{10}\right)\rho_{11}^{(2)}$$

This equation can be solved by putting in the value of $\rho_{22}^{(2)}$ and using integrating factor $e^{(\gamma_c+\gamma_{10})t}$. This obtains

$$\rho_{11}^{(2)} = \frac{\gamma_{21}}{2\gamma_{21} - \gamma_{10} - \gamma_c} K_0\left(e^{-(\gamma_c+\gamma_{10})t} - e^{-2\gamma_{21}t}\right) \tag{6.4}$$

To simplify the maths from hereon, since the decay rate γ_{21} has been measured to be very fast, the term $e^{-\gamma_{21}t}$ will be dropped. Hence Equation(6.4) can be simplified to obtain

$$\rho_{11}^{(2)} \approx \frac{1}{2} K_0 e^{-(\gamma_c+\gamma_{10})t} \tag{6.5}$$

For population in the $|1_R\rangle$ state, the following equation needs to be solved

$$\dot{\rho}_{1_R 1_R}^{(2)} = \gamma_c \rho_{11}^{(2)} - \gamma_{10} \rho_{1_R 1_R}^{(2)}$$

This equation can be solved by putting in the value of $\rho_{11}^{(2)}$ from Equation(6.5) and using integrating factor $e^{\gamma_{10}t}$. This obtains

$$\rho_{1_R 1_R}^{(2)} = \frac{1}{2} K_0 \left(e^{-\gamma_{10}t} - e^{-(\gamma_c+\gamma_{10})t} \right) \tag{6.6}$$

Population in the $|m\rangle$ state can be obtained to be:

$$\rho_{mm}^{(2)} \approx \frac{1}{2} K_0 e^{-\gamma_{m0}t} \tag{6.7}$$

From population conservation considerations, the population in the ground state is

$$\begin{aligned} \rho_{00}^{(2)} &= -\left(\frac{1}{2} K_0 e^{-(\gamma_c+\gamma_{10})t} + \frac{1}{2} K_0 \left(e^{-\gamma_{10}t} - e^{-(\gamma_c+\gamma_{10})t} \right) + \frac{1}{2} K_0 e^{-\gamma_{m0}t} \right) \\ \rho_{00}^{(2)} &= -\frac{1}{2} K_0 e^{-\gamma_{10}t} - \frac{1}{2} K_0 e^{-\gamma_{m0}t} \end{aligned} \tag{6.8}$$

To summarize the calculations of this section, the populations to the second order in the pump field given by Equations (6.5,6.6,6.7,6.8) are written below

$$
\begin{aligned}
\rho_{22}^{(2)} &\approx 0 \\
\rho_{mm}^{(2)} &\approx \frac{1}{2}K_0 e^{-\gamma_m t} \\
\rho_{11}^{(2)} &\approx \frac{1}{2}K_0 e^{-(\gamma_c+\gamma_{10})t} \\
\rho_{1_R 1_R}^{(2)} &\approx \frac{1}{2}K_0 \left(e^{-\gamma_{10}t} - e^{-(\gamma_c+\gamma_{10})t}\right) \\
\rho_{00}^{(2)} &\approx -\frac{1}{2}K_0 e^{-\gamma_{10}t} - \frac{1}{2}K_0 e^{-\gamma_{m0}t}
\end{aligned}
$$

Third Order

The perturbation sequences that contribute are shown in Figure(6.10). There is another set of symmetric perturbation sequences for the left part of the energy level diagram, that will just contribute a factor of two. The following values are obtained for the coherences to the third order in the Schrödinger picture:

$$
\begin{aligned}
\rho_{20}^{(3)} &= \frac{i\chi_{pr}}{\gamma + i\delta_{pr}} \left(\frac{1}{2}K_0 e^{-\gamma_{10}t} + \frac{1}{2}K_0 e^{-\gamma_{m0}t}\right) e^{-i\omega_{pr}t + ik_{pr}r} \\
\rho_{2'0}^{(3)} &= \frac{i\chi_{pr}}{\gamma + i\delta_{pr}} \left(\frac{1}{2}K_0 e^{-\gamma_{10}t} + \frac{1}{2}K_0 e^{-\gamma_{m0}t}\right) e^{-i\omega_{pr}t + ik_{pr}r} \\
\rho_{4'1}^{(3)} &= \frac{i\chi_{pr}}{\gamma + i\delta_{pr}} \left(-\frac{1}{2}K_0 e^{-(\gamma_c+\gamma_{10})t}\right) e^{-i\omega_{pr}t + ik_{pr}r} \\
\rho_{4'_R 1_R}^{(3)} &= \frac{i\chi_{pr}}{\gamma + i\delta'_{pr}} \left(-\frac{1}{2}K_0 e^{-\gamma_{10}t} + \frac{1}{2}K_0 e^{-(\gamma_c+\gamma_{10})t}\right) e^{-i\omega_{pr}t + ik_{pr}r}
\end{aligned}
$$

Now the expression for the nonlinear polarization can be obtained by using the relation $P^{(3)} = \mathrm{Tr}\left(\mu\rho^{(3)}\right)$. In the expression of the nonlinear polarization, the prefactor for $e^{-(\gamma_c+\gamma_{10})t}$ is given by

$$
\frac{1}{2}K_0 \left(-\frac{1}{\gamma + i\delta_{pr}} + \frac{1}{\gamma + i\delta'_{pr}}\right) \tag{6.9}
$$

Similarly, the prefactor for $e^{-\gamma_{10}t}$ in the nonlinear polarization is given by

$$\frac{1}{2}K_0\left(\frac{2}{\gamma+i\delta_{pr}}-\frac{1}{\gamma+i\delta'_{pr}}\right) \tag{6.10}$$

Finally, the prefactor for $e^{-\gamma_{m0}t}$ can be written as

$$\frac{1}{2}K_0\left(\frac{2}{\gamma+i\delta_{pr}}\right) \tag{6.11}$$

The expression of the obtained homodyne detected dT signal can be obtained by using Equations (6.1) and (6.2) for the detunings:

$$\begin{aligned}\mathrm{dT} \;\propto\; & \left(\frac{1}{\gamma^2+(\omega_0-\Delta E-\omega_{pr})^2}-\frac{1}{\gamma^2+(\omega_0-\omega_{pr})^2}\right)e^{-(\gamma_c+\gamma_{10})t}\\ +\; & \left(\frac{2}{\gamma^2+(\omega_0-\omega_{pr})^2}-\frac{1}{\gamma^2+(\omega_0-\Delta E-\omega_{pr})^2}\right)e^{-\gamma_{10}t}\\ & +\left(\frac{2}{\gamma+i\delta_{pr}}\right)e^{-\gamma_{m0}t}\end{aligned} \tag{6.12}$$

From Equation(6.12), it can be noted that the spectral shape of the prefactor of the $e^{-\gamma_{m0}t}$ term bears similarity to the experimentally measured spectra for the 60.1 ps timescale in Figure(6.4). Thus we assign the value of $1/\left(60.1\,\mathrm{ps}\right)$ to the parameter γ_{m0} in the model proposed above. The prefactor for $e^{-(\gamma_c+\gamma_{10})t}$ in the expression of the dT signal given by Equation(6.12) is simulated in Figure(6.11) for the parameters shown in the figure caption. By comparing the spectra in Figure(6.11) to the experimentally measured DAS in Figure(6.4), we find similarity between the calculated prefactor for $e^{-(\gamma_c+\gamma_{10})t}$ and the spectra for the 8.5 ps timescale. Thus we assign the value of $1/\left(8.5\,\mathrm{ps}\right)$ to $(\gamma_c+\gamma_{10})$ in the proposed model. The spectral shape of the prefactor for the term $e^{-\gamma_{10}t}$ is predicted to be asymmetric according to Equation(6.12). However, the spectral curve for the 19.4 ps timescale in Figure(6.11) is more derivative-like. If

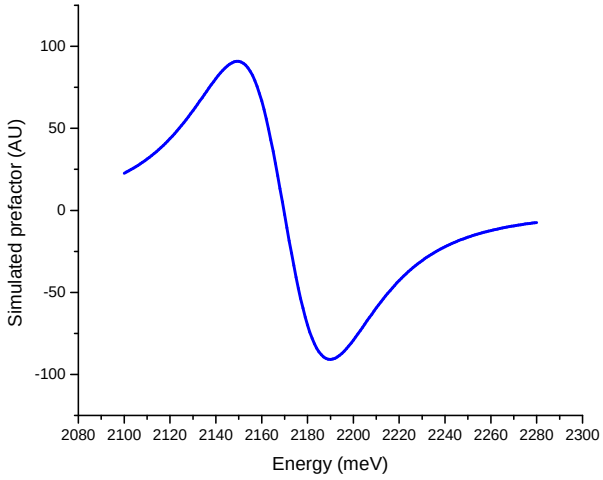

Figure 6.11: Simulated prefactor of the term $e^{-(\gamma_c+\gamma_{10})t}$ in Equation(6.12). The simulation parameters are $\omega_0 = 2170\,\text{meV}$, $\gamma = 35\,\text{meV}$, $\Delta E = 1\,\text{meV}$. The derivative lineshape indicates an excitation induced resonance energy shift.

we tentatively assign the value of $1/\,(19.4\,\text{ps})$ to γ_{10}, then we obtain the value of γ_c to be $1/\,(15.1\,\text{ps})$ in the model. It can be noted that the spectral shape of the prefactor for the term $e^{-\gamma_{10}t}$ would have been derivative like, if not for the factor of 2 in the first term of the prefactor. This discrepancy between the proposed model and the experimental DAS is still under study.

6.3 Chapter Summary

In this chapter we have shown the data obtained from two color dT experiments on SWCNTs. A global fit to the the two color data was carried out, that enabled the extraction of three timescales of 8.5, 19.4 and 60.1 ps which fit the various probe energy decay scans, with the prefactors of the three timescales depending on the probe energy. The prefactors were plotted out as a function of the probe energy, and lead to the Decay Associated Spectra (DAS) for the SWCNT sample. The derivative-like features observed in the DAS indicate a change in the resonance energy of the

SWCNTs upon optical excitation. The spectra associated with the 8.5 and 19.4 ps timescales were fitted to the difference of two lorentzians. The magnitude of the shift was obtained from the difference in the center frequencies of the two lorentzians to be on order of 1 meV, which is a small fraction of the linewidths of about 35 meV. An energy level diagram was proposed that incorporated the results of theoretical calculations from which it is inferred that a blue (red) shift occurs in the transition energies of successive excitations on the SWCNT due to excited state population in the $E_{22}(E_{11})$ state. The nonlinear signal arising from this energy level diagram was perturbatively solved to the the third order in the fields to show analytical forms of some of the prefactors, which bear similarity to the experimental prefactors in the DAS. Some of the differences between the proposed model and the experimental results were also pointed out, and it was noted that further studies are needed to analyze the reason behind these differences.

CHAPTER VII

Summary and Future Work

This chapter summarizes the results of this dissertation. Further experiments that can test out the main hypothesis used for explaining the experimental data are proposed. The implication of the effects that have been measured are discussed for device geometries where SWCNTs are coupled to cavities. The possibility of coherently controlling and optically harnessing the motion of the lattice is discussed briefly.

7.1 Summary of the Results

This dissertation has studied the interaction of resonant narrow-band picosecond lasers with samples enriched in the $(6, 5)$ chirality SWCNTs. The experimental emphasis has especially been on detecting optical excitation induced changes in the resonant energy of SWCNTs. Such changes are inferred from theoretical calculations in the literature that point to a distortion of the SWCNT lattice in the radial direction due to optical excitation. The signature signs of such an excitation induced change in the resonant energy was derived in this dissertation by perturbatively calculating the analytical form of the time resolved, homodyne detected, third order nonlinear response of such a system. Two color differential transmission experiments were conducted, in which the pump energy is fixed, and the probe energies are swept

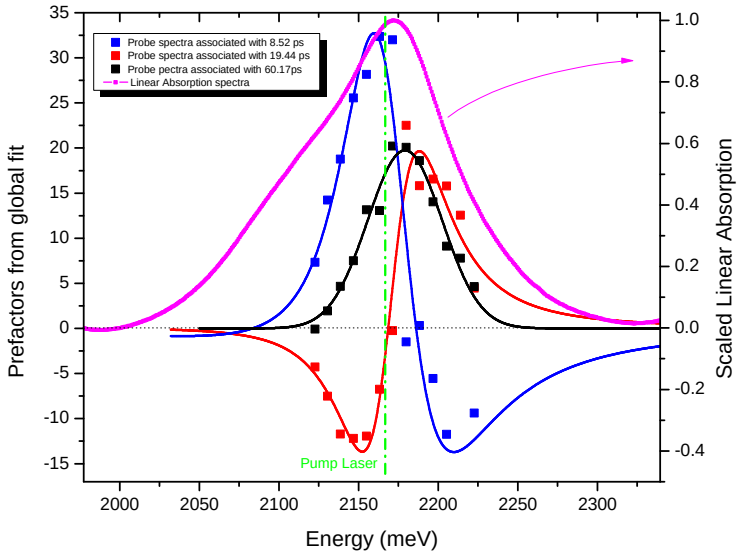

Figure 7.1: The scaled linear absorption is plotted along with the decay associated spectra obtained from the nonlinear measurement.

across the E_{22} transitions which yield decay scans for each probe energy. This dataset is globally fitted to extract prefactors for common time exponentials, from which a decay associated spectra (DAS) is plotted. The DAS shown in Figure(6.4) is plotted again in Figure(7.1), along with the scaled version of the linear absorption of the sample. Figure(7.1) serves to illustrate the utility of the narrowband lasers employed in the study. The linewidths of the nonlinear spectra are smaller than the linewidth of the linear absorption, which indicates that there is inhomogeneous broadening in the sample. The pump pulse is able to selectively excite the resonant excitations on the SWCNTS, and the probe spectra shows derivative-like lineshapes which was shown to arise in a model that incorporates excitation induced shifts in the resonant energy.

7.2 Further Experiments to Test the Hypothesis

In this section, further experiments will be described that can test the hypothesis of explaining the measured DAS on the basis of excitation induced structural changes

in SWCNTs, leading to a shift in the resonant energy for successive excitations. It can be noted from Figure(7.1), that it might be desirable to extend the wavelength range of the probe spectra scans to ascertain if the data points would follow the fits further away from the pump laser. For the optical setup used in this work, this was not possible as it would have required changing laser optics and the gain medium. It would also be interesting to see what the data would look like for an experimental setup similar to the two color differential transmission setup used in this dissertation, but with the lasers resonant with the E_{11} transition. This experimental configuration should limit optically exciting population to just the E_{11} state. From the energy level diagram proposed in Section(6.2.2), it might be expected that only one of the extracted prefactors from the global fit to such data should have a derivative-looking lineshape corresponding to an expansion in the SWCNT diameter due to excitonic population in the E_{11} state. Another interesting test of the results described in this dissertation would be to use SWCNTs belonging to a different chirality for similar experiments. It was seen in Section (2.3), that the microscopic condensed matter theory predicts a sign reversal in the electron-phonon matrix element for SWCNTs belonging to the mod(1) and mod(2) families. The experiments conducted in this dissertation were on a sample enriched in the $(6, 5)$ chirality, which belongs to the mod(1) family. If similar dT experiments on SWCNTs belonging to the mod(2) family give the result predicted according to the hypothesis in this dissertation, this would bolster the argument for this hypothesis.

7.3 Implication to Cavity Based SWCNT Devices

The hypothesis laid out in this dissertation suggests, that the resonant energy for exciting multiple excitons on a SWCNTs changes. From the decomposition of the prefactor fits carried shown in Figure(6.5), it was seen that this shift was small compared to the linewidth. This could still have implications for device geometries

involving SWCNTs where a high excited population is desired. The development of active SWCNT based photonic devices would involve interfacing SWCNTs with cavities. Luminescence has already been shown to occur in SWCNTs excited by electrical means, and an electrically-pumped nanolaser compatible with Si will greatly aid the field of silicon photonics. A necessary condition for achieving optical amplification would be to have sufficient population inversion. If the resonant energy of the SWCNTs undergoes a change for population in the ground state, compared to the population in the excited state then this might create hurdles in coupling to the cavity, but a more detailed study is called for.

7.4 Coherent Control of Vibrational States in SWCNTs

The possibility of optically inducing structural changes in SWCNTs opens up the doors to optical means of coherently controlling the motion of the lattice. Some of this has already been achieved in the literature. The coherent phonon oscillations shown in Figure(6.7) can be greatly amplified by pulse shaping techniques. In such studies, instead of a single pump pulse, a train of pulses is used, with the repetition rate of the train of pulses equal to the the radial breathing mode (RBM) frequency[25], which depends on the chirality but is in the ballpark of 10 THz. This coherently drives the SWCNT tube diameter oscillations to large amplitudes. It is interesting to note how by modifying the repetition rate, the diameter oscillations of a particular chirality can be driven to large amplitudes. This scheme achieves chirality selectivity in an inhomogeneous sample even though broadband femtosecond pulses are used[25]. Molecular dynamic simulations have also studied the possibility of irreversible structural changes induced on the SWCNTs[23], for example, by opening the end caps[10, 11]. It can be envisioned that such excited state reactions might have technological importance by optically creating structures where the SWCNTs can be filled with smaller molecular species.

7.5 Conclusion

In this dissertation, experimental investigation of resonant light with SWCNTs was carried out. The data gathered from two color differential transmission experiments, conducted with narrow-band picosecond pulses, was explained by a model that incorporates excitation induced resonant energy shifts. Such excitation induced shifts in the resonant energy were sought to be explained in the context of theoretical calculations that predict structural distortion of SWCNTs subsequent to optical excitation, that results from strong exciton-phonon coupling in this system. It is inferred that such structural changes in the SWCNT lead to a shift in the resonant energy for successive excitations on the SWCNTs which was sought to be measured using techniques of time resolved nonlinear optical spectroscopy. Further experiments that could test the main hypothesis in this thesis were proposed, and the implication of the results of this thesis to certain applications were discussed.

APPENDIX

APPENDIX A

Wavelength Dependent Offset in dT Signals

A wavelength dependent offset has been subtracted out of all differential transmission (dT) signals shown in Chapters (V) and (VI). This offset is due to a non-zero dT signal before zero delay between the pump and probe beams. The repetition rate of the lasers used in the experiments is 76 MHz, which corresponds to a time interval between two successive pulses to be 13 ns. Hence, a non-zero offset implies a physical mechanism due to which there is a change in transmission of the probe pulse over a timescale greater than 13 ns after the pump pulse. This wavelength dependent offset is plotted in Figure(A.1) along with the linear absorption peak of the sample. It is observed that the offset signal is red-shifted compared to the the linear absorption signal.

Some reasons that could be responsible for the longer timescale dT signal represented by the offset are briefly discussed below.

1. Trapping of population in metastable states: Previous studies have[51] also reported dT studies, where the signal does not reduce to zero over long timescales. This has been attributed to the presence of long-lived states that trap the optically excited population, and prevent a full recovery of the ground state population[7]. It is thought that the presence of defects and impurities in the

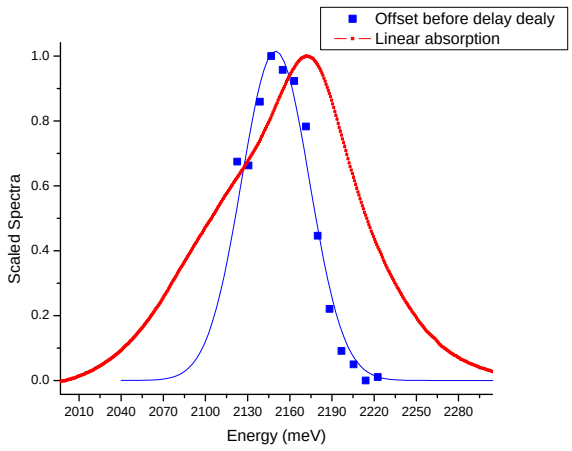

Figure A.1: Scaled spectra of the dT signal before zero delay, plotted along with the linear absorption of the sample.

SWCNT samples can lead to such long-lived states. The low photoluminescence quantum yield of surfactant encapsulated SWCNT is also attributed to such metastable states.

2. Thermal effects: Thermal heating of the sample by the pump pulse can also lead to a longer timescale dT signal. Here, two mechanisms due to thermal effects will be briefly discussed.

   (a) In the first mechanism, thermal lensing in the SWCNT solution sample can occur due to the pump pulse. In pump probe experiments, it is quite common to have an iris after the sample to spatially block out the pump. Due to the thermal lensing effect, the transmission of the probe pulse through this aperture after the sample can change[49]. This effect was observed in the experiments discussed in this dissertation: by opening and closing an iris in the probe path after the sample, the value of dT/T was seen to change. To minimize this effect, care was taken not to have apertures in the path of the probe beam after the sample, and a double modulation scheme was preferred to get rid of the pump scatter on the

detector.

(b) In the second mechanism, the Fresnel reflection and transmission coefficients for the SWCNT sample can change due to heating caused by the pump pulse, thereby causing a long timescale dT signal.

BIBLIOGRAPHY

BIBLIOGRAPHY

[1] Avouris, P. (2009), Carbon nanotube electronics and photonics, *Physics Today*, *62*(1), 34, doi:10.1063/1.3074261.

[2] Avouris, P., M. Freitag, and V. Perebeinos (2008), Carbon-nanotube photonics and optoelectronics, *Nat Photon*, *2*(6), 341–350, doi:10.1038/nphoton.2008.94.

[3] Bachilo, S. M., M. S. Strano, C. Kittrell, R. H. Hauge, R. E. Smalley, and R. B. Weisman (2002), Structure-assigned optical spectra of single-walled carbon nanotubes, *Science*, *298*(5602), 2361–2366, doi:10.1126/science.1078727.

[4] Bao, Q., H. Zhang, B. Wang, Z. Ni, C. H. Y. X. Lim, Y. Wang, D. Y. Tang, and K. P. Loh (2011), Broadband graphene polarizer, *Nat Photon*, *5*(7), 411–415, doi:10.1038/nphoton.2011.102.

[5] Berman, P. R., and V. S. Malinovsky (2010), *Principles of Laser Spectroscopy and Quantum Optics*, Princeton University Press.

[6] Boyd, R. W. (2003), *Nonlinear Optics, Second Edition*, 2 ed., Academic Press.

[7] Comfort, E. S., D. A. Jones, A. Malapanis, Z. R. Robinson, M. T. Fishman, and J. U. Lee (2011), Spectroscopy of strongly localized excitons and band-gap states in semiconducting single-walled carbon nanotubes, *Physical Review B*, *83*(8), 081,401, doi:10.1103/PhysRevB.83.081401.

[8] Crochet, J. J., S. Hoseinkhani, L. Lüer, T. Hertel, S. K. Doorn, and G. Lanzani (2011), Free-carrier generation in aggregates of single-wall carbon nanotubes by photoexcitation in the ultraviolet regime, *Physical Review Letters*, *107*(25), 257,402, doi:10.1103/PhysRevLett.107.257402.

[9] Dukovic, G., M. Balaz, P. Doak, N. D. Berova, M. Zheng, R. S. Mclean, and L. E. Brus (2006), Racemic single-walled carbon nanotubes exhibit circular dichroism when wrapped with DNA, *Journal of the American Chemical Society*, *128*(28), 9004–9005, doi:10.1021/ja062095w.

[10] Dumitrică, T., M. E. Garcia, H. O. Jeschke, and B. I. Yakobson (2004), Selective cap opening in carbon nanotubes driven by laser-induced coherent phonons, *Physical Review Letters*, *92*(11), 117,401, doi:10.1103/PhysRevLett.92.117401.

[11] Dumitrică, T., M. E. Garcia, H. O. Jeschke, and B. I. Yakobson (2006), Breathing coherent phonons and caps fragmentation in carbon nanotubes following ultrafast laser pulses, *Physical Review B*, *74*(19), 193,406, doi: 10.1103/PhysRevB.74.193406.

[12] Fox, M. (2002), *Optical Properties of Solids*, 1 ed., Oxford University Press, USA.

[13] Freitag, M., J. Chen, J. Tersoff, J. C. Tsang, Q. Fu, J. Liu, and P. Avouris (2004), Mobile ambipolar domain in carbon-nanotube infrared emitters, *Physical Review Letters*, *93*(7), 076,803, doi:10.1103/PhysRevLett.93.076803.

[14] Gabor, N. M., Z. Zhong, K. Bosnick, J. Park, and P. L. McEuen (2009), Extremely efficient multiple electron-hole pair generation in carbon nanotube photodiodes, *Science*, *325*(5946), 1367–1371, doi:10.1126/science.1176112.

[15] Gambetta, A., et al. (2006), Real-time observation of nonlinear coherent phonon dynamics in single-walled carbon nanotubes, *Nat Phys*, *2*(8), 515–520, doi: 10.1038/nphys345.

[16] Gaufres, E., N. Izard, X. Le Roux, D. Marris-Morini, S. Kazaoui, E. Cassan, and L. Vivien (2010), Optical gain in carbon nanotubes, *Applied Physics Letters*, *96*(23), 231,105, doi:10.1063/1.3443634.

[17] Ghosh, S., S. M. Bachilo, and R. B. Weisman (2010), Advanced sorting of single-walled carbon nanotubes by nonlinear density-gradient ultracentrifugation, *Nature Nanotechnology*, *5*(6), 443–450, doi:10.1038/nnano.2010.68.

[18] Graham, M. W., Y.-Z. Ma, and G. R. Fleming (2008), Femtosecond photon echo spectroscopy of semiconducting single-walled carbon nanotubes, *Nano Lett.*, *8*(11), 3936–3941, doi:10.1021/nl802423w.

[19] Gülseren, O., T. Yildirim, and S. Ciraci (2002), Systematic ab initio study of curvature effects in carbon nanotubes, *Physical Review B*, *65*(15), 153,405, doi: 10.1103/PhysRevB.65.153405.

[20] Hamm, P. (2005), Principles of nonlinear optical spectroscopy : A practical approach, *University of Zurich*, *7*(4), 252–8, doi:10.1136/jnnp.2007.124404.

[21] Hogele, A., C. Galland, M. Winger, and A. Imamoğlu (2008), Photon antibunching in the photoluminescence spectra of a single carbon nanotube, *Physical Review Letters*, *100*(21), 217,401, doi:10.1103/PhysRevLett.100.217401.

[22] Iijima, S. (1991), Helical microtubules of graphitic carbon, *354*(6348), 56–58, doi:10.1038/354056a0.

[23] Jeschke, H. O., A. H. Romero, M. E. Garcia, and A. Rubio (2007), Microscopic investigation of laser-induced structural changes in single-wall carbon nanotubes, *Physical Review B*, *75*(12), 125,412, doi:10.1103/PhysRevB.75.125412.

[24] Jishi, R. A., D. Inomata, K. Nakao, M. S. Dresselhaus, and G. Dresselhaus (1994), Electronic and lattice properties of carbon nanotubes, *Journal of the Physical Society of Japan*, *63*(6), 2252–2260, doi:10.1143/JPSJ.63.2252.

[25] Kim, J.-H., et al. (2009), Chirality-selective excitation of coherent phonons in carbon nanotubes by femtosecond optical pulses, *Physical Review Letters*, *102*(3), 037,402, doi:10.1103/PhysRevLett.102.037402.

[26] Kitiyanan, B., W. Alvarez, J. Harwell, and D. Resasco (2000), Controlled production of single-wall carbon nanotubes by catalytic decomposition of CO on bimetallic Co–Mo catalysts, *Chemical Physics Letters*, *317*(3–5), 497–503, doi:10.1016/S0009-2614(99)01379-2.

[27] Kroto, H. W., J. R. Heath, S. C. O'Brien, R. F. Curl, and R. E. Smalley (1985), C60: Buckminsterfullerene, *318*(6042), 162–163, doi:10.1038/318162a0.

[28] Lefebvre, J., J. Fraser, Y. Homma, and P. Finnie (2004), Photoluminescence from single-walled carbon nanotubes: a comparison between suspended and micelle-encapsulated nanotubes, *Applied Physics A: Materials Science & Processing*, *78*(8), 1107–1110, doi:10.1007/s00339-003-2460-6.

[29] Liu, M., X. Yin, E. Ulin-Avila, B. Geng, T. Zentgraf, L. Ju, F. Wang, and X. Zhang (2011), A graphene-based broadband optical modulator, *Nature*, *474*, 64–67, doi:10.1038/nature10067.

[30] Ma, Y.-Z., J. Stenger, J. Zimmermann, S. M. Bachilo, R. E. Smalley, R. B. Weisman, and G. R. Fleming (2004), Ultrafast carrier dynamics in single-walled carbon nanotubes probed by femtosecond spectroscopy, *The Journal of Chemical Physics*, *120*, 3368, doi:10.1063/1.1640339.

[31] Ma, Y.-Z., L. Valkunas, S. L. Dexheimer, S. M. Bachilo, and G. R. Fleming (2005), Femtosecond spectroscopy of optical excitations in single-walled carbon nanotubes: Evidence for exciton-exciton annihilation, *Physical Review Letters*, *94*(15), 157,402, doi:10.1103/PhysRevLett.94.157402.

[32] Melchor, S., and J. A. Dobado (2004), CoNTub: an algorithm for connecting two arbitrary carbon nanotubes, *J. Chem. Inf. Comput. Sci.*, *44*(5), 1639–1646, doi:10.1021/ci049857w.

[33] Mueller, T., F. Xia, and P. Avouris (2010), Graphene photodetectors for high-speed optical communications, *Nat Photon*, *advance online publication*, doi:10.1038/nphoton.2010.40.

[34] Mukamel, S. (1999), *Principles of Nonlinear Optical Spectroscopy*, Oxford University Press, USA.

[35] Nair, R. R., P. Blake, A. N. Grigorenko, K. S. Novoselov, T. J. Booth, T. Stauber, N. M. R. Peres, and A. K. Geim (2008), Fine structure constant defines visual transparency of graphene, *Science*, *320*(5881), 1308, doi: 10.1126/science.1156965.

[36] Nelder, J. A., and R. Mead (1965), A simplex method for function minimization, *The Computer Journal*, *7*(4), 308–313, doi:10.1093/comjnl/7.4.308.

[37] Nicholson, J. W., R. S. Windeler, and D. J. DiGiovanni (2007), Optically driven deposition of single-walled carbon-nanotube saturable absorbers on optical fiber end-faces, *Optics Express*, *15*(15), 9176–9183, doi:10.1364/OE.15.009176.

[38] Novoselov, K. S., A. K. Geim, S. V. Morozov, D. Jiang, Y. Zhang, S. V. Dubonos, I. V. Grigorieva, and A. A. Firsov (2004), Electric field effect in atomically thin carbon films, *Science*, *306*(5696), 666–669, doi:10.1126/science.1102896.

[39] Novoselov, K. S., A. K. Geim, S. V. Morozov, D. Jiang, M. I. Katsnelson, I. V. Grigorieva, S. V. Dubonos, and A. A. Firsov (2005), Two-dimensional gas of massless dirac fermions in graphene, *Nature*, *438*(7065), 197–200, doi: 10.1038/nature04233.

[40] Nugraha, A. R. T., G. D. Sanders, K. Sato, C. J. Stanton, M. S. Dresselhaus, and R. Saito (2011), Chirality dependence of coherent phonon amplitudes in single-wall carbon nanotubes, *Physical Review B*, *84*(17), 174,302, doi: 10.1103/PhysRevB.84.174302.

[41] O'Connell, M. J., et al. (2002), Band gap fluorescence from individual single-walled carbon nanotubes, *Science*, *297*(5581), 593–596, doi: 10.1126/science.1072631.

[42] Perebeinos, V., J. Tersoff, and P. Avouris (2005), Effect of exciton-phonon coupling in the calculated optical absorption of carbon nanotubes, *Physical Review Letters*, *94*(2), 027,402, doi:10.1103/PhysRevLett.94.027402.

[43] Ranka, J. K., A. L. Gaeta, A. Baltuska, M. S. Pshenichnikov, and D. A. Wiersma (1997), Autocorrelation measurement of 6-fs pulses based on the two-photon-induced photocurrent in a GaAsP photodiode, *Optics Letters*, *22*(17), 1344–1346, doi:10.1364/OL.22.001344.

[44] Saito, R., G. Dresselhaus, and M. S. Dresselhaus (2000), Trigonal warping effect of carbon nanotubes, *Physical Review B*, *61*(4), 2981–2990, doi: 10.1103/PhysRevB.61.2981.

[45] Sanders, G. D., C. J. Stanton, J.-H. Kim, K.-J. Yee, Y.-S. Lim, E. H. Hároz, L. G. Booshehri, J. Kono, and R. Saito (2009), Resonant coherent phonon spectroscopy of single-walled carbon nanotubes, *Physical Review B*, *79*(20), 205,434, doi:10.1103/PhysRevB.79.205434.

[46] Schneck, J. R., A. G. Walsh, A. A. Green, M. C. Hersam, L. D. Ziegler, and A. K. Swan (2011), Electron correlation effects on the femtosecond dephasing dynamics of e22 excitons in (6,5) carbon nanotubes, *J. Phys. Chem. A*, *115*(16), 3917–3923, doi:10.1021/jp108345t.

[47] Tan, Y., and D. E. Resasco (2005), Dispersion of single-walled carbon nanotubes of narrow diameter distribution, *The Journal of Physical Chemistry B*, *109*(30), 14,454–14,460, doi:10.1021/jp052217r.

[48] Tans, S. J., A. R. M. Verschueren, and C. Dekker (1998), Room-temperature transistor based on a single carbon nanotube, *Nature*, *393*(6680), 49–52, doi:10.1038/29954.

[49] Uchiyama, K., A. Hibara, H. Kimura, T. Sawada, and T. Kitamori (2000), Thermal lens microscope, *Japanese Journal of Applied Physics*, *39*(Part 1, No. 9A), 5316–5322, doi:10.1143/JJAP.39.5316.

[50] Wallace, P. R. (1947), The band theory of graphite, *Physical Review*, *71*(9), 622, doi:10.1103/PhysRev.71.622.

[51] Wang, F., G. Dukovic, L. E. Brus, and T. F. Heinz (2004), Time-resolved fluorescence of carbon nanotubes and its implication for radiative lifetimes, *Physical Review Letters*, *92*(17), 177,401, doi:10.1103/PhysRevLett.92.177401.

[52] Wang, F., G. Dukovic, L. E. Brus, and T. F. Heinz (2005), The optical resonances in carbon nanotubes arise from excitons, *Science*, *308*(5723), 838–841, doi:10.1126/science.1110265.

[53] Wang, F., Y. Zhang, C. Tian, C. Girit, A. Zettl, M. Crommie, and Y. R. Shen (2008), Gate-variable optical transitions in graphene, *Science*, *320*(5873), 206–209, doi:10.1126/science.1152793.

[54] WangF., R. G., ScardaciV., SunZ., HennrichF., W. H., M. I., and F. C. (2008), Wideband-tuneable, nanotube mode-locked, fibre laser, *Nat Nano*, *3*(12), 738–742, doi:10.1038/nnano.2008.312.

[55] Weisman, R. B., and S. M. Bachilo (2003), Dependence of optical transition energies on structure for single-walled carbon nanotubes in aqueous suspension: An empirical kataura plot, *Nano Letters*, *3*(9), 1235–1238, doi:10.1021/nl034428i.

[56] Xia, F., M. Steiner, Y.-m. Lin, and P. Avouris (2008), A microcavity-controlled, current-driven, on-chip nanotube emitter at infrared wavelengths, *Nat Nano*, *3*(10), 609–613, doi:10.1038/nnano.2008.241.